Abstract

WANG, LEI. Elastic Wave Propagation in Composites and Least-squares Damage Localization Technique. (Under the direction of Dr. Fuh-Gwo Yuan)

The main objective of Structural Health Monitoring (SHM) is to be able to continuously monitor and assess the status of the integrity of a structure or its components with a high level of confidence and reliability. In general, the common techniques employed in SHM for monitoring structures and detecting damages can be divided into two categories: (1) vibration-based approach and (2) wave-based approach. Since wave-based approach can provide better local health status information and has higher sensitivity to damages than vibration-based approach, this thesis focuses on damage localization of plate structure using wave-based approach by first characterizing elastic waves in composite laminates; then using a time-frequency signal processing technique to analyze dispersive stress waves; and lastly a least-squares technique is proposed for damage localization.

Exact solutions of dispersive relations in a composite lamina and composite laminate are first deduced from three-dimensional (3-D) elasticity theory. The dispersion relations containing infinite number of symmetric and antisymmetric wave modes are numerically solved. Then, to make dispersive wave solutions tractable in composites, a higher-order plate theory is proposed. The dispersion relations of three antisymmetric wave modes and five symmetric wave modes can be analytically determined. The dispersion curves of phase velocity and group velocity are obtained from the two theories. From the results of the 3-D elasticity theory and higher-order plate theory, it can be seen from dispersion curves that the higher-order plate theory gives a good agreement in comparison with those obtained from 3-D elasticity theory in the relatively high frequency range; and especially for the lowest

symmetric and antisymmetric modes, dispersion relation curves obtained from the two theories match very well.

In the Chapter of time-frequency analysis of dispersive waves, a Wavelet Transform (WT) is directly performed on a transient dispersive wave to extract the time-frequency information of transient waves. Consequently, the dispersion relations of group velocity and phase velocity can be mathematically obtained. Experiments are set up to verify the proposed WT method, in which a lead break is used as a simulated acoustic emission source on the surface of an aluminum plate. The dispersion curves of both phase and group velocities of the lowest flexural wave mode obtained from the experiments by using WT show good agreement with theoretical prediction values.

Having group velocities verified from the experiments, a least-squares method is proposed to SHM field for iteratively searching damage location based on elastic wave energy measurements. The method is suitable for achieving automated SHM system since the proposed method is based on active damage detection technique and deals with the entire sensor data in the least-squares algorithm without the need of ambiguously measuring the time-of-flights. The simulated data are obtained from finite difference method in conjunction with Mindlin plate theory. Simulated examples for damage detection are demonstrated by using the least-squares method. Moreover, an active SHM system is set up to validate the feasibility of the least-squares damage localization technique. From the simulated and experimental results, it is shown that the estimated damage position by least-squares method gives good agreement with the targeted damage location.

ELASTIC WAVE PROPAGATION IN COMPOISTES AND LEAST-SQUARES DAMAGE LOCALIZATION TECHNIQUE

by

LEI WANG

A thesis submitted to the Graduate Faculty of
North Carolina State University
in partial fulfillment of the
requirements for the Degree of
Master of Science

AEROSPACE ENGINEERING

Raleigh

2004

APPROVED BY:

Dr. Kara Peters

Dr. Jeffrey W. Eischen

Dr. Fuh-Gwo Yuan
Chair of Advisory Committee

To my parents

and

Jane

Biography

Lei Wang was born in Dongying, Shandong Province, the People's Republic of China on July 1, 1977. Having received his elementary and secondary education in Dongying, he graduated from the No. 2 Middle School of Shengli Oil Field in 1995. He received his Bachelor of Science degree in Detecting Technology and Instruments from Nanjing University of Aeronautics and Astronautics in 1999. Since then he continued his graduate study in The Aeronautical Science Key Laboratory for Smart Materials and Structures at Nanjing University of Aeronautics and Astronautics for three years. He started his M.S. program of Aerospace Engineering at North Carolina State University in the fall of 2002.

Acknowledgements

First of all, I would like to thank Dr. Fuh-Gwo Yuan for suggesting the following work and serving as my graduate advisor over the past two years. I appreciate very much his warm guidance and enthusiastic encouragement throughout the work. Especially, his insight into cross disciplines, prowess of exploring frontier research and perseverance of pursuing perfection in research impress me greatly and will surely benefit my future academic career.

I would like to thank Drs. Kara Peters, Jeffrey W. Eischen, and Fen Wu for providing helpful advice in completing this research. I thank Dr. Shaorui Yang for his help and suggestion in this research. Special thanks go to Dr. Xiao Lin, one of Dr. Yuan's former Ph.D. students, who always offers me a warm and in-time assistance whenever I asked for.

This research is supported by the Sensors and Sensor Networks program from the National Science Foundation (Grant No. CMS-0329878). Dr. S. C. Liu is the program manager. The financial support is gratefully acknowledged.

Thanks also go to all the members in our research group including Mr. Yun Jin, Mr. Lei Liu, Ms. Aihua Liang, Mr. Artem Dyakonov, Mr. Saeed Nojovan, Mr. Perry Miller, Mr. H. Hussein, and Mr. Guoliang Jiang for their care and help. The friendship with them makes my life in Raleigh brighter and more colorful.

Additionally, my deepest appreciation goes to Mr. Ziyue Liu and his wife, Mr. Chunwei Wu, Mr. Jibing Li, Mr. Zheng Gao, and Mr. Andrew Bowman who were there whenever I needed. I would like to express my sincere thanks to all the people from whom I have received help and advised during my MS study at North Carolina State University.

Finally, I should thank my father, mother and brother. Without their understanding and encouragement, I could never reach this joyful moment.

Table of Contents

List of Tables

List of Figures

Nomenclature and Abbreviations

Greek Symbols

α	Reflection factor at the damage
ε_x, ε_y, ε_z	Normal strain components
ϕ	Direction of wave propagation or direction of wavenumber
ϕ_x, ϕ_y	Higher-order terms in the expression of displacement fields
φ	Skew angle of group velocity
Γ_{ij}	Elements of the determinant defined in Eq. (2.1-9)
γ	Sensor gain factor at a sensor
γ_{yz}, γ_{xz}, γ_{xy}	Engineering shear strain components
κ	Shear correction factor
ν	Poisson's ratio
θ	Phase angle
ϑ	Fiber orientation of a lamina
$\boldsymbol{\rho}$	Damage position vector
ρ	Mass density
Σ	Stress components along z direction on outer surfaces of a composite laminate
$\boldsymbol{\sigma}$	Contracted notation of stress components in the global coordinates
$\boldsymbol{\sigma}'$	Contracted notation of stress components in the principal material coordinates
σ_x, σ_y, σ_z	Normal stress components
ς	Updated step size in least-squares algorithm

τ	Time delay from the actuator to the damage
τ_{yz}, τ_{xz}, τ_{xy}	Shear stress components
υ	Zero-mean additive white Gaussian noise
ω	Angular frequency
ψ	Mother wavelet or base wavelet function
ψ_x, ψ_y	Rotations of section x = constant and y = constant, respectively

Roman Symbols

A, B, C	Displacement constants defined in Eq. (2.1-8)
a	Scale parameter in Wavelet Transform
a_0	Normalized reflected waveform from damage
b	Translation parameter in Wavelet Transform
C_{ij}	Components of stiffness matrix in the global coordinates
C'_{ij}	Components of stiffness matrix in the principal material coordinates
C_ψ	Admissible condition
c_g	Group velocity
c_L	Longitudinal wave velocity in the direction of fiber orientation $c_L = \sqrt{C_{11}/\rho}$
c_p	Phase velocity
D	Matrix variable defined in Eq. (2.1-32)
D	Plate bending stiffness, $D = \dfrac{Eh^3}{12(1-\nu^2)}$
E	Young's modulus
E	Mathematical expectation operator

f	Frequency
f_s	Sampling rate
$\mathbf{G}$	Local transfer matrix defined in Eq. (2.1-24)
G	Shear modulus
g	Square of sensor gain factor at a sensor
H_{ij}	Variables defined in Eq. (2.1-16)
h	Thickness of the plate
I	Moment of inertia
$\boldsymbol{J}$	Least-squares error function
$\mathbf{k}$	Wavenumber vector
k	Magnitude of wavenumber
L	Variables defined in Eq. (2.2-11)
l	Direction cosines of wave propagation
M	Moment resultant / unit length
N	Axial force / unit length
$\mathbf{P}$	Vector variable defined in Eq. (2.1-25)
p	Solutions of Eq. (2.1-11)
$\mathbf{Q}$	Transformation matrix
Q	Shear force / unit length
q	Five-peak excitation signal
R, S	Variables defined in Eq. (2.1-13), higher-order resultants
$\mathbf{r}$	Cartesian coordinates of a sensor
s	Modeled received signal without additive noise at a sensor

Re	Real part of a complex variable
T	Matrix variable defined in Eq. (2.1-26)
t	Time variable
u, v, w	Displacement components in the direction of x, y and z, respectively
U, V, W	Displacement components which are function of z and defined in Eq. (2.1-5)
U', V', W'	Derivatives of U, V, W with respect to z, respectively
V_f	Fiber volume fraction
x, y, z	Cartesian coordinates
x	Modeled received signal with additive noise at a sensor
y	Measured wave energy at a sensor
Z	Modeled wave energy at a sensor

Subscripts

0	Variables on the middle plane of the plate in Section 2.2
c	Denotes central frequency
m	Sensor number
n	Layer number of composite laminates
g	Denotes Gabor function
x, y, z	Components along the direction of Cartesian coordinates

Superscripts

i	Epoch of the least-squares algorithm
T	Transpose operator
+, -	Displacements or stress variables on the upper and lower surfaces of layer n

Caps

‿	Stress components divided by *ik*
^	Variables in frequency domain
~	Nondimensional variables
–	Complex conjugate
·	Derivative with respect to time

Abbreviations

3-D	Three-dimensional
CEV	Crew Exploration Vehicle
CPT	Classical Plate Theory
CWT	Continuous Wavelet Transform
DOA	Direction of Arrival
DWT	Discrete Wavelet Transform
NDE	Non-destructive Evaluation
PZT	Lead Zirconate Titanate
SDPT	Shear Deformation Plate Theory
SH	Shear Horizontal wave
SHM	Structural Health Monitoring
SNR	Signal to Noise Ratio
STFT	Short Time Fourier Transform
TDOA	Time Difference of Arrival
WT	Wavelet Transform
WVD	Wigner-Ville Distribution

1 Introduction

1.1 Structural Health Monitoring

The integrity of critical structures such as aircrafts, civil infrastructures, mechanical systems, etc., needs to be monitored in-situ and real-time to detect damage at an early stage. Traditional Non-destructive Evaluation (NDE) techniques can not be directly applied to monitor the health status of structures since these techniques usually rely on in-laboratory testing and require bulky instruments (Thomas, 1995). Especially for aerospace vehicles, the health monitoring system requires to perform on in-service structures with minimum manual interference. Therefore, integrated monitoring components such as sensors, either surface-mounted or embedded in the structures are compulsory in these circumstances (Boller, 1997). A structural health monitoring (SHM) system with built-in sensors has attracted much attention in the past decade (Chang, 1999; Doebling *et al*., 1996; Hall, 1999; Housner *et al*., 1997; and Sohn *et al*., 2004). Besides sensors, actuators exciting diagnostic signals can also be surface-mounted on or embedded in the structures to build an active SHM system. A major advantage of the active SHM system over a passive one (without built-in actuators) is that the active SHM is subjected to a prescribed actuation and thus increases the accuracy and reliability of assessing the structural status from the collected sensor data.

For real applications of SHM in aerospace, Boeing's new 7E7 aircraft will have a full-time built-in SHM system with sensors embedded in the structure to evaluate the state of structural health (Butterworth-Hayes, 2003). According to NASA's requirements on the new Crew Exploration Vehicle (CEV), Lockheed Martin's Atlas V and Boeing's Delta IV satellite launchers will soon have integrated health monitoring system to assess the overall

health of the vehicle continually during the ascent to spot a problem before it becomes catastrophic (Lannotta, 2004).

Detecting the location and identifying the dimension and form of damages are the primary goals of a SHM system. Generally, the common techniques of damage identification employed in SHM can be roughly divided into two categories: (1) vibration-based approach and (2) wave-based approach. Vibration-based technique can be considered as a global damage detection method, where the performance of the entire structure or system is monitored and verified. Wave-based technique can be regarded as a local damage detection method and only the certain key elements of the total system are interested in monitoring.

Numerous investigators have applied vibration-based methods to detect damage existence and attempt to localize damages mainly in civil structures such as bridges, highways, and buildings. However, there are several essential disadvantages limiting the extensive application of vibration-based damage detection methods. First, vibration-based approaches have low sensitivity to damage. The basic premise of most vibration-based damage detection methods is that damage will alter the stiffness, flexibility, mode shape, etc., which in turn alter the measured dynamic response of the structure such as resonant frequencies and mode shapes. However the damage is typically a local phenomenon, at least in the beginning stage, and may not significantly influence the global response of a structure that is normally measured from the vibration test. Second, a limited number of lower modes and truncated mode shapes that can be reliably determined can lead to systematic error. In vibration-based methods, the response measurement can be expressed in terms of a superposition of all mode shapes, but only a limited number of modes may be accessible in practice because of limited number of sensor measurements and loss of fidelity in higher

modes. Third, environmental and operational variations, such as varying temperature, moisture, loading conditions, and boundary conditions affecting the dynamic response of the structures can not be overlooked either (Farrar *et al*., 1994). These effects impair reliability of damage detection.

Wave-based damage detection however excites transient waves propagating in structures by actuators (or active sensors), since the waves will be reactive to damages such as reflection, scattering or dissipation, the health status of structures will be estimated by analyzing the response waves received by either surface-bonded or embedded sensors. Compared with vibration-based method, wave-based method can effectively obtain the local information of structures and can accommodate variations of boundary conditions and temperatures (Sohn *et al*., 2004). Many investigators have applied transient wave-based damage detection techniques to localizing damages and even quantifying the dimension of damage either in isotropic (e.g., Gaul and Hurlebaus, 1997; Hurlebaus, 2001; Lin and Yuan, 2001b; Quek *et al*., 2001; and Giurgiutiu *et al*, 2002), or in anisotropic materials (e.g., Cawley, 1994; Guo and Cawley, 1994; Tan *et al*., 1995; Birt, 1998; Jeong and Jang, 2000; Wang and Yuan, 2003; Sohn *et al*., 2004; and Ihn and Chang, 2004).

1.2 Elastic Waves in Composite Plates

The propagation of waves in an infinite elastic plate has been studied since 1889 dispersive waves based on the theory of elasticity in plane strain. For plane waves traveling in a free isotropic plate case, the waves are a combination of longitudinal and vertically polarized shear bulk waves propagating in a direction parallel to the plate. These two types of waves are coupled by the reflections in the plate. The resulting guided waves traveling along the plate axis in an isotropic material are called *Lamb waves*, which may have symmetric and

antisymmetric modes. The theory of Lamb waves has been fully documented in a number of textbooks (Viktorov, 1967 and Graff, 1991) and it has been widely applied in NDE (Krautkramer and Krautkramer, 1990; Blitz and Simpson, 1996; Hurbelaus *et al.*, 2001; and Wilcox *et al.*, 2001). In recent years, several investigators have also applied Lamb waves for SHM of isotropic materials. Lin and Yuan (2001a) analytically modeled Lamb wave signal generated and collected by piezoelectric (PZT) actuator/sensor. This model first combined the analytical solution of Mindlin plate theory and piezoelectric effect of the actuator/sensor, thus the voltage output of a sensor can be obtained directly from voltage input of the actuator. Giurgiutiu *et al*. (2002) investigated a Lamb waves based SHM of both aluminum beam and plate with integrated PZT sensors and actuators.

The increasing use of advanced composites in structural components, such as aerospace structures, marine vehicles, automotive parts, and many other applications has led to extensive research activities in the field of composite materials. The most widely used composite structures are laminates consisting of many fiber-reinforced laminae that are bonded together to achieve more desirable structural properties and better performance than conventional materials. To understand the dynamic response for use in damage detection, the theory of elastic waves in composite laminates is desirable to be developed. Due to anisotropic and multilayered properties of laminates, however, the exact analytical treatment of waves in composites is much more complicated and consumes more computational cost than that of waves in an isotropic plate.

Some of the difficulties in the treatment of wave propagation in anisotropic plates can be illustrated by considering slowness wave surface methods for infinite media (Synge, 1957; Fedorov, 1968; and Musgrave, 1970). Perhaps the most significant consequence of elastic

anisotropy is the loss of pure wave modes for general propagation directions. This fact also implies that the direction of group velocity (i.e., energy flow) does not generally coincide with the wave vector or wave front normal (Fedorov, 1968). In addition, the distinction between wave mode types in generally anisotropic plates is somewhat artificial, since the equations for classical Lamb and shear horizontal (SH) modes and symmetric and antisymmetric modes generally are coupled. Therefore, we will refer to these modes as elastic waves in plates (Nayfeh and Chimenti, 1989).

Tang *et al.* (1989) investigated the flexural wave motion in symmetric cross-ply and quasi-isotropic laminates by both elasticity theory and first-order plate theory, and then compared the analytical results with the experimental results. Nayfeh and Chimenti (1989) gave dispersion relation curves of elastic wave in general one-layered anisotropic media, i.e., composite lamina. Nayfeh (1991) developed a transfer matrix technique to obtain the dispersion relation curves of elastic waves propagating in multilayered anisotropic media, i.e., composite laminate. However, Nayfeh's formulation (1989, 1991) was limited to a given plane of incidence from a line load parallel to the *y*-axis such that the problem reduces to generalized plane deformation where all the three displacement components are functions of *x* and *z*. Yuan and Hsieh (1998) obtained the exact solutions of elastic waves in composite cylindrical shell based on both 3-D anisotropic elasticity theory and compared them with Flügge shell theory. However, these studies only obtained the dispersion relations of phase velocity, but not extended to group velocity. Besides the dispersion relations, several researchers also have studied the transient elastic waves in composite laminates (Liu *et al*., 1991 and Mal and Lih, 1992).

Approximate plate theories have been extremely useful in providing analytical solutions to a variety of problems involving static and dynamic response of laminated plates of finite dimensions under external loads. Furthermore, for computing the dispersion relations of elastic waves in composites, approximate plate theories can offer much higher computational efficiency than 3-D elasticity theory since approximate plate theories avoid solving time-consuming transcendental equations. This feature of approximate plate theories is very useful to achieve a real-time SHM system in practice. The laminated plate theories are direct extensions of those developed earlier for homogeneous isotropic and orthotropic plates, where use is made of displacement fields which do not account for interface continuity explicitly between the lamina. In the simplest approximation, namely, the Classical Plate theory (CPT) based on the Kirchhoff hypotheses have been developed by Reissner and Stavsky (1961), Dong, Pister and Taylor (1962), and summarized by Ashton and Whitney (1970). These works were based on a linear displacement across the entire laminate with shear deformation neglected. An improved Mindlin-type (Mindlin, 1960) first-order transverse shear deformation plate theory (SDPT) was developed by Whitney and Pagano (1970) for composite laminates. In this theory, linear displacements were assumed across the entire laminate thickness; however, transverse shear deformation was not neglected. Higher-order shear deformation theories have been proposed by other researchers (Lo *et al.*, 1977 and Reddy, 1984).

Since the symmetric wave motion is a promising mode for long range inspection and has proposed several methods by which damage can be detected in composite laminates, especially for delamination damage (Cawley, 1994; Guo and Cawley, 1992; and Birt, 1998), the approximate plate theory for symmetric waves in laminates are needed to be developed

for SHM. Kulkarni and Pagano (1972) presented the both 3-D elasticity theory and an approximate theory for vibration of elastic laminates. Due to a first-order SDPT, the dispersion of the first symmetric mode was not predicted by this theory. Whitney and Sun (1973) extended the above theory to a higher-order theory including the first symmetric thickness shear and thickness stretch modes by considering higher-order terms in the displacement expansion about the mid-plane of the laminate in a manner similar to that of Mindlin and Medick (1959) for homogeneous isotropic plates. These theories have been focused on the vibration problem of composites. The existing higher-order plate theory still needs to be extended to analyze elastic waves propagating along arbitrary direction in composites.

1.3 Time-frequency Analysis for Dispersive Waves

One of the main objectives of SHM is to extract certain physical parameters from measured data in structures and then to use them to quantify the health status of structures. Since the ultrasonic waves generated from initiation of the damage and/or reflected from the damage carry the information about the damage, the characterization of waves such as its dispersion curves needs to be further understood. In general, the phase and group velocities of dispersive waves propagating in plate-like solids are related to the geometry and material properties. Thus, evaluating the dispersion of phase and group velocities with sensible physical information is of practical importance in SHM.

In SHM, signal processing plays an essential role to physically interpret the collected data records from sensors, extract health status information of structures, and even improve the decision on damage detection. Generally the collected signals are non-stationary time series in nature. Traditional Fourier analysis is obviously unsuitable for processing these time

series since it is mainly a stationary time series based processing technique and is unable to simultaneously provide both time and frequency information. In the past, the Fourier transform has been extensively used for the analysis of dispersive wave signals (Sachse and Pao, 1978; Wu and Chen, 1996). In recent years, some advanced techniques based on the time-frequency analysis were applied to study waves in solids, such as Short-Time Fourier Transform (STFT) (Hodges, Power and Woodhouse, 1985) and Wigner-Ville Distribution (WVD) (Latif *et al*., 1999). However, because of the constant window structure employed in STFT, it is not capable of providing sufficient resolution over a wide spectral range. Furthermore, since WVD is defined as the Fourier transform of the central covariance function of a given signal and has quadratic structure, it inevitably generates interference terms that incur spurious information to the results of WVD.

Compared with these techniques, Wavelet Transform (WT) appears to be a very attractive signal processing technique for non-stationary signals and has been proved to be a more versatile and effective tool for studying dispersive waves. One of the earliest introductory works on dispersive waves using WT is by Önsay and Haddow (1995). They selected a complex Morlet wavelet as a mother wavelet function but did not examine the dispersion relations of phase and group velocities. Kishimoto et al. (1995) applied a Gabor wavelet to time-frequency analysis of flexural waves and obtained the dispersion relations of group velocity from numerically simulation data of an Euler beam. In addition, Quek et al. (2001) investigated several key practical issues on the application of Gabor wavelet to dispersive waves such as sampling rate, choice and resolution of wavelet scales. Furthermore, by knowing the dispersion relation, a couple of practical NDE applications were developed from WT. For example, Gaul and Hurlebaus (1997) applied the Gabor WT to

an impact load location on aluminum plate and Sohn et al. (2004) located the multiple delamination damages in a quasi-isotropic laminate by using WT; Jeong and Jang (2000) and Jeong (2001) obtained the group velocity of the lowest mode of flexural waves and detect a source location of an acoustic emission event in a composite laminates by using Gabor WT. Besides the Gabor WT in dispersion research, another common used WT is harmonic WT, which is one of orthogonal wavelets and has compact supports in the frequency domain, developed by Newland (1993, 1997, 1998, and 1999). However, in the previous research either by Kishimoto et al. (1995), Jeong and Jang (2000), or Jeong (2001), the time-frequency analysis of dispersive waves to obtain the group velocity was not mathematically rigorous, where WT were performed on a much simpler case that two harmonic waves with close frequency propagate together. In addition, those studies can merely obtain the dispersive group velocity determined from time-frequency map of WT, not the phase velocity.

1.4 Least-squares Damage Localization

Mathematically, locating damage is an inverse problem. The estimated damage location may be calculated from collected signals such that the error function can reach its minimum. The proposed least-squares damage localization technique utilizes the real-valued signals reflected from a single damage and iteratively searches damage position until a error function reaches its minimum value.

For conventional damage detection techniques, the wave velocity and time-of-flight or arrival time of damage reflected waves need to be measured, and then with specific algorithms the damage position can be detected (Kehlenbach and Hanselka, 2003; Jeong, 2001; Wang *et al*; and Ihn and Chang, 2004). Since the excitation is narrow-band and has a

finite envelope in time domain, the ambiguity of evaluating of time-of-flight, which is based on detecting the peak of envelope of damage reflected waves, is not negligible.

Existing acoustic source localization methods make use of three common types of physical measurements: time difference of arrival (TDOA), direction of arrival (DOA), and source signal strength or energy. DOA can be estimated by exploiting the phase difference measured at received sensors (Haykin, 1985; Taff, 1997; and Kaplan *et al.*, 2001) and is applicable when the acoustic source emits a coherent narrow band signal. TDOA is suitable for broadband acoustic source localization and has been extensively investigated (Yao *et al*., 1998 and Reed *et al*., 1999). It requires accurate measurements of the relative time delay between sensors. It is known that the intensity or equivalently the energy of acoustic signal attenuates as a function of distance from the source. Using this property, recently, an energy-based acoustic source localization method has been reported (Sheng and Hu, 2003). Since the TDOA needs a sensor array and a large number of sensors and DOA has to detect the arrival time, these two methods are not suitable for extending then in SHM. Thus, the third approach based on wave energy measurement is more suitable and feasible in a practical SHM system.

1.5 Summary

The main content of this study is covered in Chapter 2 through Chapter 5. In Chapter 2, the exact solutions of elastic waves in one-layered anisotropic plate based on 3-D elasticity theory are established, and then are extended to a multi-layered anisotropic plate (composite laminate) with an arbitrary stacking sequence. The dispersion relations of both infinite symmetric and antisymmetric wave modes can be numerically obtained. A higher-order plate theory for waves in laminates is also developed based on a method developed by Whitney and Sun (1973). Three modes of antisymmetric wave modes and five modes of symmetric

wave modes are derived from the proposed approximate plate theory. Besides the dispersion curves of phase velocity, the dispersion curves of group velocity for elastic waves in IM7/5250-4 graphite/epoxy composite laminate are computed. For each numerical example, the dispersion relations calculated from 3-D elasticity theory are compared with the results obtained from the higher-order plate theory.

In Chapter 3, WT is used to analyze the dispersion relations of elastic waves in a plate. WT is directly performed on a dispersive wave to extract the time-frequency information. Consequently, the dispersion relations of not only group velocity but also phase velocity can be mathematically obtained. Experiments are performed by using a lead break as the simulated acoustic emission source on the surface of an aluminum plate. The dispersion curves of both phase and group velocities obtained from the experiments by using WT show good agreement with theoretical prediction values.

In Chapter 4, a least-squares method is first introduced to iteratively search damage location in plates by using energy measurement of elastic waves. An elastic wave energy decay model for wave propagating in plates is first derived. Then the least-squares method is applied to iteratively searching damage localization based on elastic wave energy measurements. The proposed method possesses several advantages over other triangulation methods. First the method can be used in the active damage detection which is suitable for the applications of SHM. Second the signals collected by sensors are used in the model without measuring the time-of-flight or arrival time which oftentimes is ambiguous to be measured. Lastly, environmental noise can be readily taken into account in the model. An active SHM system is set up to validate the feasibility of the least-squares damage localization method. From the simulated and experimental results on an aluminum plate, it is

shown that the estimated damage position by least-squares method provides good agreement with the targeted damage location.

Chapter 5 summarizes the contributions and conclusions of this study and also proposes some perspective topics for the future research.

2 Elastic Wave Dispersion in Composite Laminates

In describing elastic wave propagation in symmetric laminates, there exist two types of uncoupled wave motion: symmetric (extensional and/or shear horizontal) waves and antisymmetric (flexural and/or shear horizontal) waves. Under general excitation in a plate, these types of waves may usually co-exist.

In this Chapter, dispersion curves in laminated composite plates are modeled by both 3-D elasticity theory and a higher-order plate theory. The advantage of using 3-D elasticity theory is obvious in that the "exact" solutions hold for all frequency ranges. However, the exact solutions consist of infinite wave modes, symmetric or antisymmetric motions. The mode conversions that occur when the wave mode interacts with inhomogeneity add additional complexities. Although 3-D elasticity solutions can provide an exact modeling capability, computational cost is too high to achieve real-time processing for SHM, not to mention the transcendental equations inevitably need to be numerically solved for dispersion curves. Thus, a higher-order plate theory is examined to obtain approximate solutions of waves in composites. Three modes of antisymmetric wave and five modes of symmetric wave can be obtained from the higher-order plate theory.

Dispersion relations of symmetric and antisymmetric waves in both composite lamina and laminates are analyzed. The relations are illustrated in IM7/5250-4 graphite/epoxy lamina and laminates. The validity of the approximate dispersion relations based on the higher-order plate theory is made in comparison with those from 3-D elasticity theory. From these numerical results, it may be observed that the higher-order plate theory give a very good agreement in the relatively high frequency range.

2.1 Exact Solutions for Wave in a Composite Plate

In this section, a rectangular Cartesian coordinate system *x*, *y* and *z* axis is used with *z* axis normal to the mid-plane of plate spanned by *x* and *y* axis. A wave propagates in a composite plate in an arbitrary direction that can be described by an angle ϕ with respect to *x* axis. First, 3-D elasticity theory is used to model the waves in a composite lamina to obtain closed-form dispersion relations. Then, imposing continuity of displacements and tractions along the interfaces with traction-free surface conditions, the dispersion of waves in composite laminates may be computed.

Nayfeh and Chimenti (1989) gave dispersion curves of elastic wave in general one-layered anisotropic media, i.e., composite lamina. Nayfeh (1991) developed a transfer matrix technique to obtain the dispersion relation curves of elastic wave propagating in multilayered anisotropic media, i.e., composite laminate. However, Nayfeh's formulation (1989, 1991) was limited to a given plane of incidence from a line load parallel to the *y*-axis such that the problem reduces to generalized plane deformation where all the three displacement components are functions of *x* and *z*.

2.1.1 Waves in a composite lamina

Consider a composite lamina with surfaces at $z = \pm h/2$, the stress-strain relations for a monoclinic material with respect to *z* axis are given by:

$$\begin{Bmatrix} \sigma_x \\ \sigma_y \\ \sigma_z \\ \tau_{yz} \\ \tau_{xz} \\ \tau_{xy} \end{Bmatrix} = \begin{bmatrix} C_{11} & C_{12} & C_{13} & 0 & 0 & C_{16} \\ C_{12} & C_{22} & C_{23} & 0 & 0 & C_{26} \\ C_{13} & C_{23} & C_{33} & 0 & 0 & C_{36} \\ 0 & 0 & 0 & C_{44} & C_{45} & 0 \\ 0 & 0 & 0 & C_{45} & C_{55} & 0 \\ C_{16} & C_{26} & C_{36} & 0 & 0 & C_{66} \end{bmatrix} \begin{Bmatrix} \varepsilon_x \\ \varepsilon_y \\ \varepsilon_z \\ \gamma_{yz} \\ \gamma_{xz} \\ \gamma_{xy} \end{Bmatrix} \tag{2.1-1}$$

Generally, when the global coordinate system (x, y, z) does not coincide with the principal material coordinate system (x', y', z) but makes an angle ϑ with the z-axis, the stiffness matrix C_{ij} in (x, y, z) system can be obtained from the stiffness matrix C'_{ij} in (x', y', z) system by using a transformation matrix **Q** as shown in Appendix A.1. Additionally, the material stiffness matrix C'_{ij} calculated from composite material properties E_i, ν_{ij}, and G_{ij} are given in Appendix A.2.

The linear strain-displacement relations are

$$\varepsilon_x = \frac{\partial u}{\partial x}, \quad \varepsilon_y = \frac{\partial v}{\partial y}, \quad \varepsilon_z = \frac{\partial w}{\partial z}, \quad \gamma_{xy} = \frac{\partial u}{\partial y} + \frac{\partial v}{\partial x}, \quad \gamma_{xz} = \frac{\partial u}{\partial z} + \frac{\partial w}{\partial x}, \quad \gamma_{yz} = \frac{\partial v}{\partial z} + \frac{\partial w}{\partial y} \tag{2.1-2}$$

where u, v, and w are the displacement components in the x, y, and z directions, respectively.

The equations of motion are given by:

$$\frac{\partial \sigma_x}{\partial x} + \frac{\partial \tau_{xy}}{\partial y} + \frac{\partial \tau_{xz}}{\partial z} = \rho \frac{\partial^2 u}{\partial t^2} \tag{2.1-3a}$$

$$\frac{\partial \tau_{xy}}{\partial x} + \frac{\partial \sigma_y}{\partial y} + \frac{\partial \tau_{yz}}{\partial z} = \rho \frac{\partial^2 v}{\partial t^2} \tag{2.1-3b}$$

$$\frac{\partial \tau_{xz}}{\partial x} + \frac{\partial \tau_{yz}}{\partial y} + \frac{\partial \sigma_z}{\partial z} = \rho \frac{\partial^2 w}{\partial t^2} \tag{2.1-3c}$$

and traction-free boundary conditions on the top and bottom surfaces are

$$\sigma_z = \tau_{xz} = \tau_{yz} = 0, \qquad \text{at } z = \pm h/2 \tag{2.1-4}$$

For transient waves propagating in the *x*-*y* plane of the plate in a direction of angle ϕ with respect to the *x* axis, the displacements have the form

$$u = U(z)e^{i[(k_x x + k_y y) - \omega t]},\ v = V(z)e^{i[(k_x x + k_y y) - \omega t]},\ w = W(z)e^{i[(k_x x + k_y y) - \omega t]} \tag{2.1-5}$$

where $\mathbf{k} = [k_x,\ k_y]^T$ is the wave vector and its magnitude $|\mathbf{k}| = k = \sqrt{k_x^2 + k_y^2} = \omega / c_p$ is the wave number, ω is the angular frequency, and c_p is the phase velocity. Note that **k** points in the direction of propagation. In the *x*-*y* plane, $\mathbf{k} = k[\cos\phi,\ \sin\phi]^T$ where ϕ is the direction of wave propagation, defined counterclockwise relative to the *x*-axis.

Substituting Eq. (2.1-5) into Eq. (2.1-1) and (2.1-2), we obtain

$$\sigma_x = [C_{11}k_x U + C_{12}k_y V - iC_{13}W' + C_{16}(k_y U + k_x V)]ie^{i[(k_x x + k_y y) - \omega t]} \tag{2.1-6a}$$

$$\sigma_y = [C_{12}k_x U + C_{22}k_y V - iC_{23}W' + C_{26}(k_y U + k_x V)]ie^{i[(k_x x + k_y y) - \omega t]} \tag{2.1-6b}$$

$$\sigma_z = [C_{13}k_x U + C_{23}k_y V - iC_{33}W' + C_{36}(k_y U + k_x V)]ie^{i[(k_x x + k_y y) - \omega t]} \tag{2.1-6c}$$

$$\tau_{yz} = [C_{44}(V' + ik_y W) + C_{45}(U' + ik_x W)]e^{i[(k_x x + k_y y) - \omega t]} \tag{2.1-6f}$$

$$\tau_{xz} = [C_{45}(V' + ik_y W) + C_{55}(U' + ik_x W)]e^{i[(k_x x + k_y y) - \omega t]} \tag{2.1-6e}$$

$$\tau_{xy} = [C_{16}k_x U + C_{26}k_y V - iC_{36}W' + C_{66}(k_y U + k_x V)]ie^{i[(k_x x + k_y y) - \omega t]} \tag{2.1-6f}$$

where the prime indicates the derivative with respect to *z*. Substituting Eq. (2.1-6) into Eq. (2.1-3), the equations of motion become

$$-C_{55}U'' - C_{45}V'' + (C_{11}l_x^2 + 2C_{16}l_xl_y + C_{66}l_y^2 - \rho c_p^2)U + (C_{16}l_x^2 + C_{12}l_xl_y + C_{66}l_xl_y + C_{26}l_y^2)V - i(C_{13}l_x + C_{55}l_x + C_{36}l_y + C_{45}l_y)W' = 0 \quad (2.1\text{-}7a)$$

$$-C_{45}U'' - C_{44}V'' + (C_{16}l_x^2 + C_{12}l_xl_y + C_{66}l_xl_y + C_{26}l_y^2)U + (C_{66}l_x^2 + 2C_{26}l_xl_y + C_{22}l_y^2 - \rho c_p^2)V - i(C_{36}l_x + C_{45}l_x + C_{23}l_y + C_{44}l_y)W' = 0 \quad (2.1\text{-}7b)$$

$$i[(C_{13} + C_{55})l_x + (C_{36} + C_{45})l_y)]U' + i[(C_{36} + C_{45})l_x + (C_{23} + C_{44})l_y]V' + iC_{33}W'' - (C_{44}l_y^2 + 2C_{45}l_xl_y + C_{55}l_x^2 - \rho c_p^2)W = 0 \quad (2.1\text{-}7c)$$

where $l_x = \cos\phi$, $l_y = \sin\phi$, and $c_p = \omega/k$ is the phase velocity. It is assumed that solutions of Eq. (2.1-7) have the following forms

$$U = Ae^{ikpz}, \quad V = Be^{ikpz}, \quad W = Ce^{ikpz} \quad (2.1\text{-}8)$$

Substituting these expressions into the equations of motion, Eq. (2.1-7) may be rearranged in a matrix form

$$\begin{bmatrix} \Gamma_{11} - \rho c_p^2 & \Gamma_{12} & \Gamma_{13} \\ & \Gamma_{22} - \rho c_p^2 & \Gamma_{23} \\ \text{sym} & & \Gamma_{33} - \rho c_p^2 \end{bmatrix} \begin{Bmatrix} A \\ B \\ C \end{Bmatrix} = 0 \quad (2.1\text{-}9)$$

The elements in the symmetric matrix above are listed as follows:

$$\Gamma_{11} = C_{11}l_x^2 + 2C_{16}l_xl_y + C_{66}l_y^2 + C_{55}p^2 \quad (2.1\text{-}10a)$$

$$\Gamma_{12} = C_{16}l_x^2 + (C_{12} + C_{66})l_xl_y + C_{26}l_y^2 + C_{45}p^2 \quad (2.1\text{-}10b)$$

$$\Gamma_{13} = [(C_{13} + C_{55})l_x + (C_{36} + C_{45})l_y)]p \quad (2.1\text{-}10c)$$

$$\Gamma_{22} = C_{66}l_x^2 + 2C_{26}l_xl_y + C_{22}l_y^2 + C_{44}p^2 \quad (2.1\text{-}10e)$$

$$\Gamma_{23} = [(C_{36} + C_{45})l_x + (C_{23} + C_{44})l_y)]p \quad (2.1\text{-}10f)$$

$$\Gamma_{33} = C_{55}l_x^2 + 2C_{45}l_xl_y + C_{44}l_y^2 + C_{33}p^2 \quad (2.1\text{-}10g)$$

The matrix Eq. (2.1-9) has a nontrivial solution for A, B, and C only if the determinant of the 3×3 matrix equals zero. The determinant can be set to zero, giving the following sixth-order polynomial in terms of p:

$$p^6 + \alpha\, p^4 + \beta\, p^2 + \gamma = 0 \tag{2.1-11}$$

Since Eq. (2.1-11) is a equation of p^2, it has three roots for p^2 (p_j, $j = 1, 2, 3$). Hence the six roots for p can be arranged in three pairs as

$$p_{j+1} = -p_j, \quad (j = 1, 3, 5) \tag{2.1-12}$$

For each p_j, B and C can be expressed in terms of A *via* Eq. (2.1-9) as

$$\begin{aligned} B &= \frac{(\Gamma_{11} - \rho c_p^2)\Gamma_{23} - \Gamma_{12}\Gamma_{13}}{\Gamma_{13}(\Gamma_{22} - \rho c_p^2) - \Gamma_{12}\Gamma_{23}} A \equiv RA \\ C &= \frac{(\Gamma_{11} - \rho c_p^2)\Gamma_{23} - \Gamma_{12}\Gamma_{13}}{\Gamma_{12}(\Gamma_{33} - \rho c_p^2) - \Gamma_{23}\Gamma_{13}} A \equiv SA \end{aligned} \tag{2.1-13}$$

Consequently, the general solution of Eq. (2.1-7) is

$$U = \sum_{j=1}^{6} A_j e^{ikp_j z}, \quad V = \sum_{j=1}^{6} R_j A_j e^{ikp_j z}, \quad W = \sum_{j=1}^{6} S_j A_j e^{ikp_j z} \tag{2.1-14}$$

Substituting Eq. (2.1-14) into the expression of σ_z, τ_{yz}, and τ_{xz}, with traction-free boundary conditions on the top and bottom surfaces $z = \pm h/2$, then σ_z, τ_{yz} and τ_{xz} may be expressed as

$$(\sigma_z,\ \tau_{yz},\ \tau_{xz})\Big|_{z=\pm h/2} = ike^{i[(k_x x + k_y y) - \omega t]} \sum_{j=1}^{6} (H_{1j},\ H_{2j},\ H_{3j}) A_j e^{\pm ikp_j h/2} = 0 \tag{2.1-15}$$

where

$$H_{1j} = C_{13} l_x + C_{23} l_y R_j + C_{33} p_j S_j + C_{36}(l_y + l_x R_j) \tag{2.1-16a}$$

$$H_{2j} = C_{44}(p_j R_j + l_y S_j) + C_{45}(p_j + l_x S_j) \tag{2.1-16b}$$

$$H_{3j} = C_{45}(p_j R_j + l_y S_j) + C_{55}(p_j + l_x S_j) \tag{2.1-16c}$$

Eq. (2.1-15) can be recast into a matrix form as

$$\begin{bmatrix} H_{11}e^{ikp_1h/2} & H_{12}e^{ikp_2h/2} & H_{13}e^{ikp_3h/2} & H_{14}e^{ikp_4h/2} & H_{15}e^{ikp_5h/2} & H_{16}e^{ikp_6h/2} \\ H_{21}e^{ikp_1h/2} & H_{22}e^{ikp_2h/2} & H_{23}e^{ikp_3h/2} & H_{24}e^{ikp_4h/2} & H_{25}e^{ikp_5h/2} & H_{26}e^{ikp_6h/2} \\ H_{31}e^{ikp_1h/2} & H_{32}e^{ikp_2h/2} & H_{33}e^{ikp_3h/2} & H_{34}e^{ikp_4h/2} & H_{35}e^{ikp_5h/2} & H_{36}e^{ikp_6h/2} \\ H_{11}e^{-ikp_1h/2} & H_{12}e^{-ikp_2h/2} & H_{13}e^{-ikp_3h/2} & H_{14}e^{-ikp_4h/2} & H_{15}e^{-ikp_5h/2} & H_{16}e^{-ikp_6h/2} \\ H_{21}e^{-ikp_1h/2} & H_{22}e^{-ikp_2h/2} & H_{23}e^{-ikp_3h/2} & H_{24}e^{-ikp_4h/2} & H_{25}e^{-ikp_5h/2} & H_{26}e^{-ikp_6h/2} \\ H_{31}e^{-ikp_1h/2} & H_{32}e^{-ikp_2h/2} & H_{33}e^{-ikp_3h/2} & H_{34}e^{-ikp_4h/2} & H_{35}e^{-ikp_5h/2} & H_{36}e^{-ikp_6h/2} \end{bmatrix} \begin{Bmatrix} A_1 \\ A_2 \\ A_3 \\ A_4 \\ A_5 \\ A_6 \end{Bmatrix} = 0 \tag{2.1-17}$$

From Eq. (2.1-10), Γ_{13} and Γ_{23} are odd functions of p and the other Γ's are even functions of p. Then, it can be readily shown from Eq. (2.1-13) that

$$R_{j+1} = R_j, \quad S_{j+1} = -S_j \qquad (j = 1, 3, 5) \tag{2.1-18}$$

and hence from Eq. (2.1-16),

$$H_{1\,j+1} = H_{1j}, \quad H_{2\,j+1} = -H_{2j}, \quad H_{3\,j+1} = -H_{3j}, \qquad (j = 1, 3, 5) \tag{2.1-19}$$

Substituting Eq. (2.1-12), (2.1-18), and (2.1-19) into Eq. (2.1-17), Eq. (2.1-17) can be simplified as

$$\begin{bmatrix} H_{11}e^{ikp_1h/2} & H_{11}e^{-ikp_1h/2} & H_{13}e^{ikp_3h/2} & H_{13}e^{-ikp_3h/2} & H_{15}e^{ikp_5h/2} & H_{15}e^{-ikp_5h/2} \\ H_{21}e^{ikp_1h/2} & -H_{21}e^{-ikp_1h/2} & H_{23}e^{ikp_3h/2} & -H_{23}e^{-ikp_3h/2} & H_{25}e^{ikp_5h/2} & -H_{25}e^{-ikp_5h/2} \\ H_{31}e^{ikp_1h/2} & -H_{31}e^{-ikp_1h/2} & H_{33}e^{ikp_3h/2} & -H_{33}e^{-ikp_3h/2} & H_{35}e^{ikp_5h/2} & -H_{35}e^{-ikp_5h/2} \\ H_{11}e^{-ikp_1h/2} & H_{11}e^{ikp_1h/2} & H_{13}e^{-ikp_3h/2} & H_{13}e^{ikp_3h/2} & H_{15}e^{-ikp_5h/2} & H_{15}e^{ikp_5h/2} \\ H_{21}e^{-ikp_1h/2} & -H_{21}e^{ikp_1h/2} & H_{23}e^{-ikp_3h/2} & -H_{23}e^{ikp_3h/2} & H_{25}e^{-ikp_5h/2} & -H_{25}e^{ikp_5h/2} \\ H_{31}e^{-ikp_1h/2} & -H_{31}e^{ikp_1h/2} & H_{33}e^{-ikp_3h/2} & -H_{33}e^{ikp_3h/2} & H_{35}e^{-ikp_5h/2} & -H_{35}e^{ikp_5h/2} \end{bmatrix} \begin{Bmatrix} A_1 \\ A_2 \\ A_3 \\ A_4 \\ A_5 \\ A_6 \end{Bmatrix} = 0 \tag{2.1-20}$$

In order to have a nontrivial solution, the determinant of the 3×3 matrix Eq. (2.1-20) should be zero. In the following, a number of procedures among columns are taken with the aim of reducing the 6×6 matrix into manageable two 3×3 submatrices. In the first step, the negative of the second column is added to the first, the negative of the fourth to the third, and

the negative of the sixth to the fifth. In the second step, the original first column is added to the second, the third to the fourth, and the fifth to the sixth. In the third step, column two is exchanged with column three, then column three with column five, and then column four with five. After these steps, one can easily see that by either adding or subtracting various columns the determinant can be reduced and partitioned into two uncoupled submatrices whose entries comprise 3×3 square matrices.

$$\begin{vmatrix} H_{11}\sin kp_1 h/2 & H_{13}\sin kp_3 h/2 & H_{15}\sin kp_5 h/2 & 0 & 0 & 0 \\ H_{21}\cos kp_1 h/2 & H_{23}\cos kp_3 h/2 & H_{25}\cos kp_5 h/2 & 0 & 0 & 0 \\ H_{31}\cos kp_1 h/2 & H_{33}\cos kp_3 h/2 & H_{35}\cos kp_5 h/2 & 0 & 0 & 0 \\ 0 & 0 & 0 & H_{11}\cos kp_1 h/2 & H_{13}\cos kp_3 h/2 & H_{15}\cos kp_5 h/2 \\ 0 & 0 & 0 & H_{21}\sin kp_1 h/2 & H_{23}\sin kp_3 h/2 & H_{25}\sin kp_5 h/2 \\ 0 & 0 & 0 & H_{31}\sin kp_1 h/2 & H_{33}\sin kp_3 h/2 & H_{35}\sin kp_5 h/2 \end{vmatrix} = 0 \quad (2.1\text{-}21)$$

The determinant can therefore be separated, leading to the two independent dispersion relations

$$H_{11}(H_{23}H_{35}-H_{25}H_{33})\tan kp_1 h/2 + H_{13}(H_{25}H_{31}-H_{21}H_{35})\tan kp_3 h/2 + H_{15}(H_{21}H_{33}-H_{23}H_{31})\tan kp_5 h/2 = 0 \quad (2.1\text{-}22)$$

$$H_{11}(H_{23}H_{35}-H_{25}H_{33})\cot kp_1 h/2 + H_{13}(H_{25}H_{31}-H_{21}H_{35})\cot kp_3 h/2 + H_{15}(H_{21}H_{33}-H_{23}H_{31})\cot kp_5 h/2 = 0 \quad (2.1\text{-}23)$$

corresponding to antisymmetric and symmetric wave modes respectively.

Since the components of H matrix and p_j are implicitly function of c_p, Eq. (2.1-22) or (2.1-23) is a transcendental equation relating the frequency and phase velocity. A numerical iterative method is listed as follows to obtain dispersion relations of phase velocity for a specified wave number direction (i.e., ϕ is given) (Rose, 1999).

1) Choose a frequency-thickness product fh;

2) Make an initial estimate of the phase velocity $(c_p)_0$;

3) Evaluate the sign of each of the left-hand sides of Eq. (2.1-22) or (2.1-23);

4) Choose another phase velocity $(c_p)_1 > (c_p)_0$ and re-evaluate the sign of Eq. (2.1-22) or (2.1-23);

5) Repeat steps (2) and (4) until the sign changes. Since the functions involved are continuous, a change in sign must be accompanied by a crossing through zero. Therefore, a root *m* exists in the interval where sign change occurs. Assume that this happens between phase velocities $(c_p)_n$ and $(c_p)_{n+1}$;

6) Use an iterative root-finding algorithm (e.g., Newton-Homer, bisection, Muller, *etc*.) to locate precisely the phase velocity in the interval $(c_p)_n < (c_p)_m < (c_p)_{n+1}$ where the left-hand side of the required equation is close enough to zero;

7) After finding the root, continue searching at this *fh* for other roots according to step (2) through step (6);

8) Choose another *fh* product and repeat step (2) through (7).

2.1.2 Waves in a composite laminate

In composite laminates, the dispersion curves are strongly influenced by the inherent anisotropy and heterogeneity of the composites. There are two different methods namely Transfer Matrix Method and Assemble Matrix Method to obtain the dispersion relations of waves in composite laminates. Although the procedure of these two methods looks different, they are identical in principle by both satisfying traction-free boundary conditions on the top and bottom surfaces of the composite laminate and continuity of interface conditions between two adjacent layers in different manner. Although these two methods can obtain a general

laminate with an arbitrary stacking sequence, it is unlikely to distinguish the symmetric and antisymmetric modes even in a symmetric laminate. To overcome this deficiency, a method is developed to decouple symmetric and antisymmetric modes in a symmetric laminate by imposing symmetric and antisymmetric boundary conditions at the mid-plane of the plate.

TRANSFER MATRIX METHOD

Using the relations in Eq. (2.1-5), (2.1-14), and (2.1-15), the solutions for the displacements and stresses may be expressed in a matrix form:

$$\begin{Bmatrix} u \\ v \\ w \\ \breve{\sigma}_z \\ \breve{\tau}_{yz} \\ \breve{\tau}_{xz} \end{Bmatrix} = \begin{bmatrix} 1 & 1 & 1 & 1 & 1 & 1 \\ R_1 & R_2 & R_3 & R_4 & R_5 & R_6 \\ S_1 & S_2 & S_3 & S_4 & S_5 & S_6 \\ H_{11} & H_{12} & H_{13} & H_{14} & H_{15} & H_{16} \\ H_{21} & H_{22} & H_{23} & H_{24} & H_{25} & H_{26} \\ H_{31} & H_{32} & H_{33} & H_{34} & H_{35} & H_{36} \end{bmatrix} \begin{Bmatrix} e^{ikp_1 z} A_1 \\ e^{ikp_2 z} A_2 \\ e^{ikp_3 z} A_3 \\ e^{ikp_4 z} A_4 \\ e^{ikp_5 z} A_5 \\ e^{ikp_6 z} A_6 \end{Bmatrix} e^{i[(k_x x + k_y y) - \omega t]} \qquad (2.1\text{-}24)$$

Here for convenience of subsequent analysis, the following variables have been used: $\breve{\sigma}_z = \sigma_z / ik$, $\breve{\tau}_{yz} = \tau_{yz} / ik$, and $\breve{\tau}_{xz} = \tau_{xz} / ik$.

Suppose a laminate consists of *N* layers as shown in Figure 2.1. The above equation holds for every layer *n*. For brevity, the term $e^{i[(k_x x + k_y y) - \omega t]}$ is suppressed in the later discussion. Eq (2.1-24) in each layer *n* is rewritten in a compact form:

$$\mathbf{P}^{\pm}_{(n)} = \mathbf{G}_{(n)} < e^{ikpz} >^{\pm}_{(n)} \mathbf{A}_{(n)} \quad n = 1,\ 2,\ \cdots,\ N \qquad (2.1\text{-}25)$$

where *n* denotes the variables associated with layer *n* and ± indicates the variables on the upper and lower surfaces of layer *n*, respectively, $\{\mathbf{P}^{\pm}_{(n)}\}^T = [u, v, w, \breve{\sigma}_z, \breve{\tau}_{yz}, \breve{\tau}_{xz}]^{\pm}_{(n)}$. The local

transfer matrix $\mathbf{G}_{(n)}$ is the 6×6 square matrix in Eq. (2.1-24), $< e^{ikpz} >^{\pm}_{(n)} = \mathrm{diag}(e^{ikp_1 z},\ e^{ikp_2 z},\ e^{ikp_3 z},\ e^{ikp_4 z},\ e^{ikp_5 z},\ e^{ikp_6 z})^{\pm}_{(n)}$, and $\mathbf{A}_{(n)} = \{A_1,\ A_2,\ A_3,\ A_4,\ A_5,\ A_6\}^T_{(n)}$. It may be easily seen that the local transfer matrix $\mathbf{G}_{(n)}$ depends on both material properties of layer *n* and wave number direction ϕ, but not function of *z*; while, in Eq. (2.1-25), only $< e^{ikpz} >^{\pm}_{(n)}$ is function of *z*.

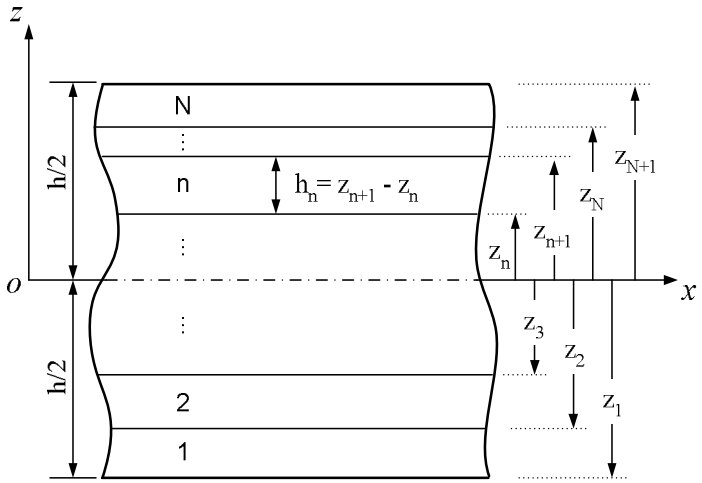

Figure 2.1 Geometry of an N-layered laminate

From $\mathbf{P}^{+}_{(n)} = \mathbf{G}_{(n)} < e^{ikpz} >^{+}_{(n)} \mathbf{A}_{(n)}$ and $\mathbf{P}^{-}_{(n)} = \mathbf{G}_{(n)} < e^{ikpz} >^{-}_{(n)} \mathbf{A}_{(n)}$, $\mathbf{A}_{(n)}$ can be eliminated and the following relation for layer *n* can be obtained

$$\mathbf{P}^{+}_{(n)} = \mathbf{T}_{(n)} \mathbf{P}^{-}_{(n)} \tag{2.1-26}$$

where $\mathbf{T}_{(n)} = \mathbf{G}_{(n)} < e^{ikpz} >^{+}_{(n)} [< e^{ikpz} >^{-}_{(n)}]^{-1} \mathbf{G}^{-1}_{(n)} = \mathbf{G}_{(n)} < e^{ikph_n} > \mathbf{G}^{-1}_{(n)}$, h_n is the thickness of layer *n* and *p* are associated with the specific layer *n*.

By applying the above procedure for each layer, followed by invoking the continuity of displacement and stress components at the layer interfaces namely, $\mathbf{P}^{+}_{(n)} = \mathbf{P}^{-}_{(n+1)}$, finally the

displacements and stresses on the upper surface of the layered plates, $z = +h/2$, can be related to its lower surface, $z = -h/2$ by

$$\mathbf{P}^{+} = \mathbf{T}\,\mathbf{P}^{-} \tag{2.1-27}$$

where $\mathbf{T} = \mathbf{T}_{(N)}\mathbf{T}_{(N-1)}\cdots\mathbf{T}_{(n)}\cdots\mathbf{T}_{(2)}\mathbf{T}_{(1)}$. In addition, $\mathbf{P}^{+}$ and $\mathbf{P}^{-}$ are now the displacement and stress column vectors on the top and bottom surfaces of the laminated plate.

Furthermore, for the traction-free boundary conditions on the top and bottom surfaces of plate, Eq. (2.1-4), and then Eq. (2.1-27) can be rewritten as:

$$\begin{Bmatrix} u^{+} \\ v^{+} \\ w^{+} \\ \hline 0 \\ 0 \\ 0 \end{Bmatrix} = \left[\begin{array}{ccc:ccc} T_{11} & T_{12} & T_{13} & T_{14} & T_{15} & T_{16} \\ T_{21} & T_{22} & T_{23} & T_{24} & T_{25} & T_{26} \\ T_{31} & T_{32} & T_{33} & T_{34} & T_{35} & T_{36} \\ \hdashline T_{41} & T_{42} & T_{43} & T_{44} & T_{45} & T_{46} \\ T_{51} & T_{52} & T_{53} & T_{54} & T_{55} & T_{56} \\ T_{61} & T_{62} & T_{63} & T_{64} & T_{65} & T_{66} \end{array}\right] \begin{Bmatrix} u^{-} \\ v^{-} \\ w^{-} \\ \hline 0 \\ 0 \\ 0 \end{Bmatrix} \tag{2.1-28}$$

For nontrivial solutions of Eq. (2.1-28), it yields the dispersion relations for elastic waves in the composite laminate:

$$\begin{vmatrix} T_{41} & T_{42} & T_{43} \\ T_{51} & T_{52} & T_{53} \\ T_{61} & T_{62} & T_{63} \end{vmatrix} = 0 \tag{2.1-29}$$

Dispersion relations Eq. (2.1-29) is a transcendental function implicitly relating the phase velocity with the wave frequency. It is not possible to solve it analytically in an explicit form; hence numerical root searching tools have to be used to find c_p for every frequency point at a given wave number direction.

It is of importance to note that Eq. (2.1-29) constitutes a generalization of the results Eq. (2.1-22) and (2.1-23) obtained for composite lamina. When the properties of all layers

are the same, Eq. (2.1-29) is expected to reduce to Eq. (2.1-22) for antisymmetric modes and Eq. (2.1-23) for symmetric modes. However, using this formulation even in symmetric laminates, it is unlikely to distinguish the antisymmetric and symmetric modes, since dispersion relations of all modes are mixed.

ASSEMBLE MATRIX METHOD

Boundary conditions on top and bottom surfaces of the laminated plate are:

$$(\sigma_z,\ \tau_{yz},\ \tau_{xz})\Big|_{z=\pm h/2} = 0 \tag{2.1-30}$$

where h is the thickness of the laminates.

Continuity conditions at the interface between the adjacent layers are given by

$$\mathbf{P}^{+}_{(n)} - \mathbf{P}^{-}_{(n+1)} = 0 \tag{2.1-31}$$

Eq. (2.1-30) and (2.1-31) can be assembled into a matrix form as follows:

$$\begin{Bmatrix} \Sigma^{+}_{(N)} \\ P^{-}_{(N)} - P^{+}_{(N-1)} \\ \vdots \\ P^{-}_{(n)} - P^{+}_{(n-1)} \\ \vdots \\ P^{-}_{(2)} - P^{+}_{(1)} \\ \Sigma^{-}_{(1)} \end{Bmatrix} = \begin{bmatrix} [\mathbf{G}_{(N)}\mathbf{D}^{+}_{(N)}]_{4\sim6} & & & & & & \\ \mathbf{G}_{(N)}\mathbf{D}^{-}_{(N)} & -\mathbf{G}_{(N-1)}\mathbf{D}^{+}_{(N-1)} & & & 0 & & \\ & \ddots & \ddots & & & & \\ & & \mathbf{G}_{(n+1)}\mathbf{D}^{-}_{(n+1)} & -\mathbf{G}_{(n)}\mathbf{D}^{+}_{(n)} & & & \\ & & & \ddots & \ddots & & \\ & 0 & & & \mathbf{G}_{(2)}\mathbf{D}^{-}_{(2)} & -\mathbf{G}_{(1)}\mathbf{D}^{+}_{(1)} & \\ & & & & & [\mathbf{G}_{(1)}\mathbf{D}^{-}_{(1)}]_{4\sim6} \end{bmatrix} \begin{Bmatrix} \mathbf{A}_{(N)} \\ \mathbf{A}_{(N-1)} \\ \vdots \\ \mathbf{A}_{(n)} \\ \vdots \\ \mathbf{A}_{(2)} \\ \mathbf{A}_{(1)} \end{Bmatrix} = 0 \tag{2.1-32}$$

where $\mathbf{D}^{\pm}_{(n)} = < e^{ikpz} >^{\pm}_{(n)}$, $\Sigma^{+}_{(N)} = (\breve{\sigma}_z,\ \breve{\tau}_{yz},\ \breve{\tau}_{xz})^T\Big|_{z=h/2}$ is the stress component column on the top surface of the laminated plate and $\Sigma^{-}_{(1)} = (\breve{\sigma}_z,\ \breve{\tau}_{yz},\ \breve{\tau}_{xz})^T\Big|_{z=-h/2}$ is the stress components on the bottom surface, moreover the operator $[\ ]_{4\sim6}$ denotes extracting last three rows from the matrix in Eq. (2.1-24), thus both the first submatrix in the first row and last submatrix in the last row are 3×6 matrix. As shown in Eq. (2.1-32), the assembled matrix is divided into *N+1* by *N* submatrices and actually it is a $6N\times6N$ square matrix.

For nontrivial solutions of Eq. (2.1-32), the determinant of assembled matrix must vanish and consequently the dispersion relations for elastic waves in a laminated composite plate is

$$\det\begin{bmatrix} [\mathbf{G}_{(N)}\mathbf{D}^{+}_{(N)}]_{4\sim6} & & & & & \\ \mathbf{G}_{(N)}\mathbf{D}^{-}_{(N)} & -\mathbf{G}_{(N-1)}\mathbf{D}^{+}_{(N-1)} & & & 0 & \\ & \ddots & \ddots & & & \\ & & \mathbf{G}_{(n+1)}\mathbf{D}^{-}_{(n+1)} & -\mathbf{G}_{(n)}\mathbf{D}^{+}_{(n)} & & \\ & & & \ddots & \ddots & \\ & 0 & & & \mathbf{G}_{(2)}\mathbf{D}^{-}_{(2)} & -\mathbf{G}_{(1)}\mathbf{D}^{+}_{(1)} \\ & & & & & [\mathbf{G}_{(1)}\mathbf{D}^{-}_{(1)}]_{4\sim6} \end{bmatrix} = 0 \quad (2.1\text{-}33)$$

Although Eq. (2.1-33) is apparently different with Eq. (2.1-29) based on transfer matrix, both of them will yield the same dispersion results since they are deduced from the same traction-free surfaces and interface continuity conditions. Similar to Eq. (2.1-29), when the material properties and fiber orientation of all layers are the same, Eq. (2.1-33) is expected to reduce to Eq. (2.1-22) and Eq. (2.1-23). Additionally, both symmetric modes and antisymmetric mode will be mixed together in the same manner as the transfer matrix method.

SEPARATION OF SYMMETRIC AND ANTISYMMETRIC MODES

Although both transfer matrix method and assemble matrix method can directly calculate a general laminate with an arbitrary stacking sequence, it is unlikely to distinguish the symmetric and antisymmetric modes, even in a symmetric laminate. In order to overcome this shortcoming, a method is developed to decouple symmetric and antisymmetric modes in a symmetric laminate by imposing boundary conditions at the mid-plane of the plate. It is

worth of noting that this method is only valid for symmetric laminates, not as general as the transfer matrix method and assemble matrix method.

For elastic waves in a symmetric laminate, boundary conditions on the top surfaces of the laminate are

$$(\sigma_z,\ \tau_{yz},\ \tau_{xz})\Big|_{z=h/2} = 0 \tag{2.1-34}$$

where h is the thickness of the laminate.

Continuity conditions at the interface between the adjacent layers are expressed in Eq. (2.1-31). Because of the symmetric structure of the laminate, one can consider only half of the laminate and then impose the symmetric or antisymmetric conditions on the stress and displacement components at the mid-plane.

For symmetric modes, the boundary conditions at mid-plane can be expressed as

$$(w,\ \tau_{yz},\ \tau_{xz})\Big|_{z=0} = 0 \tag{2.1-35}$$

Then these boundary conditions of the half-plate can be assembled into a matrix form:

$$\begin{Bmatrix} \Sigma^{+}_{(N)} \\ P^{-}_{(N)} - P^{+}_{(N-1)} \\ \vdots \\ P^{-}_{(n)} - P^{+}_{(n-1)} \\ \vdots \\ P^{-}_{(N/2+1)} - P^{+}_{(N/2+1)} \\ \Sigma^{-}_{(N/2)} \end{Bmatrix} = \begin{bmatrix} [\mathbf{G}_{(N)}\mathbf{D}^{+}_{(N)}]_{4\sim6} & & & & & & \\ \mathbf{G}_{(N)}\mathbf{D}^{-}_{(N)} & -\mathbf{G}_{(N-1)}\mathbf{D}^{+}_{(N-1)} & & & 0 & & \\ & \ddots & \ddots & & & & \\ & & \mathbf{G}_{(n+1)}\mathbf{D}^{-}_{(n+1)} & -\mathbf{G}_{(n)}\mathbf{D}^{+}_{(n)} & & & \\ & & & \ddots & \ddots & & \\ & 0 & & & \mathbf{G}_{(N/2+1)}\mathbf{D}^{-}_{(N/2+1)} & -\mathbf{G}_{(N/2+1)}\mathbf{D}^{+}_{(N/2+1)} & \\ & & & & & [\mathbf{G}_{(N/2)}\mathbf{D}^{-}_{(N/2)}]_{3,5,6} & \end{bmatrix} \begin{Bmatrix} \mathbf{A}_{(N)} \\ \mathbf{A}_{(N-1)} \\ \vdots \\ \mathbf{A}_{(n)} \\ \vdots \\ \mathbf{A}_{(N/2+1)} \\ \mathbf{A}_{(N/2)} \end{Bmatrix} = 0 \tag{2.1-36}$$

where $\mathbf{D}^{\pm}_{(n)} = < e^{ikpz} >^{\pm}_{(n)}$, $\Sigma^{+}_{(N)} = (\breve{\sigma}_z,\ \breve{\tau}_{yz},\ \breve{\tau}_{xz})^T\Big|_{z=h/2}$ are the stress components on the top surface and $\Sigma^{-}_{(N/2)} = (w,\ \breve{\tau}_{yz},\ \breve{\tau}_{xz})^T\Big|_{z=0}$ are the stress and displacement components on the middle plane, moreover operator $[\ ]_{4\sim6}$ denotes extracting last three rows from the matrix in Eq. (2.1-24), similarly $[\ ]_{3,5,6}$ indicates the third, fifth, and sixth rows of Eq. (2.1-24).

For nontrivial solutions of Eq. (2.1-36), the determinant of the matrix in Eq. (2.1-36) must be zero and consequently the dispersion relations for symmetric waves in a laminated composite plate can be numerically obtained.

Likewise, the boundary conditions of antisymmetric modes on the mid-plane are

$$(u,\ v,\ \sigma_z)\big|_{z=0} = 0 \tag{2.1-37}$$

The assembled boundary condition matrix form of the half-plate has the following expression

$$\begin{Bmatrix} \boldsymbol{\Sigma}^{+}_{(N)} \\ P^{-}_{(N)} - P^{+}_{(N-1)} \\ \vdots \\ P^{-}_{(n)} - P^{+}_{(n-1)} \\ \vdots \\ P^{-}_{(N/2+1)} - P^{+}_{(N/2+1)} \\ \boldsymbol{\Sigma}^{-}_{(N/2)} \end{Bmatrix} = \begin{bmatrix} [\mathbf{G}_{(N)}\mathbf{D}^{+}_{(N)}]_{4\sim 6} & & & & & \\ \mathbf{G}_{(N)}\mathbf{D}^{-}_{(N)} & -\mathbf{G}_{(N-1)}\mathbf{D}^{+}_{(N-1)} & & & 0 & \\ & \ddots & \ddots & & & \\ & & \mathbf{G}_{(n+1)}\mathbf{D}^{-}_{(n+1)} & -\mathbf{G}_{(n)}\mathbf{D}^{+}_{(n)} & & \\ & & & \ddots & \ddots & \\ & 0 & & & \mathbf{G}_{(N/2+1)}\mathbf{D}^{-}_{(N/2+1)} & -\mathbf{G}_{(N/2+1)}\mathbf{D}^{+}_{(N/2+1)} \\ & & & & & [\mathbf{G}_{(N/2)}\mathbf{D}^{-}_{(N/2)}]_{1,2,4} \end{bmatrix} \begin{Bmatrix} \mathbf{A}_{(N)} \\ \mathbf{A}_{(N-1)} \\ \vdots \\ \mathbf{A}_{(n)} \\ \vdots \\ \mathbf{A}_{(N/2+1)} \\ \mathbf{A}_{(N/2)} \end{Bmatrix} = 0 \tag{2.1-38}$$

where $\boldsymbol{\Sigma}^{-}_{(N/2)} = (u,\ v,\ \breve{\sigma}_z)^T\big|_{z=0}$ are the stress and displacement components on the middle plane, operator $[\ ]_{1,2,4}$ denotes extracting the first, second and forth rows from the matrix in Eq. (2.1-24).

To guarantee nontrivial solutions of Eq. (2.1-38), the determinant of the matrix in Eq. (2.1-38) should be zero. After numerically solving the determinant equation, the dispersion relations for antisymmetric waves in a laminated composite plate are obtained.

Note that the method can be also used to calculate dispersion relations for a one-layered plate (or composite lamina) case, when layer number $N = 1$, or the material properties and fiber orientation of all layers are the same.

2.2 Transient Waves in Composites Based on a Higher-order Plate Theory

The classical plate theory (CPT) is based on Kirchhoff hypothesis, which assumes that straight lines perpendicular to the mid-plane before deformation remain straight and normal to the mid-plane after deformation, and hence neglects transverse shear deformation effects. However, these effects may become significant in the case of composite laminates due to the relatively low transverse shear modulus. Further in analyzing transient wave behavior in composites, classical Kirchhoff plate theory is valid in the low frequency range or wavelength much greater than the plate thickness; a higher-order plate theory should be used in the higher frequency range, where the wavelength is smaller. Accordingly, if the effects of transverse shear deformation and rotary inertia are taken into account, the CPT evolves into first-order shear deformation plate theory (SDPT), or so-called Mindlin plate theory.

Compared with Mindlin plate theory, higher-order plate theory can represent the kinematics better and yield more accurate inter-lamina stress distributions. However, it involve considerably more computational effort. In principle, it is possible to expand the displacement field in terms of the thickness coordinate up to any desired degree. Due to the algebraic complexity and computational cost involved with higher-order plate theory in return for marginal gain in accuracy, theory higher than third-order has not been attempted.

In this section, the theory of reference (Whitney and Sun, 1973) is extended to include the first symmetric thickness shear and thickness stretch modes by including higher-order terms in the displacement expansion about the mid-plane of the laminate in a manner similar to that of Kane and Mindlin (1956) for homogeneous isotropic plates. The governing equations reveal that unsymmetrically laminated plates display a coupling phenomenon

among all the deformation modes. Also, the dispersion relations of both symmetric and antisymmetric waves in symmetrically laminated plate are obtained.

2.2.1 Constitutive relations

Considering an infinite plate of constant thickness *h* composed of thin layers of anisotropic material bonded together. The origin of a Cartesian coordinate system is located in the central *x*-*y* plane with the *z*-axis being normal to this plane. The material of each layer is assumed to possess a plane of elastic symmetry parallel to *xy* as shown in Figure 2.2.

Stress and moment resultants per unit length are defined as in the following:

$$(N_x, N_y, N_z, N_{xy}, Q_x, Q_y) = \int_{-h/2}^{h/2} (\sigma_x, \sigma_y, \sigma_z, \tau_{xy}, \tau_{xz}, \tau_{yz})\, dz \tag{2.2-1a}$$

$$(M_x, M_y, M_{xy}, R_x, R_y) = \int_{-h/2}^{h/2} (\sigma_x, \sigma_y, \tau_{xy}, \tau_{xz}, \tau_{yz})\, z dz \tag{2.2-1b}$$

$$(S_x, S_y, S_{xy}) = \frac{1}{2}\int_{-h/2}^{h/2} (\sigma_x, \sigma_y, \tau_{xy})\, z^2 dz \tag{2.2-1c}$$

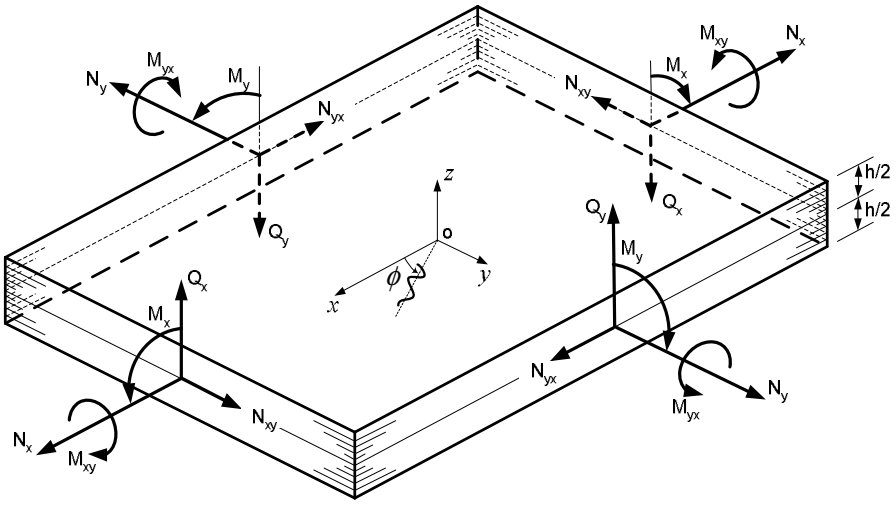

Figure 2.2 Force and moment resultants on a laminated composite plate

For a laminated composite plate with surfaces on $z = \pm h/2$ and the stress-strain relations for the monoclinic material with respect to *z* axis are given by:

$$\begin{Bmatrix} \sigma_x \\ \sigma_y \\ \sigma_z \\ \tau_{yz} \\ \tau_{xz} \\ \tau_{xy} \end{Bmatrix} = \begin{bmatrix} C_{11} & C_{12} & C_{13} & 0 & 0 & C_{16} \\ C_{12} & C_{22} & C_{23} & 0 & 0 & C_{26} \\ C_{13} & C_{23} & C_{33} & 0 & 0 & C_{36} \\ 0 & 0 & 0 & C_{44} & C_{45} & 0 \\ 0 & 0 & 0 & C_{45} & C_{55} & 0 \\ C_{16} & C_{26} & C_{36} & 0 & 0 & C_{66} \end{bmatrix} \begin{Bmatrix} \varepsilon_x \\ \varepsilon_y \\ \varepsilon_z \\ \gamma_{yz} \\ \gamma_{xz} \\ \gamma_{xy} \end{Bmatrix} \tag{2.2-2}$$

Note that the symmetric waves behavior based on CPT are not dispersive and may not hold for analyzing ultrasonic symmetric waves propagating in composites. In this study, a higher-order deformation theory, which takes into account the first symmetric thickness shear, the thickness extension motions, is used to model the symmetric waves propagating in a thin composite plate.

The displacement field in the *x*, *y*, and *z* directions of a plate can be described by

$$u(x, y, z, t) = u_0(x, y, t) + z\psi_x(x, y, t) + \frac{z^2}{2}\phi_x(x, y, t) \tag{2.2-3a}$$

$$v(x, y, z, t) = v_0(x, y, t) + z\psi_y(x, y, t) + \frac{z^2}{2}\phi_y(x, y, t) \tag{2.2-3b}$$

$$w(x, y, z, t) = w_0(x, y, t) + z\psi_z(x, y, t) \tag{2.2-3c}$$

where u_0, v_0 and w_0 represent the displacements of every point of the mid-plane of the plate, ψ_x and ψ_y physically are the rotations of the rotations of section *x* = constant and *y* = constant respectively. Eq. (2.2-3) in conjunction with the strain-displacement relations of classical theory of elasticity leads to the following relations:

$$\varepsilon_x = \varepsilon_{0x} + z\psi_{x,x} + \frac{z^2}{2}\phi_{x,x} \tag{2.2-4a}$$

$$\varepsilon_y = \varepsilon_{0y} + z\psi_{y,y} + \frac{z^2}{2}\phi_{y,y} \tag{2.2-4b}$$

$$\varepsilon_z = \varepsilon_{0z} \tag{2.2-4c}$$

$$\gamma_{xy} = \gamma_{0xy} + z(\psi_{x,y} + \psi_{y,x}) + \frac{z^2}{2}(\phi_{x,y} + \phi_{y,x}) \tag{2.2-4e}$$

$$\gamma_{xz} = \gamma_{0xz} + z(\phi_x + \psi_{z,x}) \tag{2.2-4f}$$

$$\gamma_{yz} = \gamma_{0yz} + z(\phi_y + \psi_{z,y}) \tag{2.2-4g}$$

where partial differential is denoted by a comma and

$$\varepsilon_{0x} = u_{0,x},\ \ \varepsilon_{0y} = v_{0,y},\ \ \varepsilon_{0z} = \psi_z,\ \ \gamma_{0xy} = u_{0,y} + v_{0,x},\ \ \gamma_{0xz} = \psi_x + w_{0,x},\ \ \gamma_{0yz} = \psi_y + w_{0,y} \tag{2.2-5}$$

In order to improve the results obtained from the displacement assumptions of Eq. (2.2-3), parameters κ_i are introduced in manner similar to that of Mindlin and Medick (1959) for homogeneous isotropic plates, the following substitutions are made:

$$\kappa_1\gamma_{0xz} \text{ for } \gamma_{0xz}, \qquad \kappa_2\gamma_{0yz} \text{ for } \gamma_{0yz}, \qquad \kappa_3\varepsilon_{0z} \text{ for } \varepsilon_{0z},$$

$$\kappa_4(\phi_x + \psi_{z,x}) \text{ for } (\phi_x + \psi_{z,x}), \quad \text{and} \quad \kappa_5(\phi_y + \psi_{z,y}) \text{ for } (\phi_y + \psi_{z,y})$$

$\kappa_1, \cdots, \kappa_6$ will be determined in the next section. Substituting Eq. (2.2-4) into (2.2-2) and putting the results into Eq. (2.2-1) yield the following plate constitutive relations:

$$\begin{Bmatrix} N_x \\ N_y \\ N_z \\ N_{xy} \\ \hline M_x \\ M_y \\ M_{xy} \\ \hline S_x \\ S_y \\ S_{xy} \end{Bmatrix} = \left[\begin{array}{cccc:ccc:ccc} A_{11} & A_{12} & \kappa_3 A_{13} & A_{16} & B_{11} & B_{12} & B_{16} & D_{11}/2 & D_{12}/2 & D_{16}/2 \\ A_{12} & A_{22} & \kappa_3 A_{23} & A_{26} & B_{12} & B_{22} & B_{26} & D_{12}/2 & D_{22}/2 & D_{26}/2 \\ \kappa_3 A_{13} & \kappa_3 A_{23} & \kappa_3^2 A_{33} & \kappa_3 A_{36} & \kappa_3 B_{13} & \kappa_3 B_{23} & \kappa_3 B_{36} & \kappa_3 D_{13}/2 & \kappa_3 D_{23}/2 & \kappa_3 D_{36}/2 \\ A_{16} & A_{26} & \kappa_3 A_{36} & A_{66} & B_{16} & B_{26} & B_{66} & D_{16}/2 & D_{26}/2 & D_{66}/2 \\ \hdashline B_{11} & B_{12} & \kappa_3 B_{13} & B_{16} & D_{11} & D_{12} & D_{16} & F_{11}/2 & F_{12}/2 & F_{16}/2 \\ B_{12} & B_{22} & \kappa_3 B_{23} & B_{26} & D_{12} & D_{22} & D_{26} & F_{12}/2 & F_{22}/2 & F_{26}/2 \\ B_{16} & B_{26} & \kappa_3 B_{36} & B_{66} & D_{16} & D_{26} & D_{66} & F_{16}/2 & F_{26}/2 & F_{66}/2 \\ \hdashline D_{11}/2 & D_{12}/2 & \kappa_3 D_{13}/2 & D_{16}/2 & F_{11}/2 & F_{12}/2 & F_{16}/2 & H_{11}/4 & H_{12}/4 & H_{16}/4 \\ D_{12}/2 & D_{22}/2 & \kappa_3 D_{23}/2 & D_{26}/2 & F_{12}/2 & F_{22}/2 & F_{26}/2 & H_{12}/4 & H_{22}/4 & H_{26}/4 \\ D_{16}/2 & D_{26}/2 & \kappa_3 D_{36}/2 & D_{66}/2 & F_{16}/2 & F_{26}/2 & F_{66}/2 & H_{16}/4 & H_{26}/4 & H_{66}/4 \end{array}\right] \begin{Bmatrix} u_{0,x} \\ v_{0,y} \\ \psi_z \\ u_{0,y} + v_{0,x} \\ \hline \psi_{x,x} \\ \psi_{y,y} \\ \psi_{x,y} + \psi_{y,x} \\ \hline \phi_{x,x} \\ \phi_{y,y} \\ \phi_{x,y} + \phi_{y,x} \end{Bmatrix} \tag{2.2-6}$$

$$\left\{\begin{array}{c} Q_x \\ Q_y \\ \hline R_x \\ R_y \end{array}\right\} = \left[\begin{array}{cc:cc} \kappa_1^2 A_{55} & \kappa_1\kappa_2 A_{45} & \kappa_1\kappa_4 B_{55} & \kappa_1\kappa_5 B_{45} \\ \kappa_1\kappa_2 A_{45} & \kappa_2^2 A_{44} & \kappa_2\kappa_4 B_{45} & \kappa_2\kappa_5 B_{44} \\ \hdashline \kappa_1\kappa_4 B_{55} & \kappa_2\kappa_4 B_{45} & \kappa_4^2 D_{55} & \kappa_4\kappa_5 D_{45} \\ \kappa_1\kappa_5 B_{45} & \kappa_2\kappa_5 B_{44} & \kappa_4\kappa_5 D_{45} & \kappa_5^2 D_{44} \end{array}\right] \left\{\begin{array}{c} \psi_x + w_{0,x} \\ \psi_y + w_{0,y} \\ \hline \psi_{z,x} + \phi_x \\ \psi_{z,y} + \phi_y \end{array}\right\} \tag{2.2-7}$$

where $(A_{ij}, B_{ij}, D_{ij}, F_{ij}, H_{ij}) = \int_{-h/2}^{h/2} C_{ij}(1,\ z,\ z^2,\ z^3,\ z^4)\, dz$ and h is the laminate thickness. The usual coupling between antisymmetric and symmetric modes for a laminate of arbitrary stacking sequence in Eq. (2.2-6) is through the stiffness B_{ij} and F_{ij}.

With the linear strain-displacement relations, the equations of motion of the higher-order theory can be derived using the principle of virtual displacement or Hamilton's principle (e.g., Washizu, 1982)

$$0 = \int_{t_1}^{t_2} (\delta U + \delta V - \delta K) dt \tag{2.2-8}$$

where is δU the virtual strain energy, δV virtual work done by applied force, and δK the virtual kinetic energy. A set of equations of motion is

$$\frac{\partial N_x}{\partial x} + \frac{\partial N_{xy}}{\partial y} + q_x = I_0 \frac{\partial^2 u_0}{\partial t^2} + \frac{I_2}{2} \frac{\partial^2 \phi_x}{\partial t^2} \tag{2.2-9a}$$

$$\frac{\partial N_{xy}}{\partial x} + \frac{\partial N_y}{\partial y} + q_y = I_0 \frac{\partial^2 v_0}{\partial t^2} + \frac{I_2}{2} \frac{\partial^2 \phi_y}{\partial t^2} \tag{2.2-9b}$$

$$\frac{\partial Q_x}{\partial x} + \frac{\partial Q_y}{\partial y} + q = I_0 \frac{\partial^2 w_0}{\partial t^2} \tag{2.2-9c}$$

$$\frac{\partial M_x}{\partial x} + \frac{\partial M_{xy}}{\partial y} - Q_x + m_x = \frac{I_2}{2} \frac{\partial^2 \psi_x}{\partial t^2} \tag{2.2-9d}$$

$$\frac{\partial M_{xy}}{\partial x} + \frac{\partial M_y}{\partial y} - Q_y + m_y = \frac{I_2}{2} \frac{\partial^2 \psi_y}{\partial t^2} \tag{2.2-9e}$$

$$\frac{\partial R_x}{\partial x}+\frac{\partial R_y}{\partial y}-N_z+m=I_2\frac{\partial^2\psi_z}{\partial t^2} \tag{2.2-9f}$$

$$\frac{\partial S_x}{\partial x}+\frac{\partial S_{xy}}{\partial y}-R_z+n_x=\frac{I_0}{2}\frac{\partial^2 u_0}{\partial t^2}+\frac{I_4}{4}\frac{\partial^2\phi_x}{\partial t^2} \tag{2.2-9g}$$

$$\frac{\partial S_{xy}}{\partial x}+\frac{\partial S_y}{\partial y}-R_y+n_y=\frac{I_0}{2}\frac{\partial^2 v_0}{\partial t^2}+\frac{I_4}{4}\frac{\partial^2\phi_y}{\partial t^2} \tag{2.2-9h}$$

where $(I_0,\ I_1,\ I_2,\ I_3,\ I_4)=\int_{-h/2}^{h/2}\rho(1,\ z,\ z^2,\ z^3,\ z^4)\,dz$.

By assuming the solution form as

$$\begin{aligned}
u_0&=U_0e^{i[(k_1x+k_2y)-\omega t]}\\
v_0&=V_0e^{i[(k_1x+k_2y)-\omega t]}\\
w_0&=W_0e^{i[(k_1x+k_2y)-\omega t]}\\
\psi_z&=\Psi_ze^{i[(k_1x+k_2y)-\omega t]}\\
\phi_x&=\Phi_xe^{i[(k_1x+k_2y)-\omega t]}\\
\phi_y&=\Phi_ye^{i[(k_1x+k_2y)-\omega t]}\\
\psi_x&=\Psi_xe^{i[(k_1x+k_2y)-\omega t]}\\
\psi_y&=\Psi_ye^{i[(k_1x+k_2y)-\omega t]}
\end{aligned} \tag{2.2-10}$$

Substituting Eq. (2.2-6), (2.2-7), and (2.2-10) into Eq. (2.2-9) yields the following displacement equations of motion:

$$\begin{bmatrix} L_{11} & L_{12} & 0 & L_{14} & L_{15} & L_{16} & L_{17} & L_{18} \\ L_{12} & L_{22} & 0 & L_{15} & L_{25} & L_{26} & L_{18} & L_{28} \\ 0 & 0 & L_{33} & L_{34} & L_{35} & L_{36} & L_{37} & L_{38} \\ L_{14} & L_{15} & L_{34} & L_{44} & L_{45} & L_{46} & L_{47} & L_{48} \\ L_{15} & L_{25} & L_{35} & L_{45} & L_{55} & L_{56} & L_{57} & L_{58} \\ L_{16} & L_{26} & L_{36} & L_{46} & L_{56} & L_{66} & L_{67} & L_{68} \\ L_{17} & L_{18} & L_{37} & L_{47} & L_{57} & L_{67} & L_{77} & L_{78} \\ L_{18} & L_{28} & L_{38} & L_{48} & L_{58} & L_{68} & L_{78} & L_{88} \end{bmatrix} \begin{Bmatrix} U_0 \\ V_0 \\ W_0 \\ \Psi_x \\ \Psi_y \\ \Psi_z \\ \Phi_x \\ \Phi_y \end{Bmatrix} = 0 \qquad (2.2\text{-}11)$$

where the coefficients L_{ij} are defined in the following manner:

$$L_{11} = A_{11}k_x^2 + 2A_{16}k_xk_y + A_{66}k_y^2 - \omega^2 I_0$$

$$L_{12} = A_{16}k_x^2 + (A_{12} + A_{66})k_xk_y + A_{26}k_y^2$$

$$L_{14} = B_{11}k_x^2 + 2B_{16}k_xk_y + B_{66}k_y^2 - \omega^2 I_1$$

$$L_{15} = B_{16}k_x^2 + (B_{12} + B_{66})k_xk_y + B_{26}k_y^2$$

$$L_{16} = -i\kappa_3(A_{13}k_x + A_{36}k_y)$$

$$L_{17} = \frac{1}{2}(D_{11}k_x^2 + 2D_{16}k_xk_y + D_{66}k_y^2 - \omega^2 I_2)$$

$$L_{18} = \frac{1}{2}[D_{16}k_x^2 + (D_{12} + D_{66})k_xk_y + D_{26}k_y^2]$$

$$L_{22} = A_{66}k_x^2 + 2A_{26}k_xk_y + A_{22}k_y^2 - \omega^2 I_0$$

$$L_{25} = B_{66}k_x^2 + 2B_{26}k_xk_y + B_{22}k_y^2 - \omega^2 I_1$$

$$L_{26} = -i\kappa_3(A_{36}k_x + A_{23}k_y)$$

$$L_{28} = \frac{1}{2}(D_{66}k_x^2 + 2D_{26}k_xk_y + D_{22}k_y^2 - \omega^2 I_2)$$

$$L_{33} = -(\kappa_1^2 A_{55} k_x^2 + 2\kappa_1\kappa_2 A_{45} k_x k_y + \kappa_2^2 A_{44} k_y^2 - \omega^2 I_0)$$

$$L_{34} = i\kappa_1(\kappa_1 A_{55} k_x + \kappa_2 A_{45} k_y)$$

$$L_{35} = i\kappa_2(\kappa_1 A_{45} k_x + \kappa_2 A_{44} k_y)$$

$$L_{36} = -[\kappa_1\kappa_4 B_{55} k_x^2 + (\kappa_1\kappa_5 + \kappa_2\kappa_4) B_{45} k_x k_y + \kappa_2\kappa_5 B_{44} k_y^2 - \omega^2 I_1]$$

$$L_{37} = i\kappa_4(\kappa_1 B_{55} k_x + \kappa_2 B_{45} k_y)$$

$$L_{38} = i\kappa_5(\kappa_1 B_{45} k_x + \kappa_2 B_{44} k_y)$$

$$L_{44} = D_{11} k_x^2 + 2D_{16} k_x k_y + D_{66} k_y^2 + \kappa_1^2 A_{55} - \omega^2 I_2$$

$$L_{45} = D_{16} k_x^2 + (D_{12} + D_{66}) k_x k_y + D_{26} k_y^2 + \kappa_1\kappa_2 A_{45}$$

$$L_{46} = i(\kappa_1\kappa_4 B_{55} - \kappa_3 B_{13}) k_x + i(\kappa_1\kappa_5 B_{45} - \kappa_3 B_{36}) k_y$$

$$L_{47} = \frac{1}{2}(F_{11} k_x^2 + 2F_{16} k_x k_y + F_{66} k_y^2 + 2\kappa_1\kappa_4 B_{55} - \omega^2 I_3)$$

$$L_{48} = \frac{1}{2}[F_{16} k_x^2 + (F_{12} + F_{66}) k_x k_y + F_{26} k_y^2 + 2\kappa_1\kappa_5 B_{45}]$$

$$L_{55} = D_{66} k_x^2 + 2D_{26} k_x k_y + D_{22} k_y^2 + \kappa_2^2 A_{44} - \omega^2 I_2$$

$$L_{56} = i(\kappa_2\kappa_4 B_{45} - \kappa_3 B_{36}) k_x + i(\kappa_2\kappa_5 B_{44} - \kappa_3 B_{23}) k_y$$

$$L_{57} = \frac{1}{2}[F_{16} k_x^2 + (F_{12} + F_{66}) k_x k_y + F_{26} k_y^2 + 2\kappa_2\kappa_4 B_{45}]$$

$$L_{58} = \frac{1}{2}(F_{66} k_x^2 + 2F_{26} k_x k_y + F_{22} k_y^2 + 2\kappa_2\kappa_4 B_{44} - \omega^2 I_3)$$

$$L_{66} = -\kappa_4^2 D_{55} k_x^2 - 2\kappa_4\kappa_5 D_{45} k_x k_y - D_{44}\kappa_5^2 k_y^2 - \kappa_3^2 A_{33} + \omega^2 I_2$$

$$L_{67} = i(\kappa_4^2 D_{55} - \kappa_3 \frac{D_{13}}{2}) k_x + i(\kappa_4\kappa_5 D_{45} - \kappa_3 \frac{D_{36}}{2}) k_y$$

$$L_{68} = i(\kappa_4\kappa_5 D_{45} - \kappa_3 \frac{D_{36}}{2})k_x + i(\kappa_5^2 D_{44} - \kappa_3 \frac{D_{23}}{2})k_y$$

$$L_{77} = \frac{1}{4}(H_{11}k_x^2 + 2H_{16}k_x k_y + H_{66}k_y^2 + 4\kappa_4^2 D_{55} - \omega^2 I_4)$$

$$L_{78} = \frac{1}{4}[H_{16}k_x^2 + (H_{12} + H_{66})k_x k_y + H_{26}k_y^2 + 4\kappa_4\kappa_5 D_{45}]$$

$$L_{88} = \frac{1}{4}(H_{66}k_x^2 + 2H_{26}k_x k_y + H_{22}k_y^2 + 4\kappa_5^2 D_{44} - \omega^2 I_4)$$

For symmetric laminates $B_{ij} = F_{ij} = 0$, which leads to L_{15}, L_{37}, L_{38}, L_{48}, L_{56}, and L_{57} equal to zero, and Eq. (2.2-10) is decoupled into symmetric waves:

$$\begin{bmatrix} L_{11} & L_{12} & L_{16} & L_{17} & L_{18} \\ L_{12} & L_{22} & L_{26} & L_{18} & L_{28} \\ L_{16} & L_{26} & L_{66} & L_{67} & L_{68} \\ L_{17} & L_{18} & L_{67} & L_{77} & L_{78} \\ L_{18} & L_{28} & L_{68} & L_{78} & L_{88} \end{bmatrix} \begin{Bmatrix} U_0 \\ V_0 \\ \Psi_z \\ \Phi_x \\ \Phi_y \end{Bmatrix} = 0 \qquad (2.2\text{-}12)$$

and antisymmetric waves:

$$\begin{bmatrix} L_{33} & L_{34} & L_{35} \\ L_{34} & L_{44} & L_{45} \\ L_{35} & L_{45} & L_{55} \end{bmatrix} \begin{Bmatrix} W_0 \\ \Psi_x \\ \Psi_y \end{Bmatrix} = 0 \qquad (2.2\text{-}13)$$

The elements of L_{ij} matrix are function of k_x, k_y, ω and ϕ.

The phase velocity c_p is defined as $c_p = \omega/k$. Substituting k_x and k_y with k and ϕ in dispersion relations of symmetric waves Eq. (2.2-12) or dispersion relations of antisymmetric waves Eq. (2.2-13), a tenth-order polynomial equation in terms of k or a fifth-order equation in terms of k^2 can be obtained for symmetric waves. Similarly, a sixth-order

polynomial equation in terms of k or a cubic equation in terms of k^2 can be obtained for antisymmetric waves. For a fixed wave propagation direction ϕ and at a given angular frequency $\omega = 2\pi f$, the corresponding wave number k can be solved from the polynomial equations above then considering the definition $c_p = \omega/k$, the dispersion curves of both symmetric and antisymmetric waves may be obtained respectively.

2.2.2 Determination of κ_i

The fundamental procedure for determining κ_i in a dynamic problem is to match specific frequencies calculated from the approximate plate theory to frequencies obtained from 3-D elasticity solutions. As for the general case of composite laminates, this procedure becomes very tedious since the value of the correction factors will depend on the stacking sequence and the number of layers as well as the lamina properties (Whitney and Sun, 1973). In fact, with an increasing number of layers, the procedure becomes very cumbersome to compute solutions from 3-D elasticity solutions. Since the objective of using plate theory is to approximate the 3-D elasticity solutions in a tractable manner, it becomes self-conflicting to develop an elaborate mechanism for obtaining shear correction factors κ_i.

According to Sun and Whitney (1972) and Kulkarni and Pagano (1972), the first flexural mode of vibration, which is determined from the plate theory (Whitney and Pagano, 1970) for laminates having similar transverse shear moduli of the constituent layer, can be closely matched to the exact dynamic elasticity solution by choosing $\kappa_1^2 = \kappa_2^2 = \pi^2/12$. For unsymmetrical laminates, the higher-order kinematic terms of the present theory should have little effect on the first flexural mode. Therefore both κ_1^2 and κ_2^2 are selected as $\pi^2/12$ in the plate theory.

Kane and Mindlin (1956) determined κ_3 for their in-plane extensional plate theory by matching the cut-off frequency of the first thickness stretch mode to the exact dynamic elasticity solution. For laminates having each layer constructed of the same material, but not necessarily the same fiber orientation, C_{33} is an invariant property (Tsai and Pagano, 1968), and the procedure employed by Kane and Mindlin on homogeneous plates applied to the present theory yields the same results for such laminated composites. Accordingly, in this study κ_3^2 is chosen as $\pi^2/12$, the same value obtained by Kane and Mindlin (1956).

Mindlin and Medick (1959) calculated $\kappa_4^2 = \kappa_5^2 = \pi^2/15$ by matching the first cut-off frequency of the first symmetric thickness shear mode obtained from their homogeneous isotropic extensional plate theory to the exact dynamic elasticity solutions (Mindlin and Medick, 1959). Also, this same procedure can be applied to laminated plates. As mentioned before, such procedure becomes rather complex for laminates with a large number of layers. In addition, preliminary calculations indicate that any refinements in the determination of κ_4 and κ_5 yield marginal improvement in the numerical results. Therefore, in this study both κ_4^2 and κ_5^2 are chosen as $\pi^2/15$.

2.3 Phase and Group Velocity

2.3.1 Concepts of phase and group velocity

The concept of the phase and group velocity of waves is presented in this section. Group velocity is associated with the propagation velocity of a group of waves with similar frequency. The simplest analytical explanation (Stroke, 1876) in one-dimensional case is to consider two propagating harmonic waves of equal amplitude but of slightly different frequency, ω_1 and ω_2. Then wave signal $w(x, t)$ can be superimpose with the two waves

$$w(x,t) = A\cos(k_1 x - \omega_1 t) + A\cos(k_2 x - \omega_2 t) \tag{2.3-1}$$

Using trigonometric identities, we can rewrite Eq. (2.3-1) as

$$w(x,t) = 2A\cos(\frac{k_2 - k_1}{2}x - \frac{\omega_2 - \omega_1}{2}t)\times\cos(\frac{k_2 + k_1}{2}x - \frac{\omega_2 + \omega_1}{2}t) \tag{2.3-2}$$

Noting that the cosine is an even function, we now make the following substitutions:

$$\Delta\omega = \frac{\omega_2 - \omega_1}{2},\ \Delta k = \frac{k_2 - k_1}{2},\ \omega = \frac{\omega_2 + \omega_1}{2},\ k = \frac{k_2 + k_1}{2} \tag{2.3-3}$$

Hence,

$$w(x,t) = 2A\underbrace{\cos(\Delta kx - \Delta\omega t)}_{\text{low-frequency term}}\times\underbrace{\cos(kx - \omega t)}_{\text{high-frequency term}} \tag{2.3-4}$$

This represents a carrier with high-frequency component ω and a phase velocity $c_p = \omega / k$, and the modulation $\cos(\Delta kx - \Delta\omega t)$ with low-frequency component $\Delta\omega$ and propagation velocity of $\Delta\omega / \Delta k$. Note that the low-frequency term has propagation velocity, which is group velocity $c_g = \frac{\Delta\omega}{\Delta k}$, in the limit becomes

$$c_g = \frac{d\omega}{dk} \tag{2.3-5}$$

The carrier velocity is c_p while the group velocity c_g is the velocity of the modulation. The propagating wave along the *x*-axis is represented in Figure 2.3. If we do only pay attention to the envelope motion instead of the detailed motion, we verify that the envelope moves forward with the group velocity c_g.

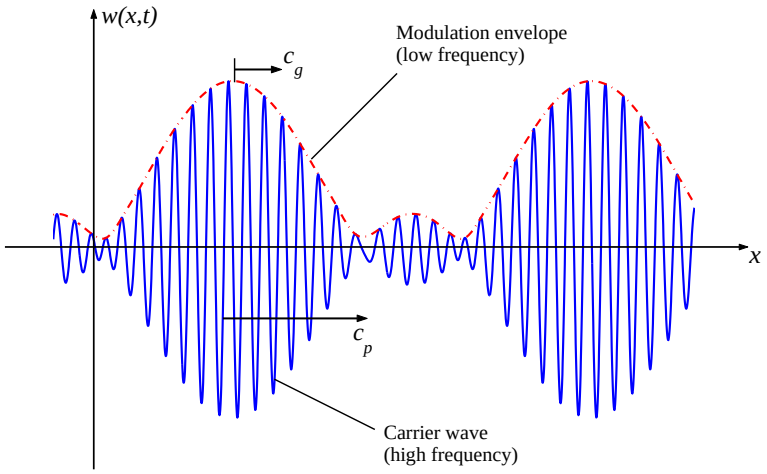

Figure 2.3 Illustration of group velocity

Additionally, observing more carefully at the detailed motion, we may see the waves moving within the envelope with their own velocity c_p.

It is worth of pointing out that the term of dispersive wave is attributed to the wave of which phase velocity is dependent upon ω, on the other hand the phase velocity changes with ω, and since different frequency components in wave travel at different speeds, the wave is distorted while traveling, however, a non-dispersive wave always keeps the same shape because all different frequency constants travel at the same velocity, for example longitudinal waves of a taut string.

2.3.2 Determination of phase velocity

In the previous Sections 2.1 and 2.2, determination of the dispersion relations of phase velocities has been discussed in detail, thus not repeated here.

2.3.3 Determination of group velocity

As far as isotropic materials are concerned, both group velocity and phase velocity has the same direction (wave propagation direction ϕ, which coincides with direction of

wave number vector **k**), and their magnitudes are independent of the wave propagation direction ϕ; numerical computation of group velocity may be simply obtained from the dispersion relation of phase velocity c_p.

Differentiating both sides of the definition of phase velocity $c_p = \omega/k$ with respect to ω, we have the expression

$$\frac{dc_p}{d\omega} = \frac{k - \omega \dfrac{dk}{d\omega}}{k^2} = \frac{1 - \dfrac{\omega}{k}\dfrac{dk}{d\omega}}{k} \tag{2.3-1}$$

Since group velocity in isotropic materials is defined as $c_g = d\omega/dk$ and consider $k = \omega/c_p$, One can rearrange Eq. (2.3-1) and immediately obtain the following relation to determine group velocity c_g from phase velocity c_p for isotropic materials

$$c_g = \frac{c_p}{1 - \dfrac{\omega}{c_p}\dfrac{dc_p}{d\omega}} \tag{2.3-2}$$

In anisotropic solids, the group velocity can be determined in the following procedures. Knowing $k_x = k\cos\phi$ and $k_y = k\sin\phi$, then the following relations can be obtained

$$k_x^2 + k_y^2 = k^2, \text{ and } \tan\phi = \frac{k_y}{k_x} \tag{2.3-3}$$

From Eq. (2.3-3), the following derivatives can be obtained

$$\frac{\partial k}{\partial k_x} = \frac{k_x}{k} = \cos\phi, \qquad \frac{\partial k}{\partial k_y} = \frac{k_y}{k} = \sin\phi \tag{2.3-4.a}$$

$$\frac{\partial \phi}{\partial k_x} = -\frac{k_y}{k_x^2}\cos^2\phi = -\frac{\sin\phi}{k}, \quad \frac{\partial \phi}{\partial k_y} = \frac{\cos^2\phi}{k_x} = \frac{\cos\phi}{k} \tag{2.3-4.b}$$

According to definition of group velocity and chain rule, we have

$$c_{gx} = \frac{\partial \omega}{\partial k_x} = \frac{\partial \omega}{\partial k}\frac{\partial k}{\partial k_x} + \frac{\partial \omega}{\partial \phi}\frac{\partial \phi}{\partial k_x} \tag{2.3-5.a}$$

$$c_{gy} = \frac{\partial \omega}{\partial k_y} = \frac{\partial \omega}{\partial k}\frac{\partial k}{\partial k_y} + \frac{\partial \omega}{\partial \phi}\frac{\partial \phi}{\partial k_y} \tag{2.3-5.b}$$

Substituting Eq. (2.3-4) into Eq. (2.3-5), the components of group velocity can be expressed as

$$c_{gx} = \frac{\partial \omega}{\partial k}\cos\phi - \frac{\partial \omega}{\partial \phi}\frac{\sin\phi}{k} \tag{2.3-6.a}$$

$$c_{gy} = \frac{\partial \omega}{\partial k}\sin\phi + \frac{\partial \omega}{\partial \phi}\frac{\cos\phi}{k} \tag{2.3-6.b}$$

or in matrix form

$$\begin{Bmatrix} c_{gx} \\ c_{gy} \end{Bmatrix} = \begin{bmatrix} \cos\phi & -\sin\phi \\ \sin\phi & \cos\phi \end{bmatrix} \begin{Bmatrix} \dfrac{\partial \omega}{\partial k} \\ \dfrac{\partial \omega}{k \partial \phi} \end{Bmatrix} \tag{2.3-7}$$

Therefore, the magnitude of group velocity c_g and skew angle φ are

$$c_g = \sqrt{c_{gx}^2 + c_{gy}^2}\text{, and } \varphi = \tan^{-1}\frac{c_{gy}}{c_{gx}} - \phi \tag{2.3-8}$$

Generally, for elastic waves in isotropic plates, the direction of group velocity coincides with the direction of wavenumber vector, so the skew angle φ is exactly zero. However, for elastic waves in anisotropic plates, the direction of group velocity does not coincide with the wavenumber vector in general, thus the skew angle may not be zero. At a given wavenumber direction ϕ, $\frac{\partial \omega}{\partial k}$ in Eq. (2.3-7) is easily calculated from the dispersion

relations of phase velocity. As for the derivative term $\frac{\partial \omega}{\partial \phi}$ in Eq. (2.3-7), a simple method is employed to approximate the value. The wavenumber direction is changed to $\phi + \Delta\phi$, where $\Delta\phi$ is a sufficiently small angle and compute the relation $\omega(k)$ from dispersion relations of phase velocity at the new angle. Thus, $\frac{\partial \omega}{\partial \phi}$ may be approximated as

$$\frac{\partial \omega}{\partial \phi} \approx \frac{\omega(k)\big|_{\phi+\Delta\phi} - \omega(k)\big|_{\phi}}{\Delta\phi} \tag{2.3-9}$$

Then, the dispersion relations of two components of group velocity can be numerically obtained by substituting $\frac{\partial \omega}{\partial k}$ and Eq. (2.3-9) into Eq. (2.3-7).

2.4 Numerical Examples

The methods described in the previous sections have been implemented for studying dispersive relations in composite laminates. The solutions from 3-D elasticity theory and the higher-order plate theory are calculated and then compared with each other. Numerical results of dispersion relations consist of elastic waves in a composite lamina (one-layered anisotropic plate) and a composite laminate (multi-layered plate). In each case we present phase and group velocity dispersion curves plotted as a function of the product of frequency and plate thickness.

The lamina material properties of IM7/5250-4 graphite/epoxy is listed in Table 2.1. Dimensionless frequency $\Omega = fh/c_L$ and dimensionless phase velocity c_p/c_L are used to normalize the physical wave frequency and phase velocity; additionally, c_L defined as $\sqrt{C'_{11}/\rho}$ is the longitudinal wave velocity in the direction of fiber orientation, where C'_{11} and

ρ are the elastic coefficient in the fiber direction and the density of a lamina. In isotropic materials, c_L is the longitudinal wave velocity. Note that all figures of dispersion curves in this section are shown in both dimensionless coordinate system (axes located at the bottom and left sides) and dimensional coordinate system (axes located at the top and right sides).

In the following, phase velocity distributions of elastic wave in both composite lamina and laminate are calculated from the higher-order plate theory and plotted in polar coordinate system at a fixed frequency. Then the dispersion behaviors of symmetric waves propagating along 45° in an IM7/5250-4 lamina are displayed with comparison between the two proposed theories followed by the results of antisymmetric waves. At last, the dispersion curves of phase and group velocity of a symmetric composite laminate are shown and are compared between the two theories. As expected, all the modes are dispersive.

Note that symmetric and antisymmetric waves are physically defined as the wave modes symmetric and antisymmetric with respect to the mid-plane of the plate. In a composite lamina where the direction of wave propagation is along the principal material directions, the extensional (symmetric) and flexural (antisymmetric) wave modes are decoupled from shear horizontal (symmetric and antisymmetric) modes. However in a composite lamina where the direction of propagation is along the off-axis and in a composite laminate, the extensional and flexural modes are coupled with the shear horizontal modes. In the following results, A_n indicates the coupled flexural and antisymmetric shear horizontal mode where flexural mode is dominant; S_n represents the coupled extensional and symmetric shear horizontal mode where extensional mode is dominant; SH_n $(n = 0, 2, \cdots)$ and $(n = 1, 3, \cdots)$ respectively represent symmetric and antisymmetric mode where shear horizontal mode is dominant;

In these figures, five symmetric modes can be obtained from the higher-order plate theory including three extensional wave modes (S_0, S_1, and S_2) and two symmetric SH wave modes (SH_0 and SH_2). Moreover, three antisymmetric modes exist in the higher-order plate theory containing two flexural wave modes (A_0 and A_1) and one antisymmetric SH wave mode (SH_1). In order to clearly compare the dispersion curves computed by the two theories, only the first five symmetric modes and three antisymmetric modes from 3-D elasticity theory are shown.

Figure 2.4 shows the phase velocity distributions of extensional wave modes (S_0, S_1, and S_2) and two symmetric SH wave modes (SH_0 and SH_2) in a lamina at dimensionless frequency $fh/c_L = 0.25$ (or 2.58 MHz·mm) based on higher-order plate theory. The phase velocity distributions of two flexural wave modes (A_0 and A_1) and one antisymmetric SH wave mode (SH_1) in a lamina are plotted in Figure 2.5 at dimensionless frequency $fh/c_L = 0.15$ (or 1.55 MHz·mm). From these figures, it can be seen that the magnitude of phase velocity depends on the propagation direction because of the inherent anisotropy of the composite lamina. When the propagation direction coincides with the fiber direction of the lamina (0º or 180º), phase velocity reaches its maximum value. However when wave propagation is perpendicular to the fiber direction (90º or 270º); phase velocity reaches its minimum value. In addition, from Figure 2.4 and 2.5, it can be observed that phase velocity distribution of each wave mode in the composite lamina has symmetry with respect to horizontal and vertical directions coinciding with the principal material directions of the lamina.

Figure 2.6 and 2.7 display the phase velocity distributions in a symmetric composite laminate. Because of stacking, the distributions are much more complicated than that of the

lamina. Furthermore, from Figure 2.6 and 2.7 it is may be seen that phase velocity distribution of each wave mode in the symmetric laminate has polar symmetric with respect to origin, that means every point on phase velocity distribution can overlap itself with 180º rotation.

In Figure 2.8, five symmetric modes in the higher-order plate theory and only the first five modes from infinite modes obtained from exact elasticity solutions are plotted. It can be seen that the first four modes and the beginning portion of SH_2 mode calculated by the higher-order plate theory have good agreement with those obtained from 3-D elasticity solutions. Figure 2.9 and 2.10 show the compared dispersion curves of group velocity and associated skew angles of symmetric modes, respectively. It can be seen that the higher-order plate theory solutions give good agreement with the 3-D elasticity solutions, especially for the frequency range below dimensionless frequency $fh/c_L = 0.15$ (or 1.55 MHz·mm).

It is noticed that in Figure 2.8 and 2.9 the beginning portions of SH_0 and S_0 mode are relatively flat in the low frequency range below dimensionless frequency $fh/c_L = 0.1$ (or 1.03 MHz·mm). thus the dispersive effect in this range is insignificant. This is a desired feature for a practical SHM using extensional wave as diagnostic signals. Although Lemistre and Balageas (2001) and Tan *et al.*(1995) suggested that the S_0 and S_1 modes of extensional waves is ideal for SHM since it has almost non-dispersive effect in the low frequency range, it was difficult to work with such mode in practice because this mode signal is very weak and attenuates quickly (Sohn *et al.*, 2004).

Three wave modes are obtained from the higher-order plate theory (see the three dotted lines in Figure 2.11). For comparison, only the first three modes from 3-D elasticity theory are plotted in Figure 2.11. It can be found that, for A_0 mode, both higher-order plate

theory and exact solutions match very well for all the frequencies plotted. For A_1 mode, the approximate solution matches the exact solution very well over the beginning portion when the dimensionless frequency fh/c_L is less than 0.15 (or 1.55 MHz·mm), and then it approaches the asymptote of exact solution of the SH_1 mode. Similar phenomenon on SH_1 mode can be observed. The approximate solution of SH_1 mode has a good agreement with 3-D elasticity solutions over the beginning portion of the SH_1 mode, which is less than dimensionless frequency $fh/c_L = 0.17$ (or 1.75 MHz·mm). Therefore, in the real SHM based on flexural waves, wave behavior in the portion of A_0 mode based on the higher-order theory, prior to the first cut-off frequency, can be conveniently modeled without the need of using more complicated 3-D elasticity solutions since the plate theory provide sufficient accuracy and real-time computation in this region without mode coupling.

Figures 2.12 and 2.13 display the computed group velocity dispersion curves and corresponding skew angles of antisymmetric waves, respectively. In Figure 2.12, as for A_0 mode, the approximate solution based on the higher-order plate theory matches the exact elasticity solution very well. However for A_1 mode, the beginning portion of the 3-D elasticity solution has a good agreement with higher-order plate theory until dimensionless frequency fh/c_L reaches 0.1 (or 1.03 MHz·mm), then it approaches the approximate solution of A_0 mode based on the higher-order plate theory after dimensionless frequency fh/c_L reaches 0.29 (or 3.08 MHz·mm). For SH_1 mode, the 3-D elasticity solution matches the higher-order solution very well within the range of dimensionless frequency $fh/c_L = 0.15$ (or 1.55 MHz·mm), then it branches off the approximate solution of SH_1 and drops sharply when dimensionless frequency fh/c_L is larger than 0.19 (or 2.0 MHz·mm), and then approaches the exact solution of A_0 mode. Due to the smeared properties through

the layers, the higher-order plate solution does not have the same the complicated behaviors as the exact solution, especially in the high frequency ranges; consequently, it can remarkably reduce the computational cost. Although the wave vector is along 45° and all of the phase velocities along this direction, the direction of group velocity can be different as shown in Figure 2.13. In this figure, it can still be seen that the skew angle based on the higher-order plate theory of A_0 mode gives a good agreement with the elasticity solution, and the skew angle of group velocity starts from 38º and then gradually drops to 15º. For the A_1 mode, the exact solution starts with the higher-order solution of the A_1 mode and approaches the higher-order solution of the A_0 mode. The exact solution of the SH_1 mode matches the higher-order plate solution from the beginning to dimensionless frequency $fh/c_L = 0.213$ (or 2.2MHz·mm) as an almost straight line around 45°, and then sharply decreases, however the higher-order plate theory remains straight line about 45°.

Finally, a set of Figures 2.14-19 shows the dispersion relations of elastic waves in an IM7/5250-4 symmetrically laminated composite with a stacking sequence $[90/60/90/-60/0]_s$. Similar trends as a single lamina are obtained with a slightly larger deviation between two theories.

Table2.1 Material properties of IM7/5250-4 lamina tape (fiber volume fraction V_f = 64%)

E_1 (GPa)	E_2 (GPa)	E_3 (GPa)	G_{12} (GPa)	G_{23} (GPa)	G_{13} (GPa)	ν_{12}	ν_{23}	ν_{13}	ρ ($\times 10^3$kg/m^3)
168	9.31	9.31	5.17	3.45	5.17	0.33	0.4	0.33	1.61

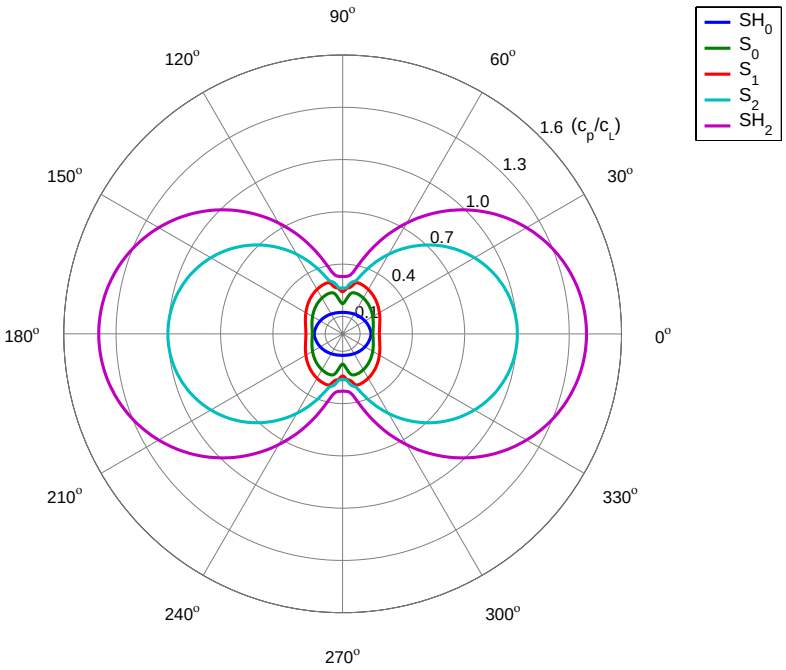

Figure 2.4 Phase velocity distribution of symmetric waves in IM7/5250-4 lamina with dimensionless frequency $fh/c_L = 0.25$

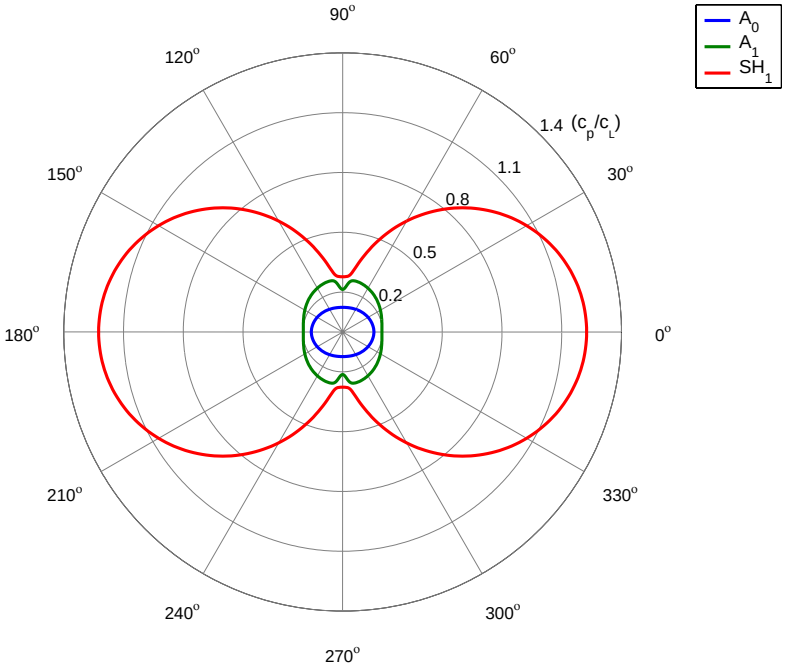

Figure 2.5 Phase velocity distribution of antisymmetric waves in IM7/5250-4 lamina with dimensionless frequency $fh/c_L = 0.15$

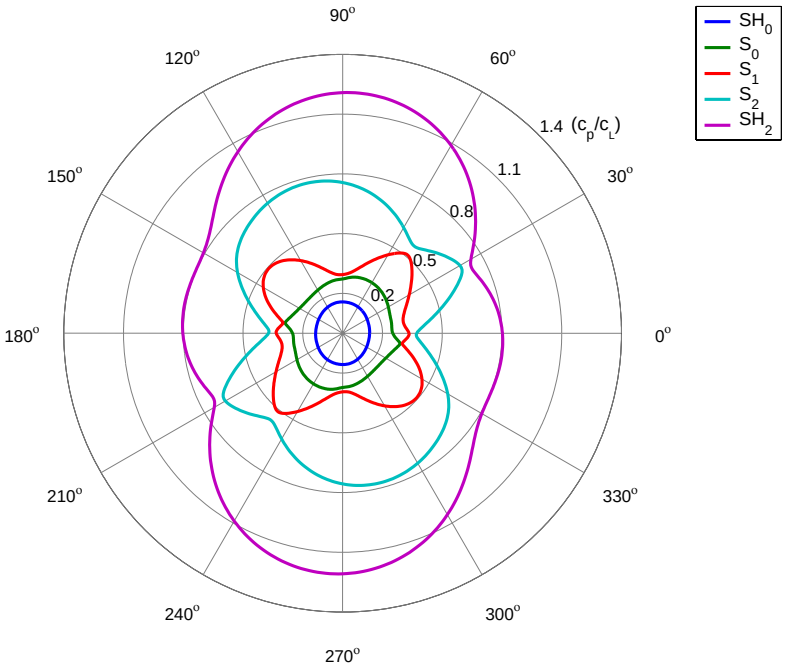

Figure 2.6 Phase velocity distribution of symmetric waves in $[90/60/90/-60/0]_s$ IM7/5250-4 laminate with dimensionless frequency $fh/c_L = 0.25$

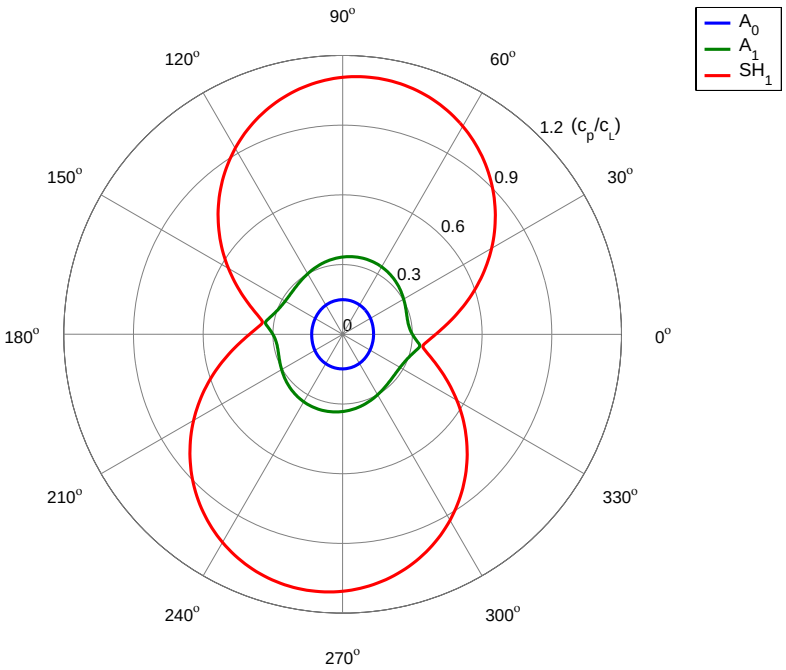

Figure 2.7 Phase velocity distribution of antisymmetric waves in $[90/60/90/-60/0]_s$ IM7/5250-4 laminate with dimensionless frequency $fh/c_L = 0.25$

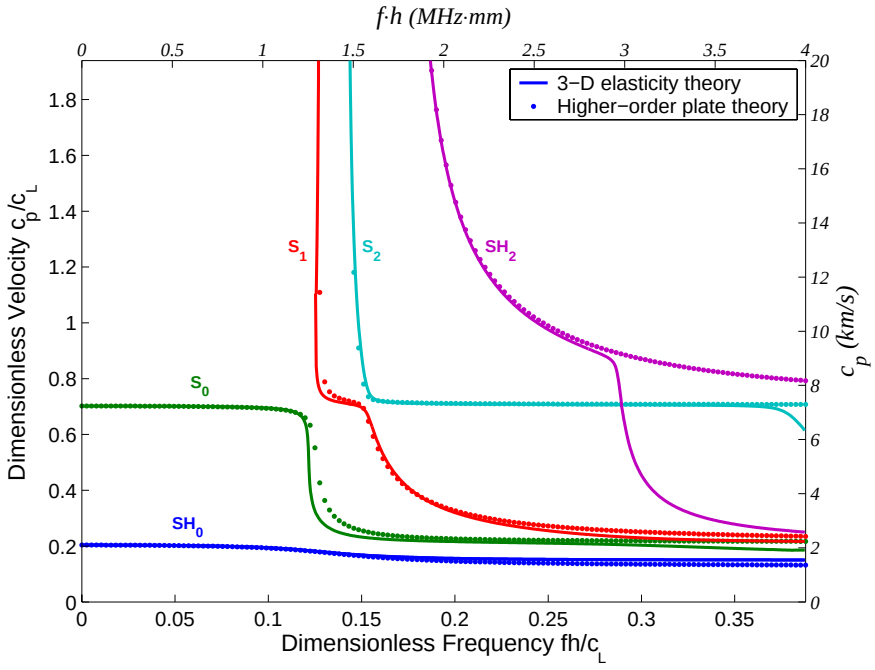

Figure 2.8 Comparison of phase velocity dispersions of symmetric waves from higher-order theory and 3-D elasticity theory with wave propagating along 45° in IM7/5250-4 lamina

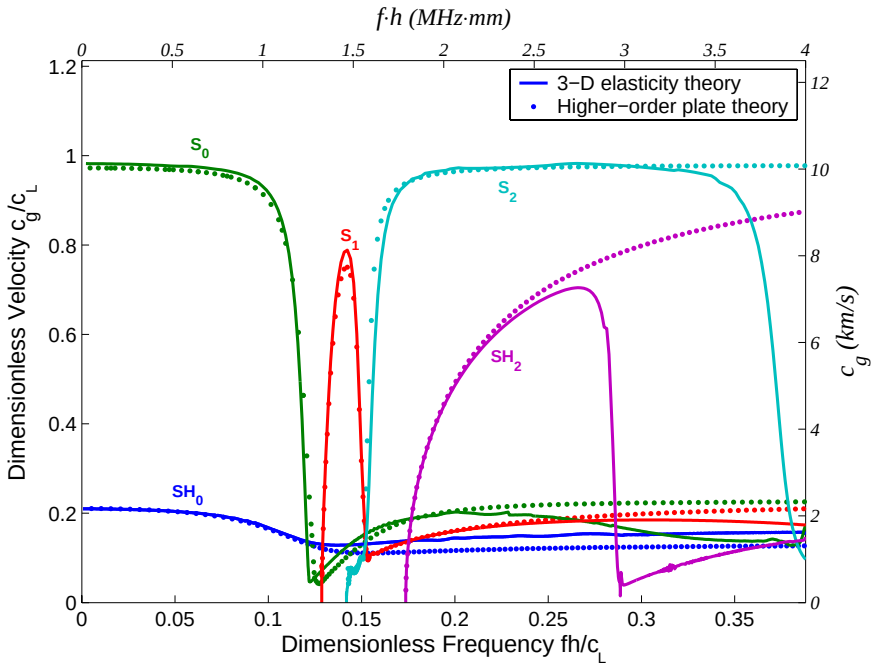

Figure 2.9 Comparison of group velocity dispersions of symmetric waves from higher-order plate theory and 3-D elasticity theory with wave propagating along 45° in IM7/5250-4 lamina

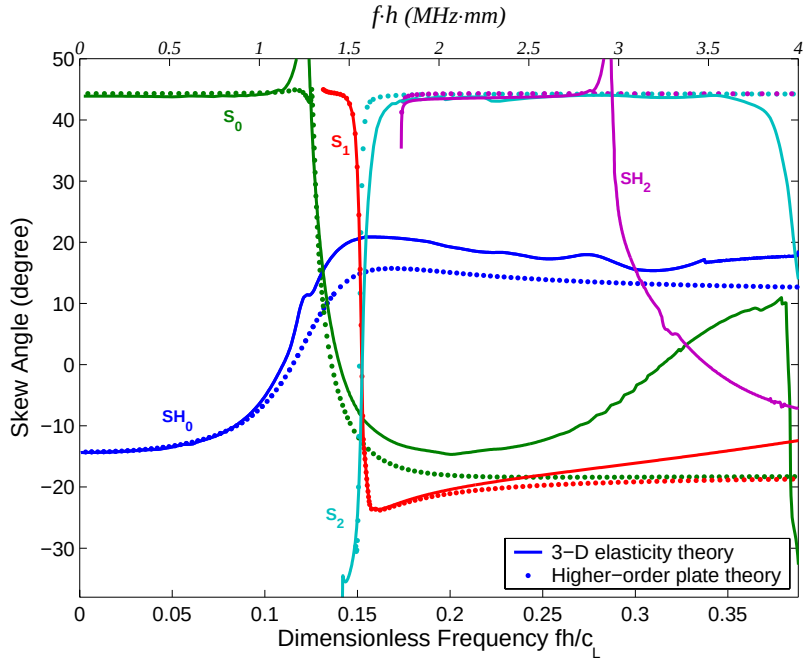

Figure 2.10 Comparison of skew angles of symmetric waves from higher-order plate theory and 3-D elasticity theory with wave propagating along 45° in IM7/5250-4 lamina

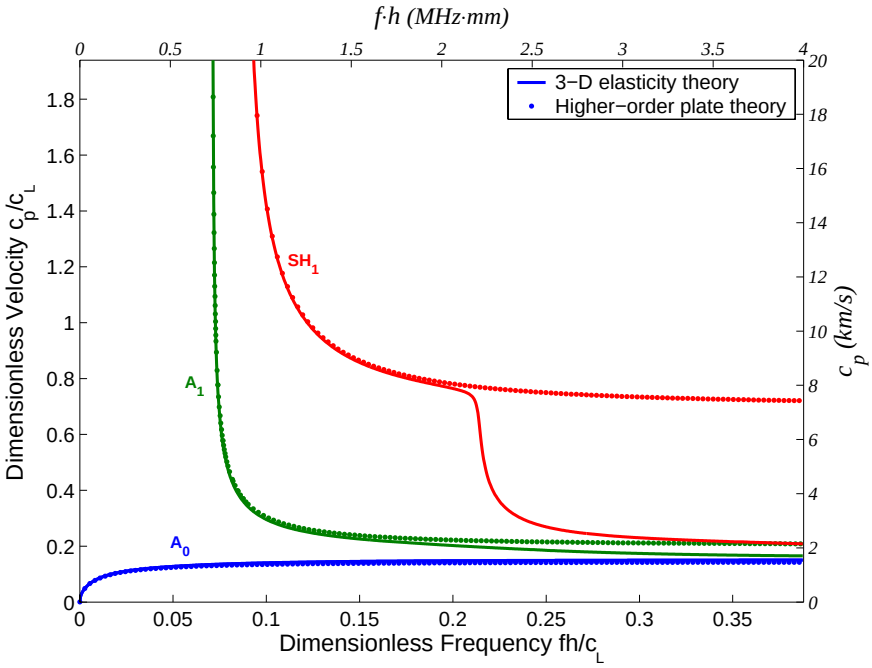

Figure 2.11 Comparison of phase velocity dispersions of antisymmetric waves from higher-order plate theory and 3-D elasticity theory with wave propagating along 45° in IM7/5250-4 lamina

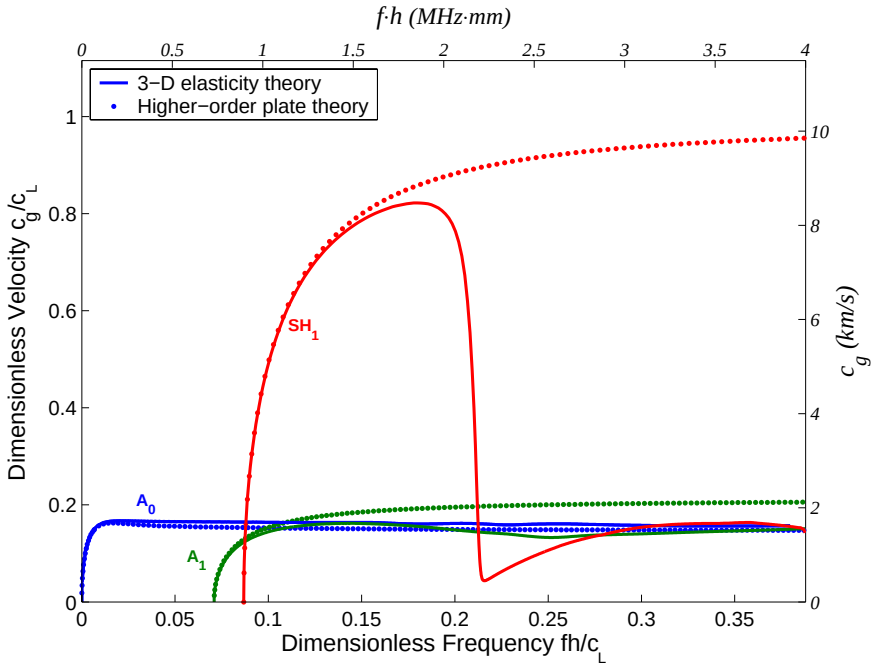

Figure 2.12 Comparison of group velocity dispersions of antisymmetric waves from higher-order plate theory and 3-D elasticity theory with wave propagating along 45° in IM7/5250-4 lamina

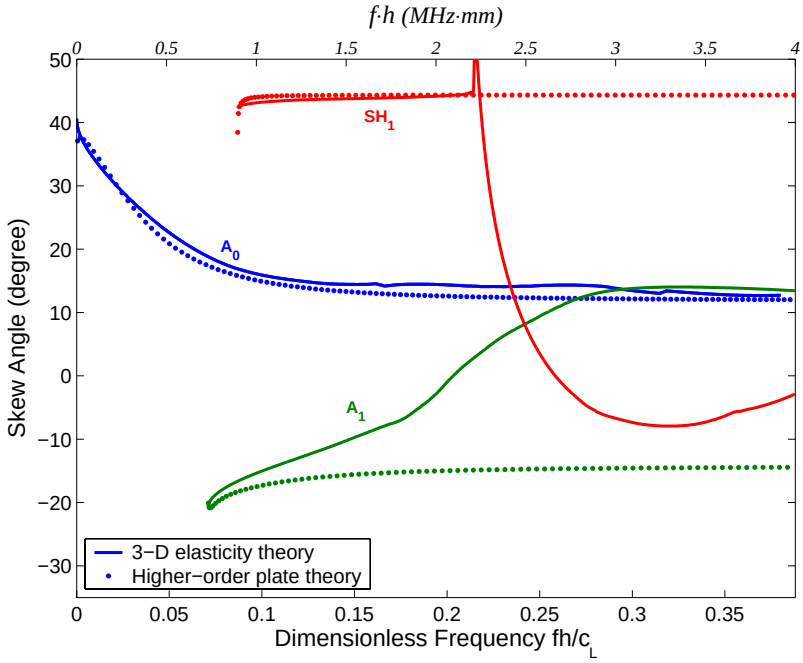

Figure 2.13 Comparison of skew angles of antisymmetric waves from higher-order plate theory and 3-D elasticity theory with wave propagating along 45° in IM7/5250-4 lamina

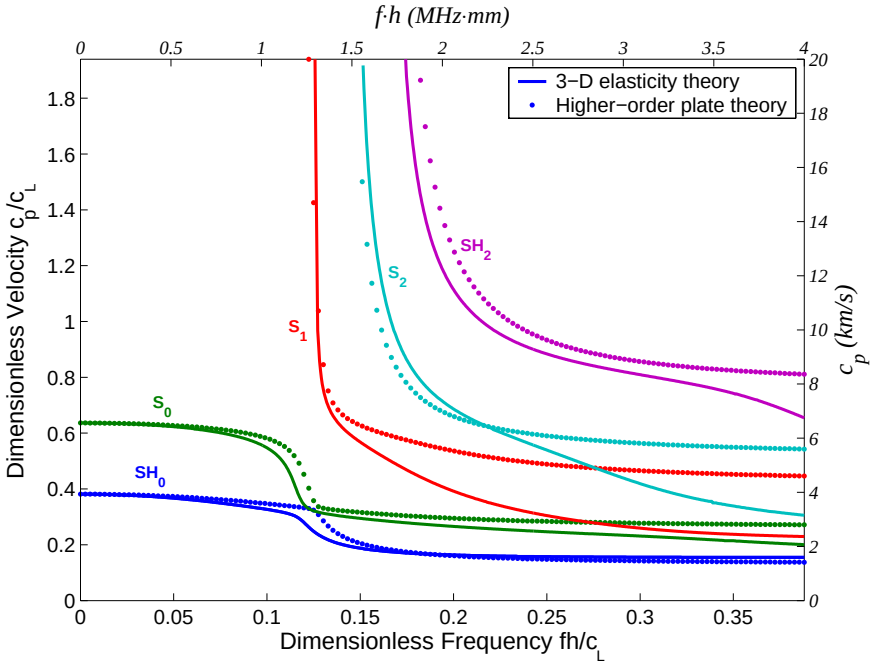

Figure 2.14 Comparison of phase velocity dispersions of symmetric waves from higher-order plate theory and 3-D elasticity theory with wave propagating along 45° in $[90/60/90/-60/0]_s$ IM7/5250-4 laminate

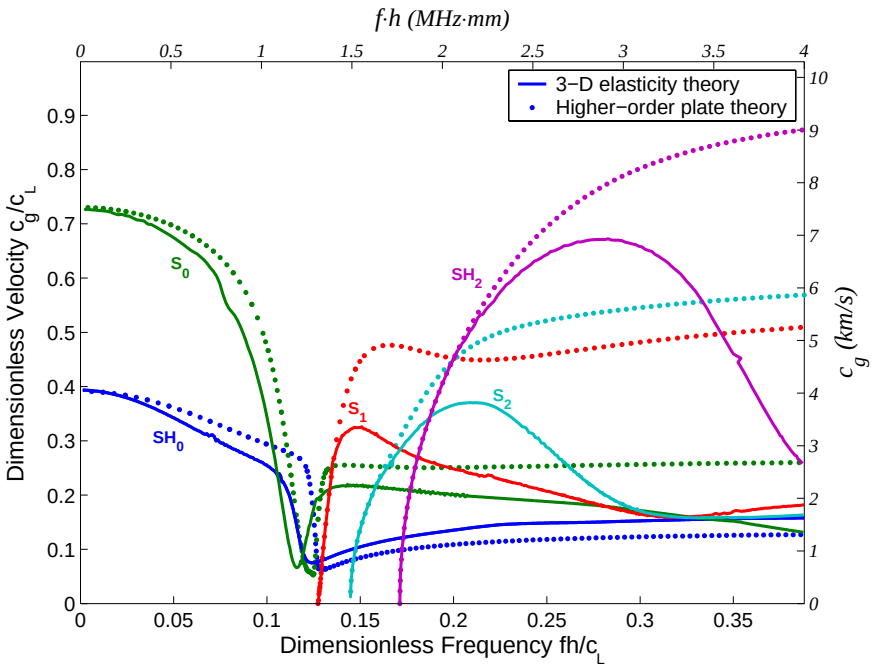

Figure 2.15 Comparison of group velocity dispersions of symmetric waves from higher-order plate theory and 3-D elasticity theory with wave propagating along 45° in $[90/60/90/-60/0]_s$ IM7/5250-4 laminate

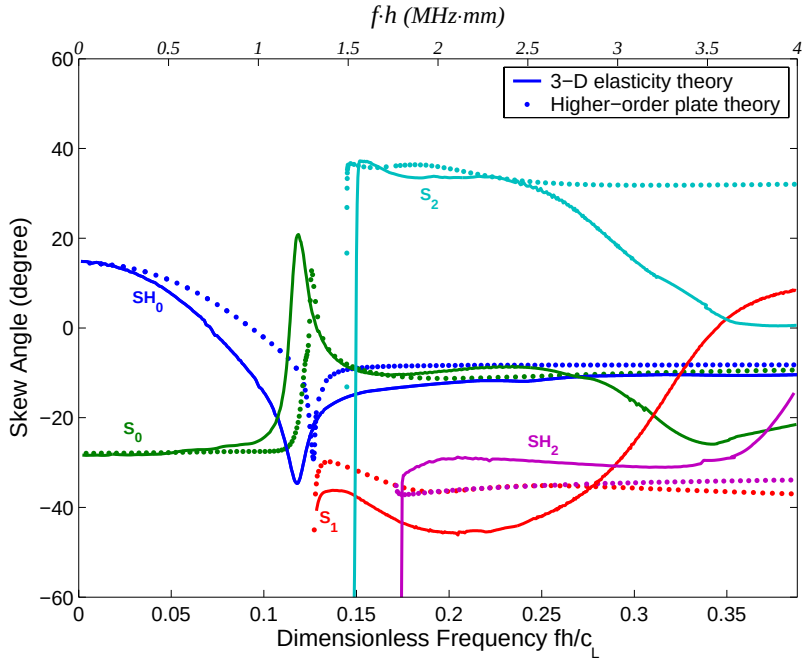

Figure 2.16 Comparison of skew angle of symmetric waves from higher-order plate theory and 3-D elasticity theory with wave propagating along 45° in $[90/60/90/-60/0]_s$ IM7/5250-4 laminate

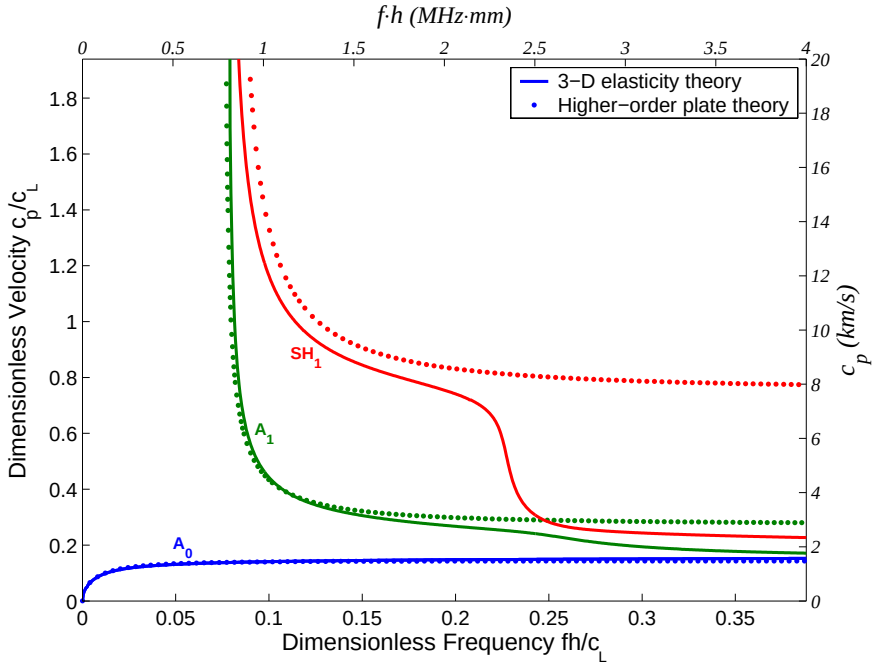

Figure 2.17 Comparison of phase velocity dispersions of antisymmetric waves from higher-order plate theory and 3-D elasticity theory with wave propagating along 45° in $[90/60/90/-60/0]_s$ IM7/5250-4 laminate

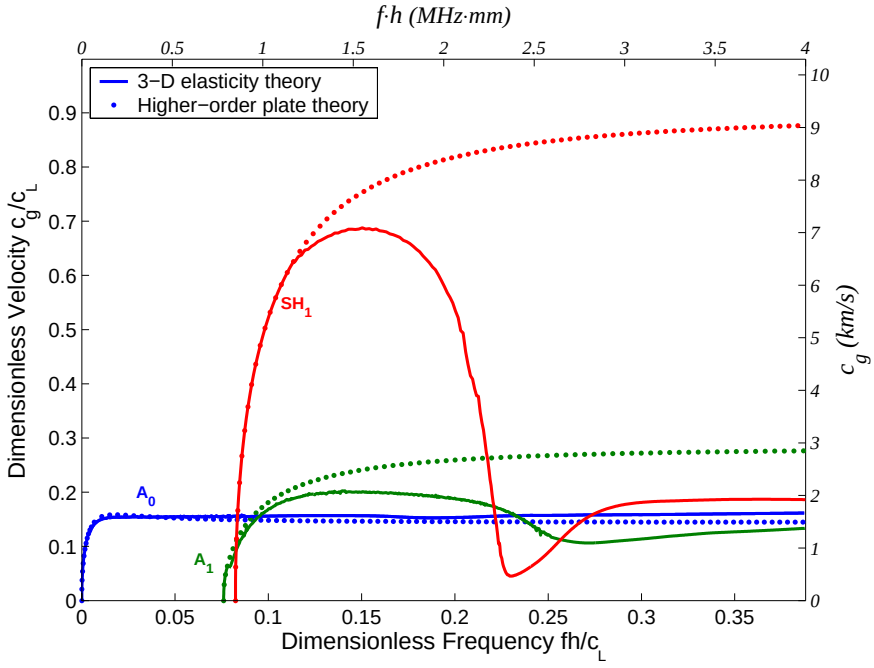

Figure 2.18 Comparison of group velocity dispersions of antisymmetric waves from higher-order plate theory and 3-D elasticity theory with wave propagating along 45° in $[90/60/90/-60/0]_s$ IM7/5250-4 laminate

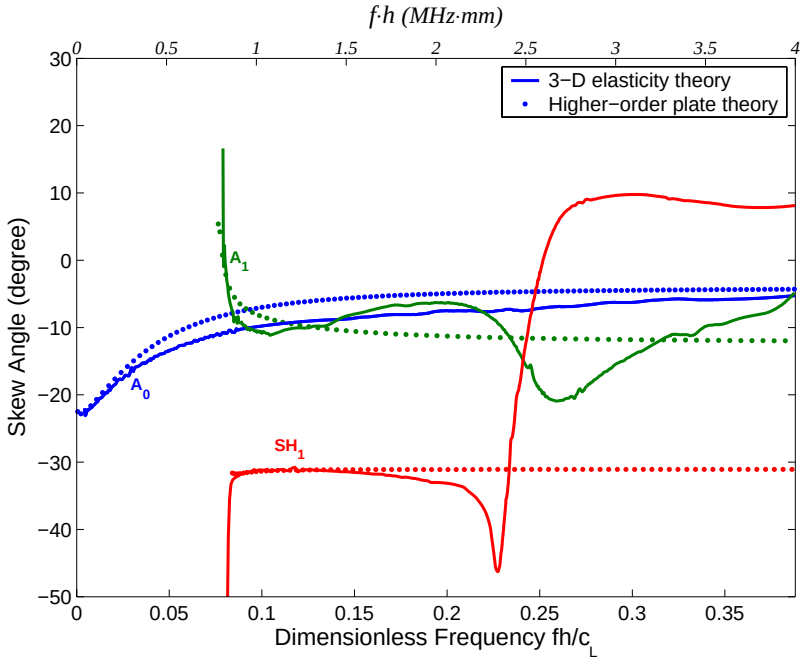

Figure 2.19 Comparison of skew angle of antisymmetric waves from higher-order plate theory and 3-D elasticity theory with wave propagating along 45° in $[90/60/90/-60/0]_s$ IM7/5250-4 laminate

3 Wavelet Analysis for Dispersive Waves in Plates

In this Chapter, Wavelet Transform (WT) is used to obtain the dispersion of phase and group velocities by analyzing elastic waves in a plate, and then dispersion curves of both phase and group velocities are verified from experiments in comparison with theoretical prediction. First, the fundamental of continuous wavelet transform (CWT) and the properties of Gabor function are introduced. Then practical implementation of WT in digital computer such as discretization of CWT, transforming a time-scale domain of WT to a physical time-frequency domain, and adding the Gabor function to Wavelet Toolbox in Matlab® are discussed in detail. Second, the Gabor WT is directly performed on a dispersive wave to extract the time-frequency information of the given waves. Consequently, the dispersion of group velocity and phase velocity can be mathematically obtained. Third, the theoretical dispersion relations are deduced from the Mindlin plate theory. Finally, experiments are performed by using a lead break as the simulated acoustic emission source signal on the surface of aluminum plate. The dispersion curves of both phase and group velocities obtained from the experiments by using WT show good agreement with theoretical prediction values.

3.1 Continuous Wavelet Transform

Wavelet analysis is fundamentally a correlation method. The wavelet coefficients provides information about a given signal $w_x(t)$, and its relationship to the shape of the analyzing wavelet, $\psi_{a,b}(t)$. The continuous WT of $w_x(t)$ is given by (Chui, 1992)

$$\mathrm{WT}_w(a,b) = \int_{-\infty}^{+\infty} w_x(t)\overline{\psi_{a,b}}dt \tag{3.1-1}$$

where $a > 0$ and over-bar indicates the complex conjugate. Moreover, the analyzing wavelet function has the form

$$\psi_{a,b}(t) = \frac{1}{\sqrt{a}}\psi(\frac{t-b}{a}) \tag{3.1-2}$$

where $\psi(t)$ is called mother (or base) wavelet function; a and b are known as the translation and scale parameters, respectively.

From Eq. (3.1-2), the base wavelet $\psi_{a,b}(t)$ can be considered as a function series generated by translating and scaling the mother wavelet function $\psi(t)$ using parameters *b* and *a*, respectively. In Fourier transform or short-time Fourier transform (STFT), the width of base function is constant either in the time domain or frequency domain. But the width of base function $\psi_{a,b}(t)$ in WT can be changed with scale a. This scaling is a primary feature of the wavelet transform. The factor $1/\sqrt{a}$ is used with the purpose of energy normalization ("energy" is defined as the square of Euclidean norm i.e. $\| \ \|_2^2$ of the given function) so that all the scaled wavelets have the same energy. In the time domain $\psi_{a,b}(t)$ can be represented as a function centered at *b* with a spread proportional to a. Furthermore, since the Fourier transform of $\psi_{a,b}(t)$ is $\sqrt{a}\hat{\psi}(a\omega)e^{-ib\omega}$, where $\hat{\psi}(\cdot)$ is the Fourier transform of $\psi(t)$, it may be seen that suppose the mother wavelet $\psi(t)$ has a central frequency ω_0 in the frequency domain, the central frequency of analyzing wavelet $\psi_{a,b}(t)$ is located at ω_0/a.

A mother wavelet function $\psi(t) \in \mathbf{L}^2$ (square integrable function) should satisfy several conditions. It should have a finite support in the time domain:

$$\lim_{t\to\infty}\psi(t) = 0 \tag{3.1-3}$$

and a zero-valued average over the entire time domain:

$$\int_{-\infty}^{+\infty}\psi(t)dt = 0 \tag{3.1-4}$$

In addition, it has to be normalized:

$$\|\psi(t)\|_2 = 1 \tag{3.1-5}$$

and is centered in the neighborhood of $t = 0$.

A WT is complete, which means $w(x,t)$ can be reconstructed from its WT coefficients, and maintains energy conservation as long as the mother wavelet function satisfies a so-called *admissible condition*, which guarantees the reconstruction of the signal $w(t)$ from its wavelet transform $\mathrm{WT}_w(a,b)$:

$$C_\psi = \int_{-\infty}^{+\infty} \frac{|\hat{\psi}(\omega)|^2}{\omega} d\omega < +\infty \tag{3.1-6}$$

The admissibility condition also implicates the Fourier $\hat{\psi}(\omega)$ of $\psi(t)$ to have a zero frequency component at the zero frequency, such that

$$\hat{\psi}(\omega)\big|_{\omega=0} = 0 \tag{3.1-7}$$

which physically means that the mother wavelet function does not have any DC (direct current) component and is consistent with the condition imposed by Eq. (3.1-4). Additionally, if Eq. (3.1-7) holds and $\psi(t)$ is continuously differentiable then the admissible condition Eq. (3.1-6) is satisfied (Mallat, 1998).

3.2 Gabor Wavelet Function

There are many continuous functions that satisfy Eq. (3.1-6) can be used as mother wavelet function in WT such as Morelet wavelet, Meyer wavelet, Mexican hat wavelet, and etc. Since the Gabor function can provide a better resolution both in the time and frequency domain than any other wavelets based on Heisenberg Uncertainty (Chui, 1992 and Mallat,

1998), it is very popular in the wavelet signal processing of SHM (Kishimoto *et al*., 1995; Suzuki *et al*., 1996; Jeong and Jang, 2000; and Quek *et al*., 2001).

The Gabor wavelet function and its Fourier transform are given by (Sato, 1991)

$$\psi_g(t) = \frac{1}{\sqrt[4]{\pi}}\sqrt{\frac{\omega_0}{\gamma}}\exp[-\frac{(\omega_0/\gamma)^2}{2}t^2]\exp(i\omega_0 t) \tag{3.2-1}$$

$$\hat{\psi}_g(\omega) = \frac{\sqrt{2\pi}}{\sqrt[4]{\pi}}\sqrt{\frac{\gamma}{\omega_0}}\exp[-\frac{(\gamma/\omega_0)^2}{2}(\omega-\omega_0)^2] \tag{3.2-2}$$

where γ is usually chosen as $\pi\sqrt{2/\ln 2} \approx 5.336$ such that the value of $\mathrm{Re}[\psi_g(t)]$ corresponding to the second peak of $\cos\omega_0 t$ (at $t = 2\pi/\omega_0$) is half the first one (at t = 0) (Vetterli and Kovacevic, 1995). The constant factor $\frac{1}{\sqrt[4]{\pi}}\sqrt{\frac{\omega_0}{\gamma}}$ of the Gabor function in Eq. (3.2-1) ensures the requirement given by Eq. (3.1-5). Figure 3.1 shows the Gabor function in the time and frequency domain. Note that $\psi_g(t)$ is complex in time domain; while $\hat{\psi}_g(\omega)$ is real in frequency domain.

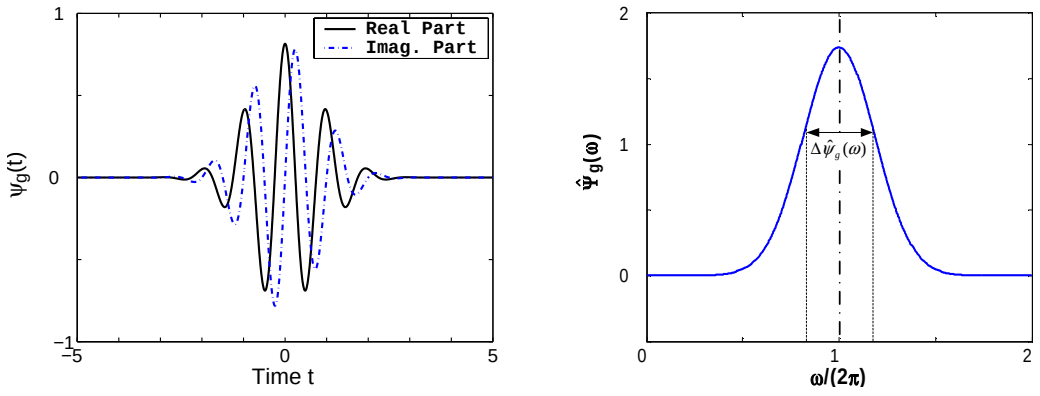

(a) (b)

Figure 3.1 (a) The Gabor function; (b) its Fourier transform for $\gamma = \pi\sqrt{2/\ln 2}$ and $\omega_0 = 2\pi$

The frequency bandwidth $\Delta\hat{\psi}_g(\omega)$ of Gabor function is $\frac{\sqrt[4]{\omega_0\pi}}{\sqrt[8]{8\ln 2}} \approx 1.075\times\sqrt[4]{\omega_0}$ marked in Figure 3.1(b) and detailedly deduced in Appendix A.4.

The Gabor function given in Eq. (3.2-1) may be physically considered as a modulated Gaussian window function centered at $t=0$, and its Fourier transform in Eq. (3.2-2) centered at $\omega=\omega_0$. Therefore the function $\psi_g(\frac{t-b}{a})$ is centered at $t=b$ and its Fourier transform given by $[a\exp(-ib\omega)\hat{\psi}_g(a\omega)]$ is centered at $\omega=\omega_0/a$. The $\mathrm{WT}_w(a,b)$ using the Gabor wavelet thus represents the time-frequency component of $w(x,t)$ around $t=b$ and $\omega=\omega_0/a$. In this study, ω_0 is conveniently set as 2π such that $1/a$ is exactly equal to the physical frequency f $(=\omega/2\pi)$.

However, the Gabor function does not strictly satisfy the admissibility condition Eq. (3.1-6), since $\hat{\psi}_g(\omega)\big|_{\omega=0} = \frac{1}{\sqrt[4]{\pi}}\sqrt{\frac{\omega_0}{\gamma}}e^{-\frac{\gamma^2}{2}} \neq 0$. However, when γ is sufficiently large, say $\gamma > 5$, $\hat{\psi}_g(\omega)\big|_{\omega=0}$ is very close to zero.

Furthermore, γ is usually chosen such that the value of $\mathrm{Re}[\psi_g(t)]$ corresponding to the second peak of $\cos\omega_0 t$ (at $t=2\pi/\omega_0$)is half the first one (at t = 0) (Vetterli and Kovacevic, 1995). That is

$$\mathrm{Re}[\psi_g(t)]\big|_{t=0} = 2\,\mathrm{Re}[\psi_g(t)]\big|_{t=2\pi/\omega_0} \tag{3.2-3}$$

This leads to

$$\frac{1}{\sqrt[4]{\pi}}\sqrt{\frac{\omega_0}{\gamma}} = 2\frac{1}{\sqrt[4]{\pi}}\sqrt{\frac{\omega_0}{\gamma}}\exp(-\frac{(\omega_0/\gamma)^2}{2}\frac{4\pi^2}{{\omega_0}^2}) \tag{3.2-4}$$

Simplifying the form above, we can obtain $\ln 2 = 2\pi^2/\gamma^2$. Thus $\gamma \equiv \pi\sqrt{2/\ln 2} \approx 5.336$.

Lastly, if $\gamma = \pi\sqrt{2/\ln 2}$ and $\omega_0 = 2\pi$, $\hat{\psi}_g(\omega)\big|_{\omega=0} = \frac{1}{\sqrt[4]{\pi}}\sqrt{\frac{\omega_0}{\gamma}}e^{-\frac{\gamma^2}{2}} = 9.313\times10^{-7}$.

Clearly its value at zero frequency is negligible. Therefore it is does not present any problem in practice (Vetterli and Kovacevic, 1995).

Thus the Gabor function approximately satisfies the admissibility condition when $\gamma > 5$. But if γ is very large, it will enlarge the time window of the Gabor function. Figure 3.2 (a) and (b) show the different Gabor functions in terms of different values of γ.

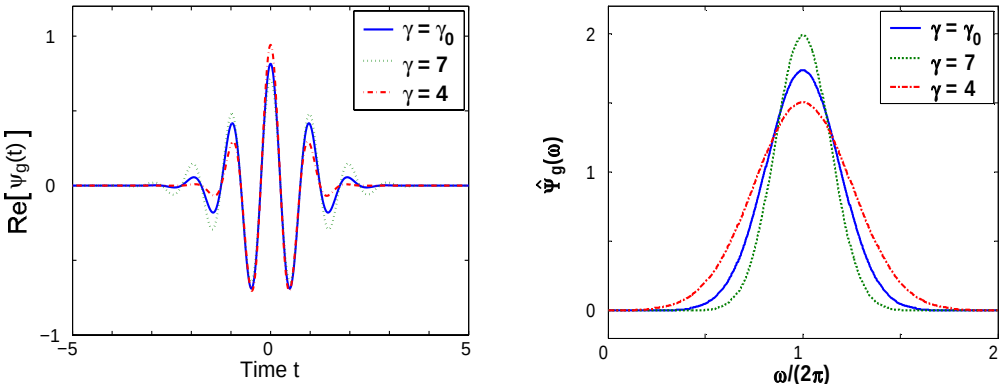

(a) (b)

Figure 3.2 (a) The real parts of different Gabor functions when $\gamma = 4, 5.356, 7$;
(b) associated Fourier transforms

Lastly, by Parseval identity (Chui, 1992 and Mallat, 1998),

$$\int_{-\infty}^{+\infty} f(t)\overline{g(t)}\,dt = \frac{1}{2\pi}\int_{-\infty}^{+\infty} \hat{f}(\omega)\overline{\hat{g}(\omega)}\,d\omega \tag{3.2-5}$$

Eq. (3.1-1) in the time domain can be transformed into the frequency domain as

$$\mathrm{WT}_w(a,b) = \frac{\sqrt{a}}{2\pi}\int_{-\infty}^{+\infty} \hat{w}(x,\omega)\hat{\psi}_g(a\omega)\exp(ib\omega)\,d\omega \tag{3.2-6}$$

This expression will be used in the following Section 3.4 to determine phase and group velocities.

3.3 Implementation of Gabor Wavelet Transform

3.3.1 Discretization of CWT

Since the computation of wavelet coefficients has to be performed in a digital computer, the CWT needs to be calculated numerically, requiring discretization of the function and its transform. It should be noted that, even though CWT is calculated in a discrete manner, it is still called a CWT. The reason is that this discretization transform is calculated for every single scale value and still holds the time-invariance shifting property of CWT, see Eq. (3.3-1); on the other hand, there is a special form of discretizing scale and translation domain and takes the name of Discrete Wavelet Transform (DWT). It should be noted that DWT does not hold the time-invariance shifting property.

The discretization of CWT is made by directly discretizing Eq. (3.1-1)

$$a_n = n\Delta a\,,\ n = 1, 2, 3, \cdots, M \tag{3.3-1a}$$

$$b_k = k\Delta t\,,\ k = 0, 1, 2, \cdots, N-1 \tag{3.3-1b}$$

$$t_m = m\Delta t\,,\ m = 0, 1, 2, \cdots, N-1 \tag{3.3-1c}$$

where M is the number of scale values desired, N is the number of discrete points in the function, Δa is the scale step, and Δt is the sampling interval.

Substituting into Eq. (3.1-1), the discrete version of the CWT may be expressed as

$$\mathrm{WT}_w(k,n) = \frac{1}{\sqrt{n\Delta a}} \sum_{m=0}^{N-1} w(m\Delta t)\overline{\psi(\frac{(m-k)\Delta t}{n\Delta a})}\Delta t \tag{3.3-2}$$

3.3.2 Time-scale to physical time-frequency

It has been shown one-dimensional signal $w(t)$ can be transformed into two-dimensional a-b domain named time-scale plane after performing CWT. Moreover, the reciprocal of scale parameter a is related to frequency and the translation parameter b is

associated with time. In order to obtain the physical frequency and time information from the coefficients of CWT, the quantitative relations from time-scale (*a*-*b* domain) to time-frequency (*t*-*f* domain) has to be established.

The CWT has the time-invariance shifting property:

$$\mathrm{WT}_{w(t-\tau)}(a,b) = \mathrm{WT}_{w(t)}(a,b-\tau) \tag{3.3-3}$$

which means that if the original signal delays τ, the CWT coefficients of $w(t)$ will also have the same delay τ shown in the b axis. Therefore, the b axis of CWT is exactly equivalent to t axis of original signal $w(t)$, and also shares the same units as each other. No operation on b axis is needed after CWT.

It has been mentioned in Section 3.2 that the function $\psi_g(\frac{t-b}{a})$ is then centered at $t=b$, its Fourier transform yields $[a\exp(-ib\omega)\hat{\psi}_g(a\omega)]$ is centered at $\omega = \omega_0/a$. Hence, the scale to the frequency relation is related by:

$$f = \frac{\omega}{2\pi} = \frac{\omega_0}{2\pi a} \tag{3.3-4}$$

For the Gabor wavelet used in this study, we have $\omega_0 = 2\pi$, then Eq. (3.3-4) yield

$$f = \frac{1}{a} \tag{3.3-5}$$

Since scale a is a non-dimensional factor, f is also non-dimensional frequency. To obtain the dimensional frequency $\hat{f}$, the following relation needs to be used in the practical signal processing

$$\hat{f} = f \cdot f_s = \frac{f_s}{a} \tag{3.3-6}$$

where f_s is the sampling rate of $w(t)$. $\hat{f}$ has frequency unit in Hz. Thus, after CWT, a axis needs a reciprocal operation and multiplies the sampling rate f_s.

3.3.3 Add Gabor function to wavelet toolbox of Matlab®

The Wavelet Toolbox of Matlab® is chosen as a computing platform to implement wavelet analysis of dispersive wave signals, because this toolbox contains a very comprehensive collection of wavelet-related functions together with powerful computation and convenient data visualization of Matlab®. However, the Gabor wavelet is not available in Wavelet Toolbox. In this case, the Gabor wavelet function needs to be added into Wavelet Toolbox before running a Matlab® command cwt for continuous wavelet transform. The following steps illustrate how to add a new function into Wavelet Toolbox:

1. Write an M-script file `gabor.m` based on Eq. (3.2-1) and save it to both "\MATLAB6p5\toolbox\wavelet\wavelet\" and current work directory. It is optional to write another M-script file `gabinfo.m`, which contains the mathematic features of the Gabor wavelet and allows Wavelet Toolbox GUI (`wavemenu`) to access this information, and save it as the same location of `gabor.m`. (See Appendix A.3)
2. Run the following command in command window to add the new mother function. `wavemngr('add','Gabor','gab',5,'','gabor',[-4,4])`. If "Gabor gab" is listed by running command `wavemngr('read')`, the Gabor wavelet function is successfully added. The Wavelet Toolbox User's Guide (Misiti *et al.*, 2002) provides more details and the procedures.

3.4 Time-frequency Analysis of Dispersive Waves

3.4.1 Time-frequency analysis by wavelet transform

For a harmonic wave propagating along the *x*-axis direction in a thin plate, the transverse displacement can be expressed as

$$w(x,t) = A\exp[i(\omega t - kx)] \tag{3.4-1}$$

where A is the complex-valued amplitude, ω is the angular frequency and k is the wave number.

The dispersive waves in structures are characterized by phase velocity c_p, and group velocity c_g as

$$c_p = \frac{\omega}{k},\ c_g = \frac{d\omega}{dk} \tag{3.4-2}$$

For a plate governed by linear equations, according to the principle of superposition, $w(x,t)$ propagating in the linear medium $x \geq 0$ may be expressed as a superposition of all plane harmonic waves.

$$w(x,t) = \int_{-\infty}^{+\infty} A(\omega)\exp[i(\omega t - kx)]\,d\omega \tag{3.4-3}$$

Assuming that the medium is at rest initially $w(x,0) = \dot{w}(x,0) = 0$ and an excitation signal or load $F(t)$ is generated at the location $x = 0$, for $t \geq 0$, that is,

$$w(0,t) = F(t) \tag{3.4-4}$$

Then, from Eq. (3.4-3), it follows that

$$F(t) = \int_{-\infty}^{+\infty} A(\omega)\exp(i\omega t)\,d\omega \tag{3.4-5}$$

Mathematically Eq. (3.4-5) implies that $F(t)$ is the inverse Fourier transform of the function $A(\omega)$. Therefore $A(\omega)$ can be recovered by

$$A(\omega) = \frac{1}{2\pi}\int_{-\infty}^{+\infty} F(\xi)\exp(-i\omega\xi)\,d\xi \tag{3.4-6}$$

With Eq. (3.4-6), Eq. (3.4-3) may be rewritten as

$$\begin{aligned} w(x,t) &= \frac{1}{2\pi}\int_{-\infty}^{+\infty} d\omega \int_{-\infty}^{+\infty} F(\xi)\exp[i(\omega t - kx - \omega\xi)]\,d\xi \\ &= \frac{1}{2\pi}\int_{-\infty}^{+\infty}\left(\int_{-\infty}^{+\infty} F(\xi)\exp(-ikx)\cdot\exp(-i\omega\xi)\,d\xi\right)\exp(i\omega t)d\omega \end{aligned} \tag{3.4-7}$$

According to the definition of Fourier transform of $w(x,t)$, $\hat{w}(x,\omega)$ may be obtained from Eq. (3.4-7),

$$\begin{aligned} \hat{w}(x,\omega) &= \int_{-\infty}^{+\infty} F(\xi)\exp(-ikx)\cdot\exp(-i\omega\xi)\,d\xi \\ &= \hat{F}(\omega)\exp(-ikx) \end{aligned} \tag{3.4-8}$$

where complex $\hat{F}(\omega)$ is the Fourier transform of $F(t)$ (Sachse and Pao, 1978).

Substituting Eq. (3.4-8) into Eq. (3.2-6) gives the WT in frequency domain

$$\mathrm{WT}_w(a,b) = \frac{\sqrt{a}}{2\pi}\int_{-\infty}^{+\infty}\hat{F}(\omega)\exp(-ikx)\hat{\psi}_g(a\omega)\exp(ib\omega)d\omega \tag{3.4-9}$$

In order to observe both amplitude and phase angle information of $\mathrm{WT}_w(a,b)$, it is useful to get an approximate soluiton and to provide physical insight of $\mathrm{WT}_w(a,b)$, instead of directly evaluating integral form above. Using a first-order Taylor expansion and performing some algebraic deductions, Eq. (3.4-9) leads to (see Appendix A.5 for detail)

$$\begin{aligned} \mathrm{WT}_w(a,b) = {} & \frac{\hat{F}(\omega_c) - \omega_c\hat{F}'(\omega_c)}{2\sqrt{a}\pi}\exp[(i(k'x\omega_c - kx)]\,\psi_g\left(\frac{b-k'x}{a}\right) \\ & + \frac{\sqrt{a}\hat{F}'(\omega_c)}{2a^2\pi}\exp[i(k'x\omega_c - kx - \pi/2)]\,\psi'_g\left(\frac{b-k'x}{a}\right) \end{aligned} \tag{3.4-10}$$

where $\omega_c = \omega_0 / a$ and $k' = dk(\omega_c)/d\omega$.

3.4.2 Determination of group and phase velocities

In Eq. (3.4-10), both $\hat{F}(\omega_c)$ and $\hat{F}'(\omega_c)$ have only one independent variable ω_c, furthermore ω_c is merely a function of a. Accordingly, $\hat{F}(\omega_c)$ and $\hat{F}'(\omega_c)$ are functions of a. In the following proof, $\Phi_w(a,b)$ and $\left|\mathrm{WT}_w(a,b)\right|$ are defined as the phase angle and magnitude of wavelet transform $\mathrm{WT}_w(a,b)$ respectively.

(1) Determination of group velocity c_g

If the derivative of $\left|\mathrm{WT}_w(a,b)\right|$ with respect to b in Eq. (3.4-10) equals to zero, i.e., $\dfrac{\partial\left|\mathrm{WT}_w(a,b)\right|}{\partial b} = 0$, we have

$$b - k'x = 0 \tag{3.4-11}$$

It means $$c_g = \frac{d\omega}{dk} = \frac{1}{k'} = \frac{x}{b} \tag{3.4-12}$$

The result indicates that the magnitude of the WT takes its maximum value at $\omega_c = \omega_0 / a$ and $b = \dfrac{dk}{d\omega}x = \dfrac{x}{c_g}$. In other words, the peak location on the magnitude plane $\left|\mathrm{WT}_w(a,b)\right|$ indicates the arrival time of the group velocity c_g at each local frequency $\omega_c = \omega_0 / a$. Here b can be called arrival time.

If the distance x between actuator and sensor is known and the arrival time b from the magnitude plane $\left|\mathrm{WT}_w(a,b)\right|$ at a fixed scale a can be observed, the group velocity is obtained as $c_g = \dfrac{x}{b}$ for this scale. Furthermore, with the change of scale a, the corresponding group velocities can be calculated, and then the group velocity dispersion can be obtained.

Note that Kishimoto *et al.* (1995) and Jeong (2001) obtained the same result by using the wavelet analysis of a combination of two different harmonic waves with slightly different frequencies.

(2) Determination of phase velocity c_p

The peak location on the magnitude plane $|\mathrm{WT}_w(a,b)|$ indicates $b-k'x=0$, where b is the arrival time; in this case, the magnitude of $\psi_g(\frac{b-k'x}{a})$ arrives at its maximum value and thus $\psi'_g(\frac{b-k'x}{a})$ is equal to zero. Therefore, there is only one term left in Eq. (3.4-10), that is,

$$\mathrm{WT}_w(a,b)=\frac{\hat{F}(\omega_c)-\omega_c\hat{F}'(\omega_c)}{2\sqrt{a}\pi}\exp[(i(k'x\omega_c-kx)]\psi_g(\frac{b-k'x}{a}) \tag{3.4-13}$$

Substituting the expression of $\psi_g(\frac{b-k'x}{a})$ with $\omega_c=\omega_0/a$ into Eq. (3.4-13) gives

$$\mathrm{WT}_w(a,b)=\frac{\hat{F}(\omega_c)-\omega_c\hat{F}'(\omega_c)}{2\sqrt{a}\sqrt[4]{\pi}\pi}\sqrt{\frac{\omega_0}{\gamma}}\exp[-\frac{(\omega_0/\gamma)^2}{2}(\frac{b-k'x}{a})^2]\exp(i\omega_0\frac{b-k'x}{a})\exp[i(k'x\omega_c-kx)] \tag{3.4-14}$$

It can be further simplified as

$$\mathrm{WT}_w(a,b)=\frac{\hat{F}(\omega_c)-\omega_c\hat{F}'(\omega_c)}{2\sqrt{a}\sqrt[4]{\pi}\pi}\sqrt{\frac{\omega_0}{\gamma}}\exp[-\frac{\omega_c^2}{2\gamma^2}(b-k'x)^2]\exp[i(\omega_c b-kx)] \tag{3.4-15}$$

Therefore, the phase angle of $\mathrm{WT}_w(a,b)$ is $\omega_c b-kx$. This means at the arrival time b

$$\Phi_w(a,b)=\omega_c b-kx,\quad \frac{\partial\Phi_w}{\partial b}=\omega_c \tag{3.4-16}$$

Suppose, for a fixed scale a, the phase of wavelet coefficients $\Phi_w(a,b)$ has the value θ which is related to the peak location on the magnitude plane $|\mathrm{WT}_w(a,b)|$. That is,

$$\omega_c b-kx=\theta \tag{3.4-17}$$

Solving the equation above, we can get the phase velocity c_p at scale a can be obtained as

$$c_p = \frac{\omega_c}{k} = \frac{x}{b - \frac{\theta}{\omega_c}} \tag{3.4-18}$$

where $\omega_c = \omega_0 / a$.

If the arrival time b can be found by locating the peak point from the magnitude plane $\left|\mathrm{WT}_w(a,b)\right|$ for a fixed scale a, then the corresponding phase angle from the phase plane $\Phi_w(a,b)$ can be obtained. Knowing the distance x between actuator and sensor, the phase velocity c_p can be calculated by using the Eq. (3.4-18). With the change of scale a, the corresponding phase velocities can be calculated; furthermore the phase velocity dispersion can also be obtained.

3.5 Theory on Dispersion of Flexural Waves

A theoretical approach is used for predicting the behavior of plate mode waves in isotropic plates. For prediction of dispersion of the flexural mode, Mindlin plate theory (Mindlin, 1951) is employed. This theory includes the effects of shear deformation and rotory inertia.

Consider an isotropic plate with Young's modulus E, shear modulus G, density ρ, and thickness h. Based on Mindlin plate theory, the equation of motion can be described as (Graff, 1991)

$$(\nabla^2 - \frac{\rho}{\kappa G}\frac{\partial^2}{\partial t^2})(D\nabla^2 - \frac{\rho h^3}{12}\frac{\partial^2}{\partial t^2})w + \rho h \frac{\partial^2 w}{\partial t^2} = 0 \tag{3.5-1}$$

From the above equation, one has the dispersion relation

$$\frac{(\omega\sqrt{\rho h^5/D})^4}{72\kappa(1-\nu)}-\left\{1+[\frac{1}{12}+\frac{1}{6\kappa(1-\nu)}](kh)^2\right\}(\omega\sqrt{\rho h^5/D})^2+(kh)^4=0 \tag{3.5-2}$$

where ω is the angular frequency of the propagating wave, plate bending stiffness $D=\frac{Eh^3}{12(1-\nu^2)}$ and shear correction factor $\kappa=\pi^2/12$.

Eq. (3.5-2) can be considered as a fourth-order polynomial equation with respect to variable k. Defining the nondimensional variables $\tilde{\omega}=\omega T$, $\tilde{k}=kh$, where $T=\sqrt{\rho h^5/12D}$ and $\alpha=\kappa(1-\nu)/2$, (Note that the superscript "~" in the context is defined as the nondimensional of the known variable) Eq. (3.5-2) can be simplified as

$$\alpha\tilde{k}^4-[(1+\alpha)\tilde{k}^2+12\alpha]\tilde{\omega}^2+\tilde{\omega}^4=0 \tag{3.5-3}$$

The nondimensional dispersion relation is only a function of α.

Eq. (3.5-3) has four analytical solutions of $\tilde{k}$; but physically, the wavenumer k is supposed to be a positive real value. The two positive real solutions of $\tilde{k}$ are written as follows and the other two negative real solutions are neglected.

$$\tilde{k}_1=\sqrt{\frac{\tilde{\omega}}{2\alpha}[(1+\alpha)\tilde{\omega}+\sqrt{48\alpha^2+(1-\alpha)^2\tilde{\omega}^2}]} \tag{3.5-4}$$

$$\tilde{k}_2=\sqrt{\frac{\tilde{\omega}}{2\alpha}[(1+\alpha)\tilde{\omega}-\sqrt{48\alpha^2+(1-\alpha)^2\tilde{\omega}^2}]} \tag{3.5-5}$$

To guarantee the real value of $\tilde{k}_2$, the following relation of the first cut-off frequency can be deduced from Eq. (3.5-5)

$$(1+\alpha)\tilde{\omega}-\sqrt{48\alpha^2+(1-\alpha)^2\tilde{\omega}^2}\geq 0 \tag{3.5-6}$$

Solving the inequality equation above, the nondimensional first cut-off frequency is

$$\tilde{\omega}_{cut-off} = 2\sqrt{3\alpha} \tag{3.5-7}$$

and its corresponding dimensional first cut-off frequency is

$$\omega_{cut-off} = \tilde{\omega}_{cut-off} / T = 6\sqrt{2}\sqrt{\frac{(1-\nu)\kappa D}{\rho h^5}} = \frac{\sqrt{6}}{h}\sqrt{\frac{E\kappa}{\rho(1+\nu)}} \tag{3.5-8}$$

Since the phase and group velocities are defined as follows

$$c_p = \frac{\omega}{k} = \frac{h\tilde{\omega}}{T\tilde{k}},\ c_g = \frac{d\omega}{dk} = \frac{hd\tilde{\omega}}{Td\tilde{k}} \tag{3.5-9}$$

from two real positive $\tilde{k}$, we may obtain the corresponding nondimensional phase velocities of two modes:

$$\tilde{c}_{p1} = c_{p1}\sqrt{\rho h^3/12D} = \frac{\sqrt{2\alpha\tilde{\omega}}}{\sqrt{(1+\alpha)\tilde{\omega} + \sqrt{48\alpha^2 + (1-\alpha)^2\tilde{\omega}^2}}} \tag{3.5-10}$$

$$\tilde{c}_{p2} = c_{p2}\sqrt{\rho h^3/12D} = \frac{\sqrt{2\alpha\tilde{\omega}}}{\sqrt{(1+\alpha)\tilde{\omega} - \sqrt{48\alpha^2 + (1-\alpha)^2\tilde{\omega}^2}}} \tag{3.5-11}$$

Considering Eq. (3.5-9), the derivative of Eq. (3.5-3) with respect to $\tilde{k}$ may be expressed as

$$4\alpha\tilde{k}^3 - 2[(1+\alpha)\tilde{k}^2 + 12\alpha]\tilde{\omega}\frac{d\tilde{\omega}}{dk} - 2(1+\alpha)\tilde{k}\tilde{\omega}^2 + 4\tilde{\omega}^3\frac{d\tilde{\omega}}{dk} = 0 \tag{3.5-12}$$

Solving the equation above, we get

$$\frac{d\tilde{\omega}}{d\tilde{k}} = \frac{2\tilde{k}^3\alpha - \tilde{k}(1+\alpha)\tilde{\omega}^2}{\tilde{k}^2(1+\alpha)\tilde{\omega} - 2\tilde{\omega}(\tilde{\omega}^2 - 6\alpha)} \tag{3.5-13}$$

Because of two positive real $\tilde{k}$, the nondimensional group velocities can be obtained as

$$\tilde{c}_{g1} = c_{g1}\sqrt{\rho h^3/12D} = \frac{p\sqrt{2\alpha\tilde{\omega}}\sqrt{(1+\alpha)\tilde{\omega} + p}}{(1+\alpha)p\tilde{\omega} + q} \tag{3.5-14}$$

$$\tilde{c}_{g2} = c_{g2}\sqrt{\rho h^3/12D} = \frac{p\sqrt{2\alpha\tilde{\omega}}\sqrt{(1+\alpha)\tilde{\omega}-p}}{(1+\alpha)p\tilde{\omega}-q} \tag{3.5-15}$$

where $p = \sqrt{48\alpha^2 + (1-\alpha)^2\tilde{\omega}^2}$ and $q = 24\alpha^2 + (1-\alpha)^2\tilde{\omega}^2$

3.6 Experimental Study

3.6.1 Experimental setup

An aluminum plate of Al 6061 is used in this study, whose dimensions and material properties are given in Table 3.1.

Table 3.1 Material properties and geometry of Al 6061 plate

E (GPa)	ν	ρ (kg/m^3)	h (mm)	Dimension (m×m)
72.0	0.3	2730	1.6	1.0×0.8

These values are used to calculate the predicted group and phase velocities based on Mindlin plate theory. A schematic of the experimental setup for velocity measurements is shown in Figure 3.3. Lead breaks (Pentel 0.5mm) are exerted on the surface of aluminum plate in order to excite elastic waves. For the lead break at 90º with respect to the plane of the plate, most of the motion is normal to the plate, which normally generates a large flexural mode (Gorman, 1991). Two piezoelectric sensors (PAC Micro-80) are chosen to collect the response waves due to their broadband and mini size (10mm diameter). They are coupled on the plate surface by 2211 silicone compound vacuum grease. A Tektronix's four-channel digitizing oscilloscope (TDS420A) is employed for data acquisition. Additionally, the experimental data feeds to computer for signal processing and wavelet analysis *via* GPIB bus. In this experiment, the sampling rate f_s of TDS 420A is set 5 MHz.

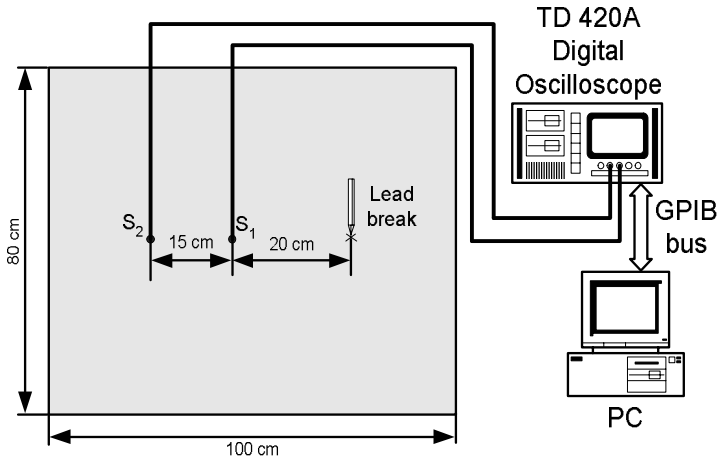

Figure 3.3 Experimental setup for the measurement of plate wave velocities

Figure 3.3 also shows the senor arrangement. For velocity measurements, two sensors S_1 and S_2 are placed at known locations along a line from the lead break source on the aluminum plate and the time difference of arrival between the sensors are then calculated. The distances to the S_1 and S_2 from the source are $l_1 = 20cm$ and $l_2 = 35cm$ respectively.

3.6.2 Determination of group and phase velocities

In the experiments, the group and phase velocities can not be obtained directly from Eq. (3.4-12) and Eq. (3.4-18), because the time origin of practical collected signals from S_1 and S_2 are simultaneously delayed to the time when physical waves excited by the lead break. Moreover, not all frequency components appear at the same time, a so-called “time lag” exists between different frequency components. Therefore, using two sensors S_1 and S_2 to measure the response waves at the same time can effectively eliminate these side effects.

The procedure of evaluating the group and phase velocities at the scale a, i.e., central angular frequency $\omega_c = \omega_0 / a$ is as follows:

1) Compute the CWT coefficients of signals collected at sensor S_1 and S_2. Figures 3.5, 3.6, 3.8, and 3.9 display the CWT results. The mother wavelet function of CWT is the Gabor wavelet.

2) Determine the arrival time b_1 and b_2 for the signal in sensor S_1 and S_2, respectively, at each scale a i.e., central angular frequency $\omega_c = \omega_0 / a$ from the magnitude map plane $\left|\mathrm{WT}_w(a,b)\right|$;

3) Use the following formula to obtain the group velocity at that scale a. (Figure 3.10, 3.13)

$$c_g = \frac{l_2 - l_1}{b_2 - b_1} \tag{3.6-1}$$

4) Due to the phase definition in calculating $\tan^{-1}$, there are many jump points in the original phase plane $\Phi_w(a,b)$ of the CWT coefficients. Applying the usual phase unwrapping method in order to change it back to a continuous curve. (Figure 3.12, 3.15);

5) According to Eq. (3.4-18), the following formula is used obtain the phase velocity at that scale a.

$$c_p = \frac{\omega_c}{k} = \frac{l_2 - l_1}{(b_2 - b_1) - \dfrac{(\theta_2 - \theta_1)}{\omega_c}} \tag{3.6-2}$$

where θ_1 and θ_2 are the corresponding phase angle at b_1 and b_2 for that scale a (Figures 3.12 and 3.15).

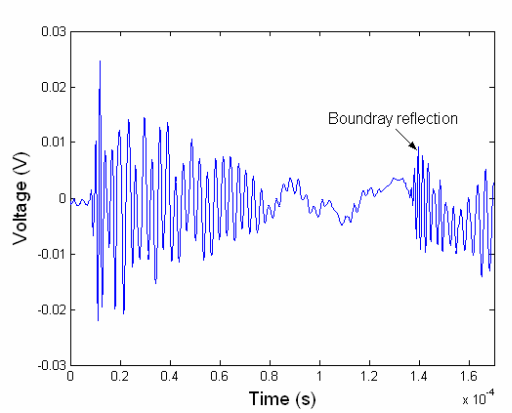

Figure 3.4 Waveform collected at sensor S_1

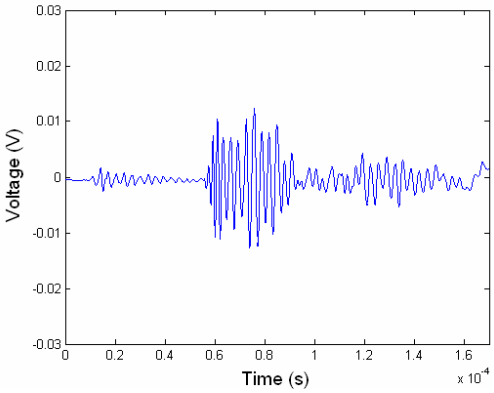

Figure 3.7 Waveform collected at sensor S_2

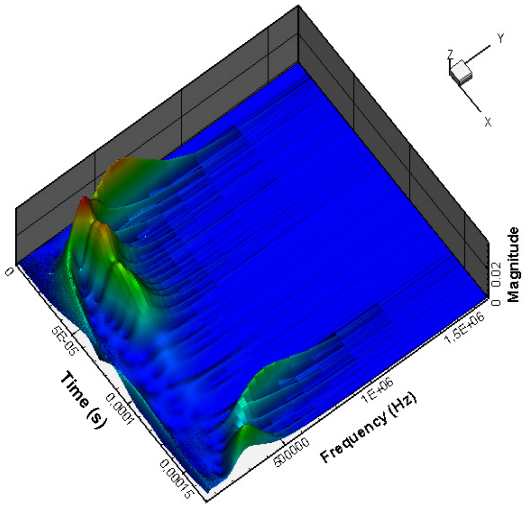

Figure 3.5 3-D view of the WT at sensor S_1

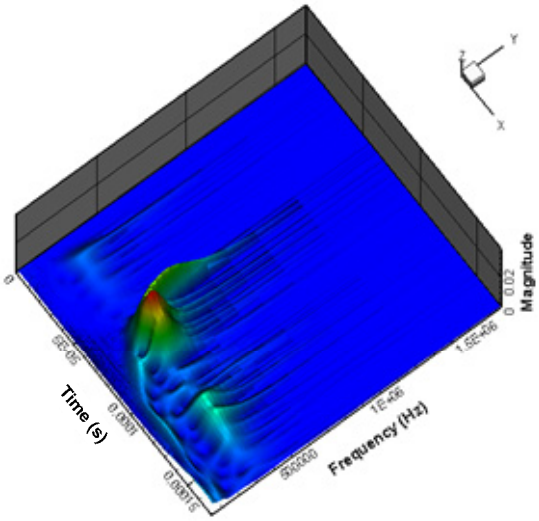

Figure 3.8 3-D view of the WT at sensor S_2

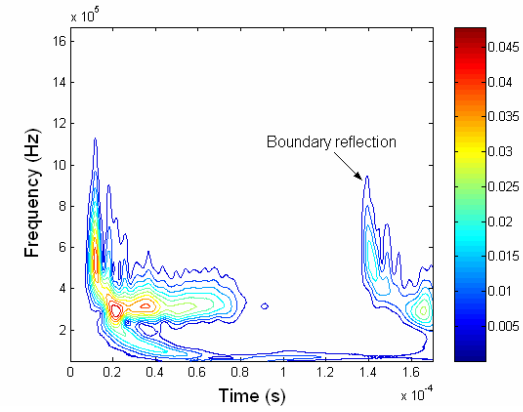

Figure 3.6 Contour plot of the WT at sensor S_1

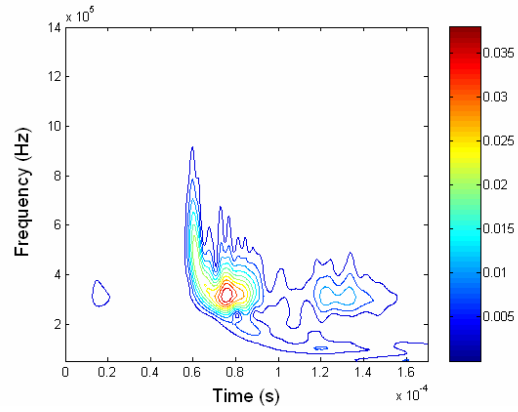

Figure 3.9 Contour plot of the WT at sensor S_2

3.6.3 Results and discussion

A typical waveform excitation from a 90º lead break on the surface of the aluminum plate is shown in Figure 3.3. In this figure, source-to-sensor distance $l_1 = 200$ mm, the flexural mode can be observed at about 10μs and the arrival of waves reflected from the boundaries can be found at around 140μs. Figure 3.5 provides visualization about the time-frequency distribution of the magnitude of the WT. The peak line of a mountain-like form located from 10μs to 60μs in Figure 3.5 is so called "wavelet ridge" (Newland, 1999 and Mallat, 1999). Physically, for each scale a, the magnitude of WT reaches the maximum at the wavelet ridge point; the corresponding time b of ridge point is the arrival time of dispersive group velocity c_g at the frequency $\omega_c = \omega_0 / a$. Figure 3.6 is the contour plot of the magnitude of the WT, which can offer more precise information on wavelet ridge location. Boundary reflection waves recorded by sensor S_1 are also observed both in Figures 3.5 and 3.6 after 140μs. Similarly, the waveform of lead break at sensor S_2 is shown in Figure 3.7 and the related 3-D view and contour plot of the time-frequency distribution of the magnitude of the WT are given in Figures 3.8 and 3.9, respectively.

Figure 3.10 is a 2D plot of the magnitude of WT coefficients of sensor S_1 at a given scale 20 (according to Eq. (3.3-6), $\hat{f} = f_s / a = 250$ kHz where sampling rate $f_s = 5$ MHz), in which b_1 indicates the arrival time, and the reflection from boundary may be observed. By use of unwrapped technique, the continuous phase angle is nearly a straight line in Figure 3.11, which can be obtained from the ordinary phase angle of WT shown in Figure 3.12. Note that the slope of the continuous phase angle at b_1 is 1.60×10^6 rad/s much closer to $2\pi \times f_s / a \approx 1.57\times10^6$ rad/s (a = 20, and sampling rate $f_s = 5$ MHz), than that of other

points. This result verifies the second formula of Eq. (3.4-16). Likewise, as for sensor S_2, Figures 3.13-3.15 illustrate the magnitude of WT, original phase angle and continuous phase angle at scale 20. In addition, b_2 and θ_2 denotes in the associated plots. Also the slope of the continuous phase angle at b_2 is 1.590×106rad/s, which is close to theoretical value 1.579×10^6 rad/s.

After knowing b_1, b_2, θ_1 and θ_2, the group and phase velocity for the first mode may be computed by using Eq. (3.6-1) and Eq. (3.6-2) for a given scale. With the change of scale, the dispersive group and phase velocities versus frequency can be finally obtained. Figure 3.16 shows the measured group and phase velocities of the flexural mode, moreover the solid line and dashed line in Figure 3.16 are the theoretical group and phase velocities based on Mindlin plate theory. The measured group velocity agrees well with the theory in the frequency range of 0-5MHz. The measured phase velocity shows good agreement in the low frequency range, but small discrepancy in the high frequency range. The reason is that noise contaminates the response signals and this effect may add up by using the unwrapped phase technique. Further study should investigate some effective way to denoise in phase angle such that the accuracy of measured phase velocity can be improved.

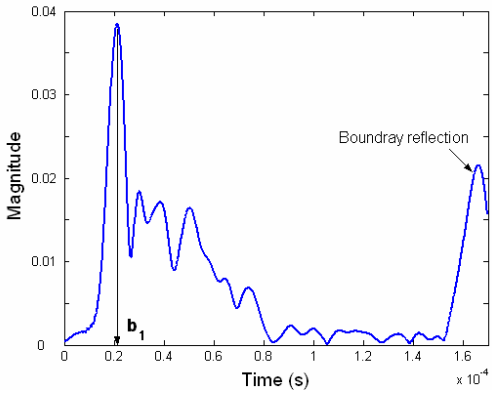

Figure 3.10 The magnitude of WT coefficients of sensor S_1 at scale 20 (250kHz)

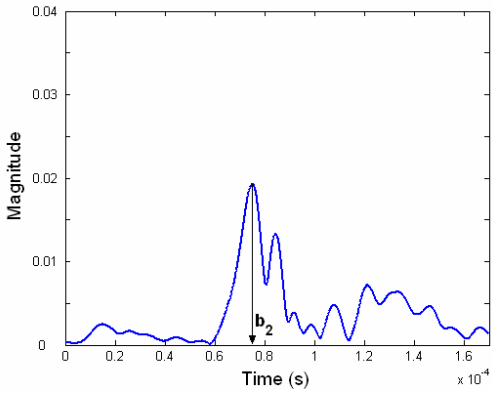

Figure 3.13 The magnitude of WT coefficients of sensor S_2 at scale 20 (250kHz)

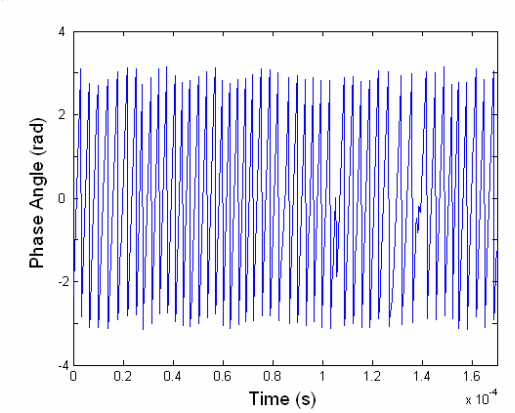

Figure 3.11 The phase angle of WT coefficients of sensor S_1 at scale 20 (250kHz)

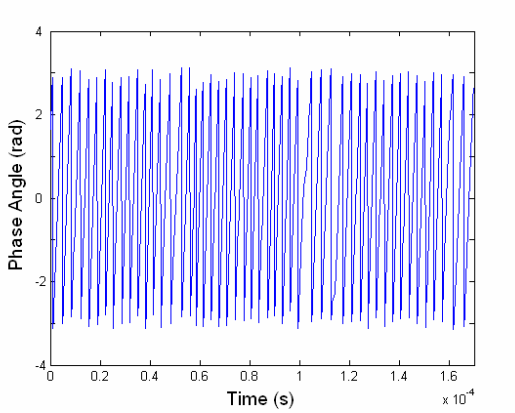

Figure 3.14 The phase angle of WT coefficients of sensor S_2 at scale 20 (250kHz)

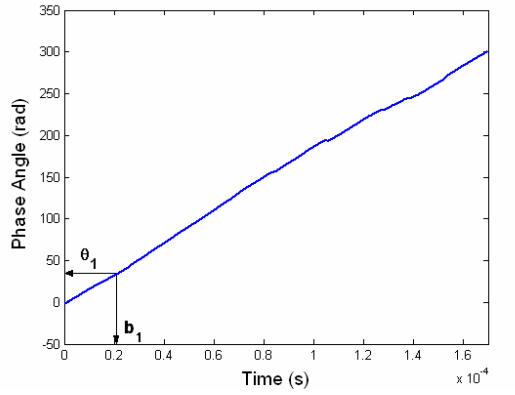

Figure 3.12 The unwrapped phase angle of WT coefficients of sensor S_1 at scale 20 (250kHz)

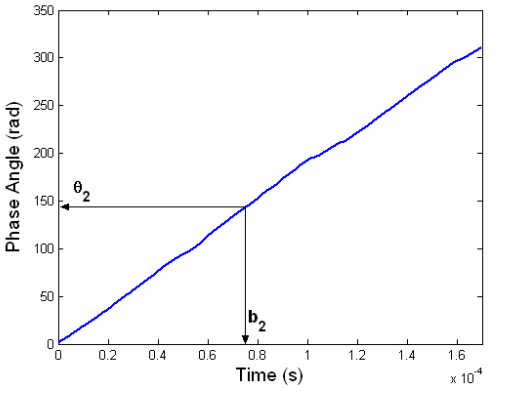

Figure 3.15 The unwrapped phase angle of WT coefficients of sensor S_2 at scale 20 (250kHz)

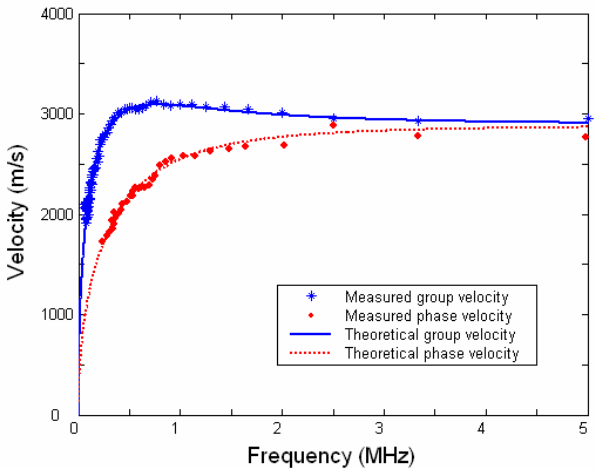

Figure 3.16 Measured and theoretical group/phase velocities of flexural dispersive waves

4 Least-squares Damage Localization Using Elastic Wave Energy Measurements

In this Chapter, a damage localization technique based on a least-squares method is mathematically deduced and verified *via* both numerical simulation and experiments. Firstly, an elastic wave energy decay model for wave propagating in plates is established. Secondly, the least-squares method is applied to iteratively search localized damage based on elastic wave energy measurements. Thirdly, simulation examples for single damage detection are demonstrated. Finally, a simple experimental system is set up to validate the feasibility of the least-squares method for damage localization in an aluminum plate. From the simulated results and experimental data, it is shown that the estimated damage position by the least-squares method makes good agreement with the targeted damage location.

A number of assumptions are made in developing the wave energy decay model for energy based damage localization. These assumptions are:

1) Since the isotropic aluminum plate is tested, group velocity is independent of wave propagation direction because the isotropic aluminum plate is tested;
2) The size of incipient damage is relatively small so that reflected waves from the damage can be treated as a secondary wave point source;
3) Excitation wave signals are narrow banded and their central frequencies are lower than the cut-off frequency. Thus the dispersion effect is largely neglected. All the excitation wave signals are dominated by the A_0 mode;
4) The received sensor data are reasonably large such that the noise can be characterized. The noise is assumed to follow stationary Gaussian distribution.

4.1 An Elastic Wave Energy Decay Model

In wave analysis of isotropic plates, Yang and Yuan (2004) have recently developed asymptotic solutions of flexural waves in isotropic plates using Mindlin plate theory.

Applying the stationary phase method, the asymptotic solutions for long time and distance with r/t held fixed can be expressed as

$$w(r,t) \sim \sqrt{\frac{2\pi}{rt}} \sum_{\substack{stationary \\ point\ s\ k}} \frac{F_1(k)}{\sqrt{\omega''(k)}} \exp i[kx - \omega(k)t - \frac{\pi}{4}\operatorname{sgn}\omega''(k)] \tag{4.1-1}$$

$$\psi(r,t) \sim \sqrt{\frac{2\pi}{rt}} \sum_{\substack{stationary \\ point\ s\ k}} \frac{F_2(k)}{\sqrt{\omega''(k)}} \exp i[kx - \omega(k)t - \frac{\pi}{4}\operatorname{sgn}\omega''(k)] \tag{4.1-2}$$

where $k = k(r,t)$ is the stationary point which is root of the equations $\omega(k) = r/t$, $\omega(k)$ is the dispersion relation Eq. (3.5-2) based on Mindlin plate theory, the wave propagation distance r equals to $c_g t$; $F_1(k), F_2(k)$ are associated with the initial conditions or loading. Note that the above equations are valid for $d^2\omega/dk^2 \neq 0$ and single wave mode (Yang and Yuan, 2004).

Figure 4.1 displays group dispersion relations of flexural wave from both Mindlin plate theory (pointed line) and elasticity theory (solid line). Two wave modes A_0 and A_1 can be obtained in the dimensionless frequency range of (0, 0.529) or dimensional frequency range (0, 1MHz). It may be seen that the Mindlin plate theory and elasticity theory match very well over the beginning portion of each mode. In order to only generate A_0 mode, the excitation frequency of actuator must be less than the first cut-off frequency 0.267 (or dimensional frequency 505 kHz). Furthermore, since Eq. (4.1-1) and (4.1-2) are valid in the region of $d^2\omega/dk^2 \neq 0$, the frequency of excitation signal should avoid the flat portion of the

dispersion curve of A_0. Accordingly, in this study the excitation frequency of actuator is chosen as 50 kHz.

In order to obtain the reflected waves solely from damages, the response wave signals at each sensor are measured: before and after damages occurred, then the pre-damage wave signals are subtracted from the post-damage wave signals. Let M be the number of sensors, N be the data length collected by each sensor and only one damage exits in the plate. Figure 4.2 shows the scheme of sensor and actuator deployment with the damage location.

In the region of $d^2\omega/dk^2 \neq 0$, since $r = c_g t$, it can be concluded from Eqs. (4.1-1) and (4.1-2) that the amplitude of elastic waves propagating in a plate decays at a rate inversely proportional to the propagation distance. Thus the signal received by each sensor can be modeled as:

$$x_m(n) = s_m(n) + \upsilon_m(n), \quad m = 1, 2, \cdots, M, \; n = 1, 2, \cdots, N \tag{4.1-3}$$

and

$$s_m(n) = \gamma_m \frac{\alpha a_0(n - t_m - \tau)}{\left\| \boldsymbol{\rho} - \mathbf{r}_m \right\|} \tag{4.1-4}$$

where $x_m(n)$: the n^{th} value sampled at the m^{th} sensor over time interval $1/f_s$;

f_s is the sampling rate;

$\upsilon_m(n)$: zero-mean additive white Gaussian noise of sensor m with variance σ_m^2;

γ_m: sensor gain factor of the m^{th} sensor;

$\boldsymbol{\rho}$: the position vector of the damage;

$\mathbf{r}_m$: Cartesian coordinates of the sensor m;

α: reflection factor or the initial amplitude at the damage;

$a_0(n-t_m-\tau)$: normalized reflected waveform from damage with unit peak-to-peak value;

t_m : time delay from the damage to sensor *m*;

τ : time delay from the actuator to the damage.

$$t_m = \frac{\|\boldsymbol{\rho}-\mathbf{r}_m\|}{c_g} \text{ and } \tau = \frac{\|\boldsymbol{\rho}-\mathbf{r}_0\|}{c_g} \tag{4.1-5}$$

where $\mathbf{r}_0$ is a given vector denoting Cartesian coordinates of the actuator, c_g indicates the group velocity and the operator $\|\ \|$ indicates Euclidean distance.

The excited waves from an actuator is a Hanning window modulated sinusoid loading governed by the following function:

$$q(t) = P[\mathrm{H}(t)-\mathrm{H}(t-N_p/f_c)]\times[1-\cos(2\pi f_c t/N_p)]\sin(2\pi f_c t) \tag{4.1-6}$$

where $\mathrm{H}(t)$ is the Heaviside step function, *P* is the voltage, N_p is the number of peaks of the loading and f_c is the central frequency. In this study, $N_p = 5$, and $f_c = 50\text{kHz}$ are used.

The reflected waveform also has the same shape as Eq (4.1-4), thus we have $a_0(t) = [\mathrm{H}(t)-\mathrm{H}(t-N_p/f_c)]\times[1-\cos(2\pi f_0 t/N_p)]\sin(2\pi f_0 t)$ and the expectation of $a_0(n)$, or even its delay, equals to zeros if *N* is large enough.

$$\mathrm{E}[a_0(n)] = 0, \quad \mathrm{E}[a_0(n-t_{km}-\tau_k)] = 0 \tag{4.1-7}$$

Assume $s_m(n)$ and $\upsilon_m(n)$ are uncorrelated such that $\mathrm{E}[s_m(n)\upsilon_m(n)] = \mathrm{E}[s_m(n)]\,\mathrm{E}[\upsilon_m(n)] = 0$, we get

$$\mathrm{E}[x_m^2(n)] = \mathrm{E}[s_m^2(n)] + \mathrm{E}[\upsilon_m^2(n)] \tag{4.1-8}$$

The expectation of energy is calculated by averaging over a time window $T = N / f_s$. Denoting the scalar $\mathrm{E}[x_m^2(n)]$ as y_m and knowing the $\mathrm{E}[\upsilon_m^2(n)]$ equals its variance σ_m^2, the energy decay model can be expressed as:

$$y_m = \mathrm{E}[x_m^2(n)] = \frac{1}{N}\sum_{n=1}^{N} x_m^2(n) = \frac{g_m}{N}\sum_{n=1}^{N}\left[\frac{\alpha a_0(n - t_m - \tau)}{\|\boldsymbol{\rho} - \mathbf{r}_m\|}\right]^2 + \sigma_m^2 \tag{4.1-9}$$

where $g_m = \gamma_m^2$ and note that $a_0(n - t_m - \tau)$ is a $N \times 1$ vector.

In practice, y_m is the measured energy which is calculated from the N reflected wave signals at the m^{th} sensor, furthermore, y_m may be viewed as the extracted characteristic from the collected data at the m^{th} sensor. σ_m^2 is the variance of background noise affecting sensor m and can be measured from the collected signal. Thus, before performing any optimization algorithm, we need to obtain $2M$ known values $\{y_1, y_2 \quad \cdots \quad y_M \; ; \quad \sigma_1, \sigma_2 \quad \cdots \quad \sigma_M\}_{2M}$.

In Eq. (4.1-9), we have two unknown variables of the damage location coordinates $\boldsymbol{\rho} = (\rho_1, \rho_1)$ and one unknown damage reflection factor α, that is, the three unknown parameters are defined as

$$\boldsymbol{\theta} = \{\rho_1 \quad \rho_2 \quad \alpha\}_3 \tag{4.1-10}$$

Since there are totally three unknown variables, there must be at least three or more sensors reporting wave energy measurements to yield a solution.

4.2 Least-squares Damage Localization Method

Several methods based on elastic waves have been investigated for damage localization. Tobias (1976) presented a triangulation method to detect single damage in a plate with three sensors. He approached the problem as three interesting circles, each

centered at a sensor, with their radii determined by the time of propagation of the wave from the source to the respective sensor. Jeong and Jang (2000) proposed another triangulation method, in which the time difference of arrival (TDOA) between two sensors was evaluated first, and then the damage located at the crossing point of two hyperbolas. However, there are two disadvantages of these two methods. First, these two triangulation methods are based on acoustic emission technique, which is passive sensing but not active detection. Thus they are not suitable for SHM. Second, these two methods must evaluate the arrival time or TDOA of the response waves. Due to the ambiguity of time-arrival and background noise, the measurement of time-arrival may not be accurate enough to be determined and incurs additional errors to the localization results. Although Kehlenbach and Hanselka (2003) developed an active damage localization technique by using reflected Lamb waves from damage, the time-of-flight was still needed to be evaluated in advance. In this thesis, a least-squares method uses the energy measurement of the collected elastic wave signals such that it uses all the data information including the time-of-flight. Furthermore, since the least-squares method is based on active detection technique to obtain the reflection waves, it is a promising method for the application of SHM.

In the least-squares method, the unknown variables are iteratively updated to make the following error function between the modeled record and measured data reach its minimum:

$$J(\boldsymbol{\theta}) = \frac{1}{2}\sum_{m=1}^{M}(Z_m - y_m)^2 \tag{4.2-1}$$

where Z_m is the modeled wave energy and y_m is the measured wave energy at sensor *m*, respectively.

The gradient of $J(\boldsymbol{\theta})$ with respect to α is

$$\frac{\partial J(\boldsymbol{\theta})}{\partial \alpha} = 2\alpha \sum_{m=1}^{M} g_m (Z_m - y_m) \frac{1}{N} \sum_{n=1}^{N} \frac{a_0^2 (n - t_m - \tau)}{\left\| \boldsymbol{\rho} - \mathbf{r}_m \right\|^2} \tag{4.2-2}$$

The gradient of $J(\boldsymbol{\theta})$ with respect to the p^{th} component of damage coordinates $\boldsymbol{\rho}$ can be expressed as

$$\begin{aligned} \frac{\partial J(\boldsymbol{\theta})}{\partial \boldsymbol{\rho}_{.p}} = 2\alpha^2 \sum_{m=1}^{M} g_m (Z_m - y_m) \frac{1}{N} \sum_{n=1}^{N} \Bigg[& \frac{(r_{m.p} - \rho_{.p}) a_0^2 (n - t_m - \tau)}{\left\| \boldsymbol{\rho} - \mathbf{r}_m \right\|^3} \\ & + \frac{2}{c_g} \frac{a_0 (n - t_m - \tau) a_0' (n - t_m - \tau)}{\left\| \boldsymbol{\rho} - \mathbf{r}_m \right\|^2} \cdot \left(\frac{r_{m.p} - \rho_{.p}}{\left\| \boldsymbol{\rho} - \mathbf{r}_m \right\|} + \frac{r_{0.p} - \rho_{.p}}{\left\| \boldsymbol{\rho} - \mathbf{r}_0 \right\|} \right) \Bigg] \end{aligned} \tag{4.2-3}$$

where the subscript $.p$ denotes the p^{th} component of coordinates and sub-prime is the derivative with respect to its argument.

Then for the next iteration the variables will be updated as

$$\alpha^{(i+1)} = \alpha^{(i)} - \varsigma_1 \frac{\partial J(\boldsymbol{\theta})}{\partial \alpha} \tag{4.2-4}$$

$$\boldsymbol{\rho}_{.p}^{(i+1)} = \boldsymbol{\rho}_{.p}^{(i)} - \varsigma_2 \frac{\partial J(\boldsymbol{\theta})}{\partial \boldsymbol{\rho}_{.p}} \tag{4.2-5}$$

where ς_1 and ς_2 are positive scalar called step size.

The above procedure leads to a so-called Gradient optimization algorithm:

Gradient optimization algorithm

Initialization:

Initial damage positions $\{\boldsymbol{\rho}\}$ *and*

damage reflection factors α

Repeat until convergence

Calculate Eq. (4.2-2) and Eq. (4.2-3)

Update Eq. (4.2-4) and Eq. (4.2-5)

The convergence criterion is given by

$$\left\| \boldsymbol{\rho}^{(i+1)} - \boldsymbol{\rho}^{(i)} \right\| \leq 0.0001 \tag{4.2-6}$$

4.3 Simulations and Experiments

4.3.1 Simulation examples

In this section, simulation results of a single damage localization case based on the proposed least-squares method is illustrated as follows. The aluminum plate (Al-6061) used in this study and its material properties are previous listed in Table 3.1. The central frequency of the excitation signal is set as 50 kHz which is less than the cut-off frequency of A_1 waves such that only the lowest antisymmetric wave A_0 can exist. Using the Lamb wave theory, we can calculate the group velocity of the lowest symmetric wave A_0. The group velocity c_g in the above equations equals to 2107m/s.

In order to generate the wave signal received by each sensor, a finite difference algorithm based on Mindlin Plate theory is used to synthesize the waves in the aluminum plate (Lin, 2000 and Lin and Yuan, 2001b). A 600×600 finite difference mesh is with uniform square grid space $\Delta x = \Delta y = 2.54$mm superimposed on the plate region. The thickness of the plate is 0.32cm. The origin of the coordinate system is set at the center of the plate. One damage is modeled as a point diffractor at (20,10)cm. The point damage is modeled as a material with 16 times value of the bending stiffness for the undamaged plate. In addition, four sensors are located at (-30,30)cm, (30, -30)cm, (30, 30)cm and (-30, 30)cm. The parameters of excitation signal in Eq. (4.1-6) are set as $N_p = 5$, and $f_c = 50$kHz . Figure 4.3 displays the simulated damage reflected wave signals received at four sensors by using the finite difference algorithm. Since the plate is large enough to guarantee that no reflection from the boundary during the time span of data record. From Figure 4.3, it may be seen that

the damage reflected waves form the damage are still packed in the time domain under the five-peak excitation, but the slight dispersion effect can still be observed.

The additive white noise of each sensor is set the same as Gaussian noise with mean $\mu = 0$ and standard variance $\sigma^2 = 0.01$. Every sensor shares the same the same gain factor $\gamma_m = 200$. In addition, the signal to noise ratio (SNR) is defined in the following to evaluate the effect of additive noise:

$$SNR = 10\log\frac{y-\sigma^2}{\sigma^2}\text{db} \tag{4.3-1}$$

where y is the measured wave energy at a sensor.

Figure 4.4 shows the reflected waveform after adding Gaussian noise and the calculated SNR at each sensor. In order to detect single damage locating at (20, 10)cm, from Section 4.1, the minimum number of sensor is 3. Figure 4.5 and Figure 4.6 show the finial localization results and the performance of searching for three-sensor setup and four-sensor setup, respectively. Note that the searching track in plot (b) of two figures is updated every forty steps

The simulated data records from sensor 1 to sensor 3, which are shown in Figure 4.4, are used for damage location with three-sensor setup. In Figure 4.5(a), although the estimated location tends to approach the targeted damage location, the rate of convergence is decreased greatly. It may be seen from Figure 4.5(c) the location error remains after 1400 epoch, and is still close to 4 even after 4000 epochs. Note that the location error is the Euclidean distance between the ideal location and estimated location. The estimated damage location is (16.7, 12.1)cm which is deviated from the targeted damage location by 3.9cm. Comparing with

distance 60 cm between sensor 1 and sensor 2, the method may be acceptable in practical applications.

Compared with three sensors case, the searching procedure will speed up remarkably when four sensors are used. After 500 epochs, it reaches the location error 1.2. Thus the more sensors can effectively reduce the number of epochs. On the other hand, more sensors may also add up the computational cost of the optimization algorithm. There is a trade-off between the numbers of sensors and computational cost. Generally the former effect is dominant, thus the number of sensors should be somewhat larger than the necessary number of sensor in the application of real-time damage detection. The estimated damage location is (18.8, 10.1)cm and the error with respect to the targeted damage location (20, 10)cm is 1.2cm.

Figure 4.6(a) shows the different searching tacks with different initial guess positions. From this figure, it can be seen that this method has a robust performance and good convergence.

4.3.2 Experimental study

In this section, the least-squares method is performed on experimental signals to validate its capability of damage localization. An aluminum plate Al-6061 with dimension $91\times91\times0.32cm^3$ is prepared and two circular rare-earth magnet stones with diameter 1.2cm are put on both sides of the plate at (20,10)cm to simulate a damaged area. Table 3.1 lists the material properties of the plate. A pair of PZT disks (Navy Type II PKI502) are mounted on upper and lower sides at the central point of the plate to act as an actuator and the other four pieces of PZT disks are bonded near the four corners of the plate. Note that the diameter of PZT sensor is 6.4mm and the thickness is 1.57mm. The experimental setup as shown in Figure 4.7 consists of a HP 33120A function generator, a Tektronix TDS 420A digital

oscilloscope, and a computer connected through a GPIB interface. The HP 3220A function generator is used to generate a 50 KHz five-peak signal with a 10Hz repetition rate. The signal is sent to TDS420A oscilloscope and K-H7602 amplifier. The sampling rate of TDS420A is set as 500kHz. The peak voltage of the excitation signal from the amplifier is kept at 50V, which translates into an electric field intensity of about 31.25V/mm, below the maximum operating field of 300 Vmm^{-1}. Then the response signals measured by sensors are displayed and stored in the digital oscilloscope. Finally, the computer obtains the collected date via GPIB interface and runs the least-squares algorithm to estimate the damage location.

In Figure 4.8, the upper plot shows the waveform of the excitation signal in time domain, the middle plot displays the response wave signals collected by sensor 3 before and after damage, and the lower plot is the reflected wave, which is obtained by subtracting the response wave signal before damage from the response wave signal after damage. From the reflected wave signal, it can be seen that first the wave pack is directly from the damage. However, besides the first arrival pack (at 270μs), several wave packs are also observed in the lower plot of Figure 4.8. Since the simulated damage using magnetic stone mounted the plate, the wave packs between 300μs and 700μs are the scattered waves from the boundary of the damage; and the wave packs after 700μs are generated from the boundary reflection of the aluminum plate. Figure 4.9 shows the reflected wave signals from damage received by the four sensors.

In order to eliminate the scattered waves and extract the first damage reflected wave pack, a discrete wavelet transform (DWT) is performed before running the least-squares algorithm. Firstly, the original signal is decomposed into five levels by using DWT, in which one approximation signal a_5 and five detail signals d_1~d_5 may be obtained. Figure 4.10 shows

the structure of decomposed signals and their corresponding frequency bandwidth. Since the sampling rate is 500kHz, based on the Shannon Theory (Shannon, 1949 and Mallat, 1998) the maximum frequency $f_{\max}$ of received signal is 250kHz. On the other hand, the excitation signal is narrow-banded and its central frequency equals to 50kHz. Thus, the bandwidth of level 3, which is (31.25, 62.5)kHz, covers 50kHz signals, i.e. the most energy concentrates in this level as shown in Figure 4.11. Secondly, in level 3 the portion of the signal after the first reflection is set to zero and the other portions in this level are unchanged. Additionally, the composed signals in other levels remain unchanged. Thirdly, after performing the elimination of scattered waves, the wave signal can be reconstructed by using d_1~d_5 levels. Figure 4.12 shows the reconstructed singles at sensor 3. Repeat this procedure for the rest of the original signals collected by sensors, the damage reflected waves signal can be extracted as shown in Figure 4.13.

With the extracted wave signal as shown in Figure 4.8, the least-squares method can be performed on these signals and the position of damage will be estimated iteratively. Figure 4.14 illustrates the experimental results of damage localization by the least-squares method, in which the different searching tacks with different initial guess positions and the star indicates the targeted damage. The estimated damage position is (18.6, 10.7)cm and the error with respect to the target damage location (20, 10)cm is 1.5cm. From this figure, it can be seen that this method has a robust performance and good convergence.

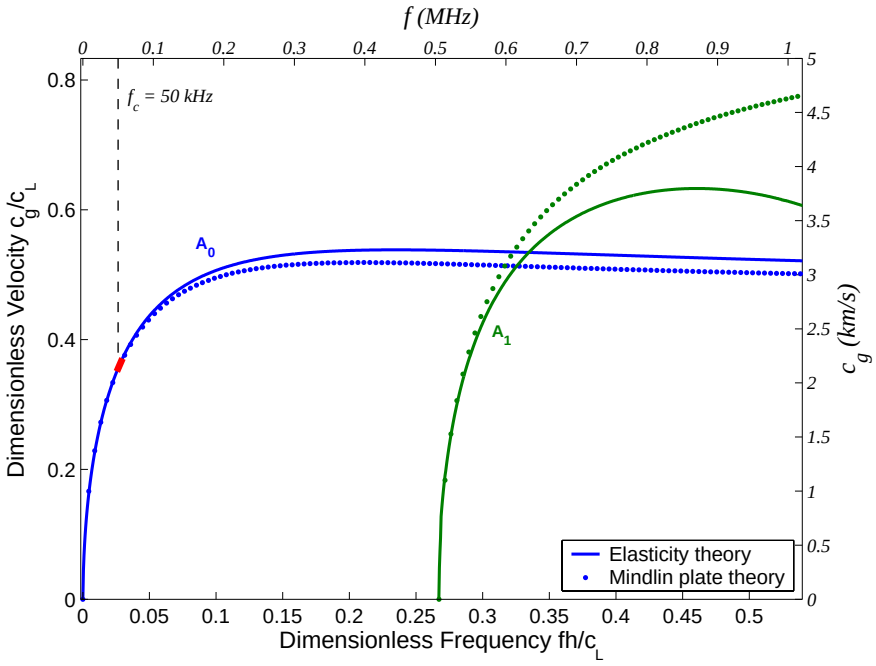

Figure 4.1 Dispersion curves of flexural waves from Lamb wave theory and Mindlin plate theory

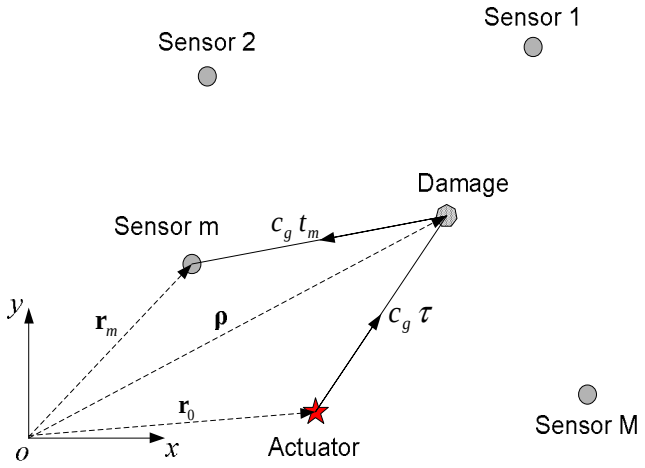

Figure 4.2 Scheme of sensor/actuator deployment and unknown damage

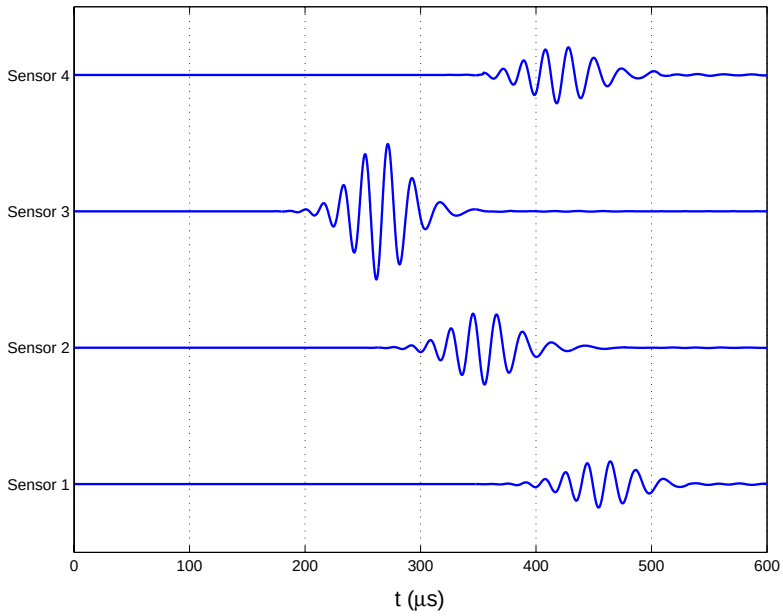

Figure 4.3 Simulated reflected wave packs from the damage using finite difference method

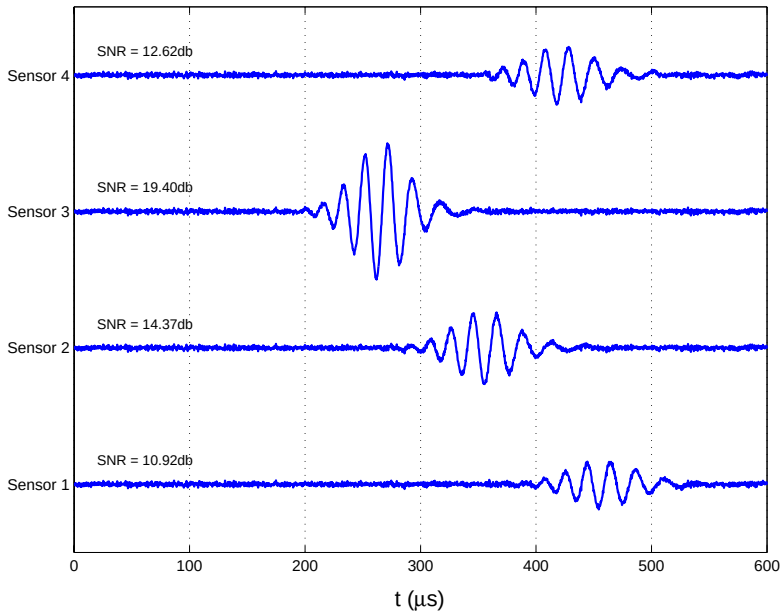

Figure 4.4 Simulated reflected wave packs with the zero-mean additive Gaussian noise

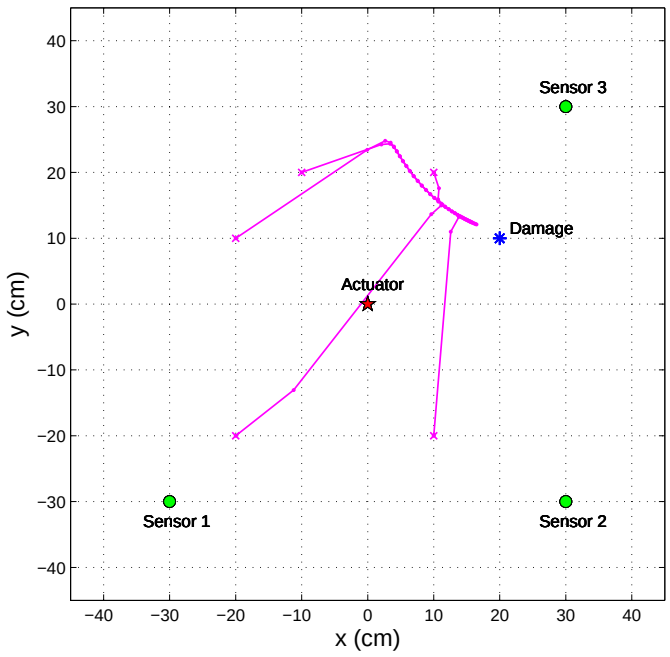

(a)

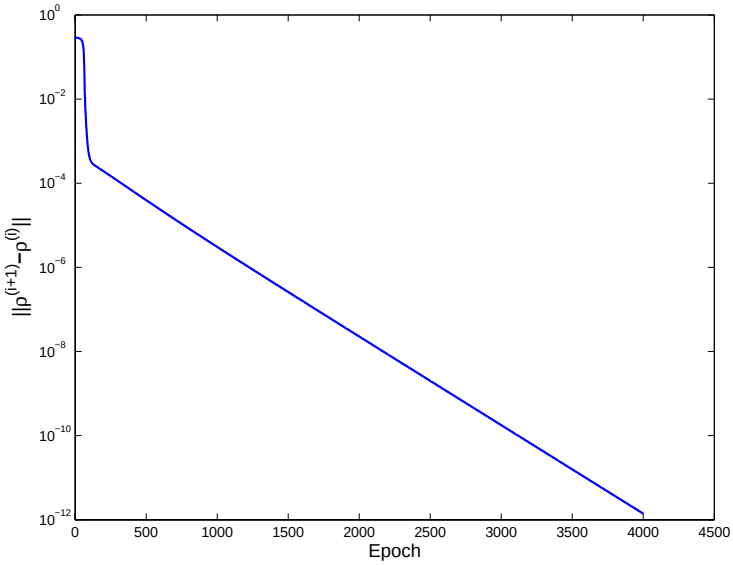

(b)

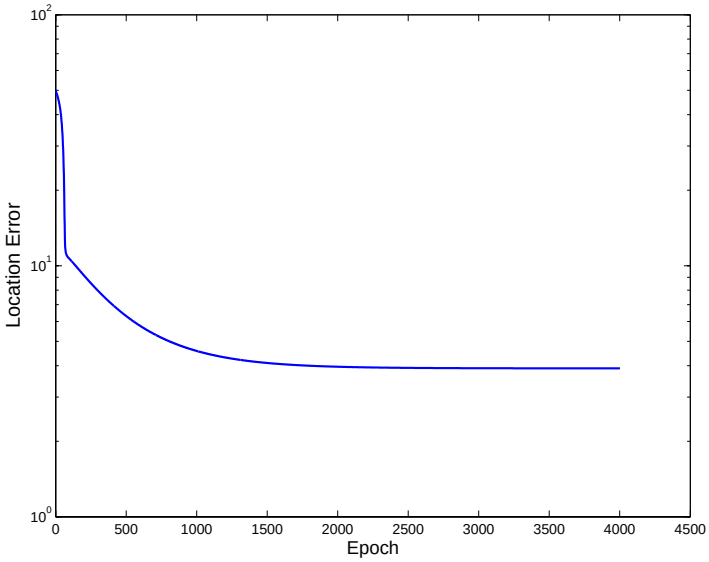

(c)

Figure 4.5 Single damage localization using three sensors

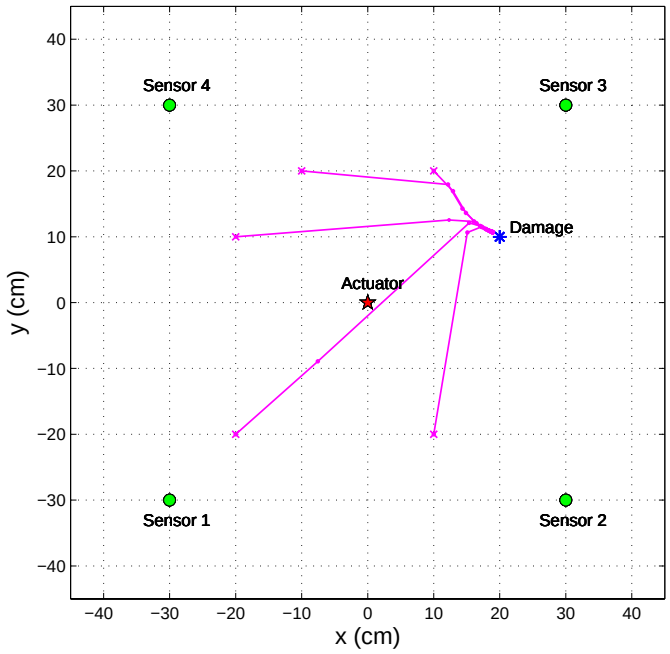

(a)

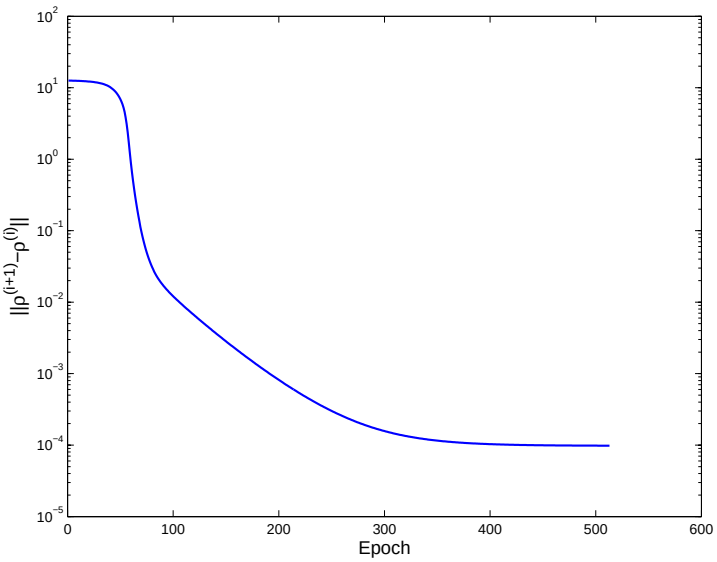

(b)

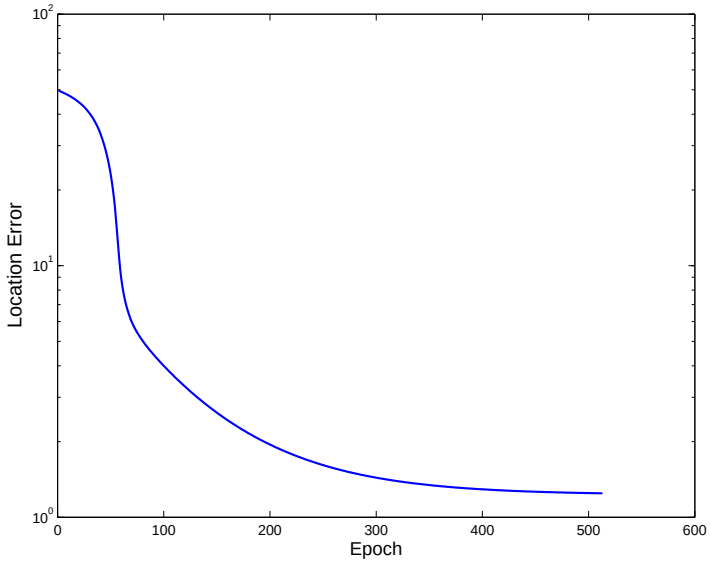

(c)

Figure 4.6 Single damage localization using four sensors

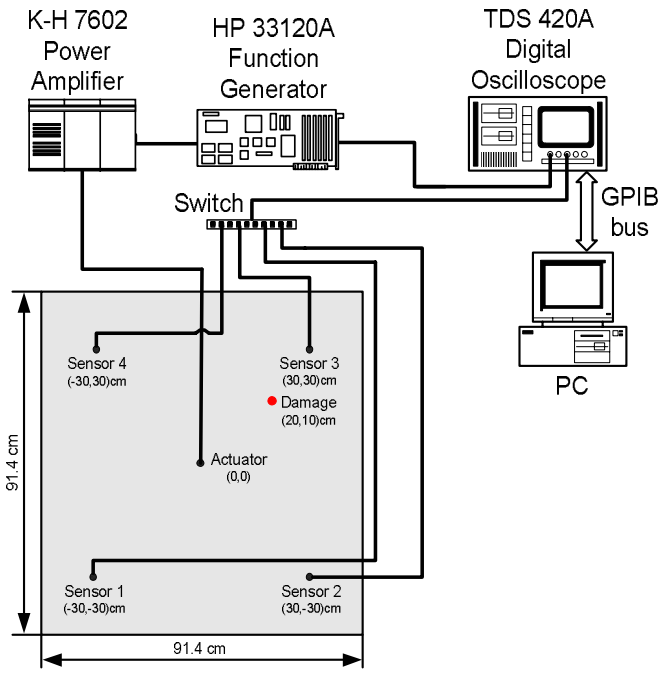

Figure 4.7 Experimental setup for damage localization

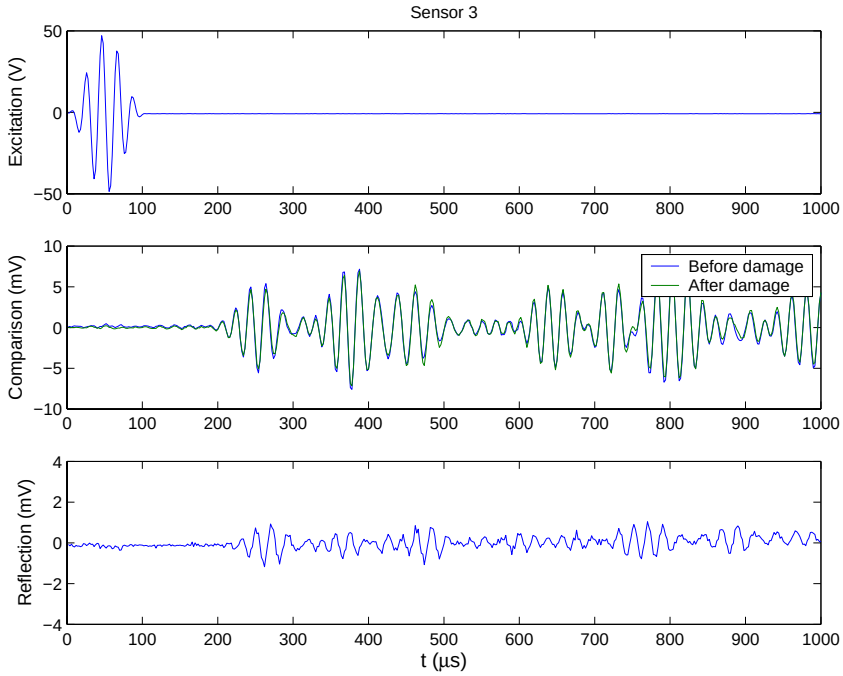

Figure 4.8 The excitation waveform, the response wave signals before and after damage, and the reflected waves at sensor 3

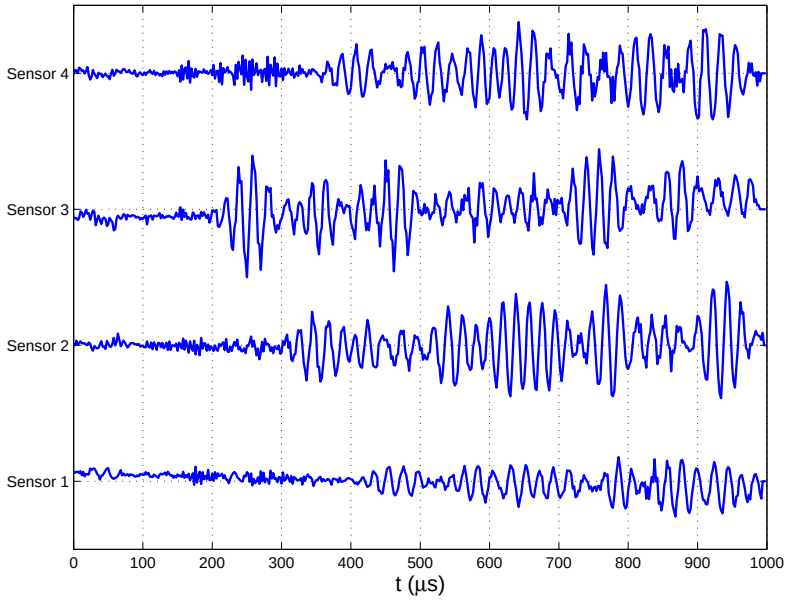

Figure 4.9 The reflected wave signal received by each sensor

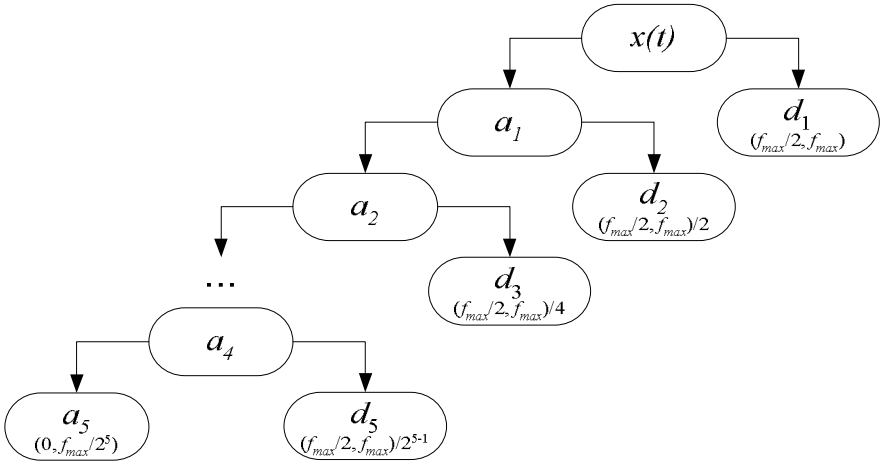

Figure 4.10 Tree decomposition algorithm of DWT and bandwidth of each level

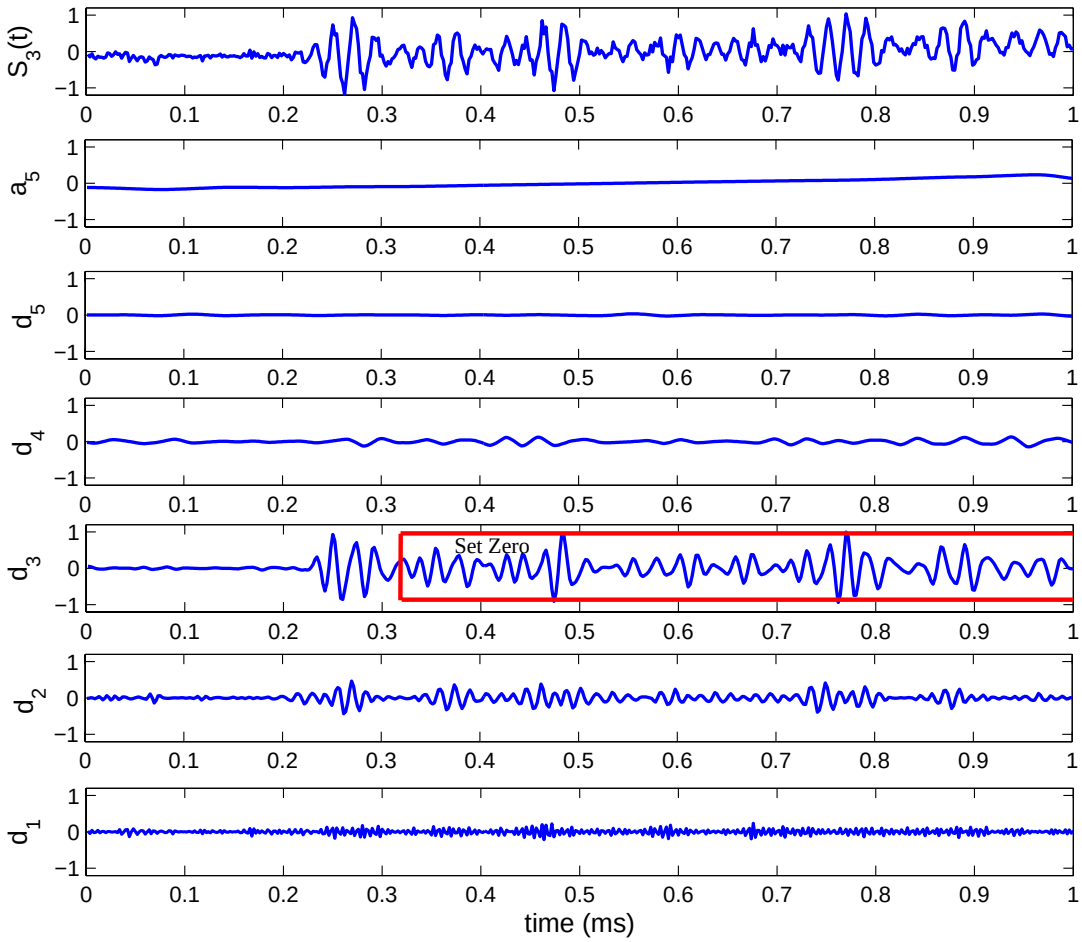

Figure 4.11 The original signal at sensor 3, its decomposed signals by DWT and extraction of the first reflection at level 3

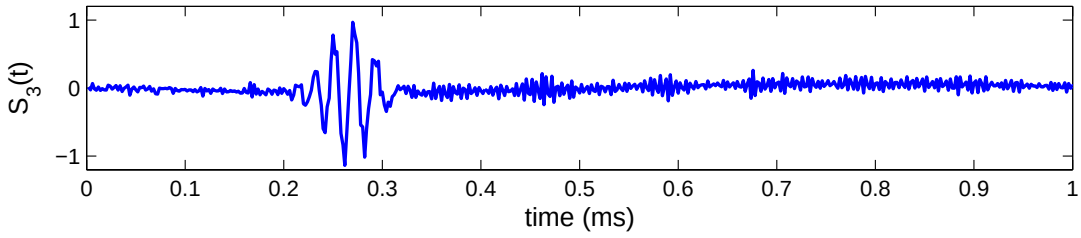

Figure 4.12 The reconstructed signal at sensor 3 by using DWT and extraction of the first reflected wave signal

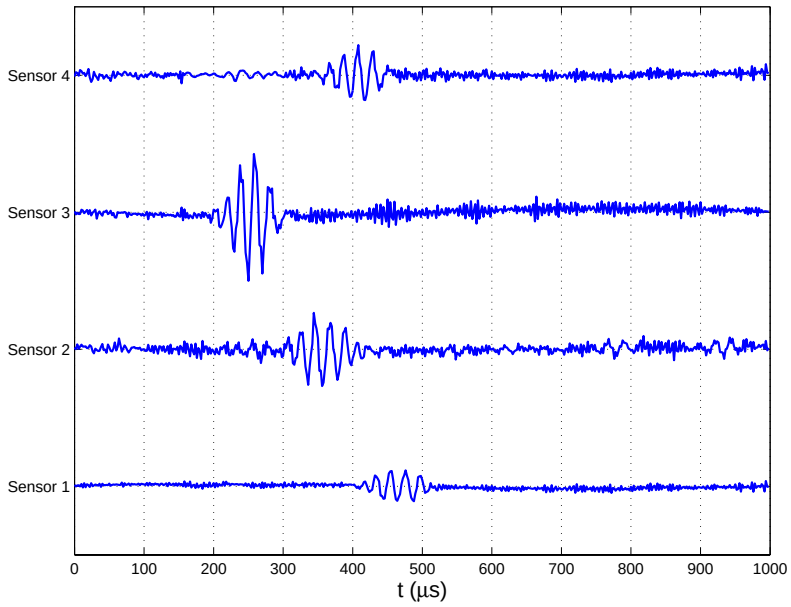

Figure 4.13 The reflected wave pack directly from the damage received from each sensor after DWT

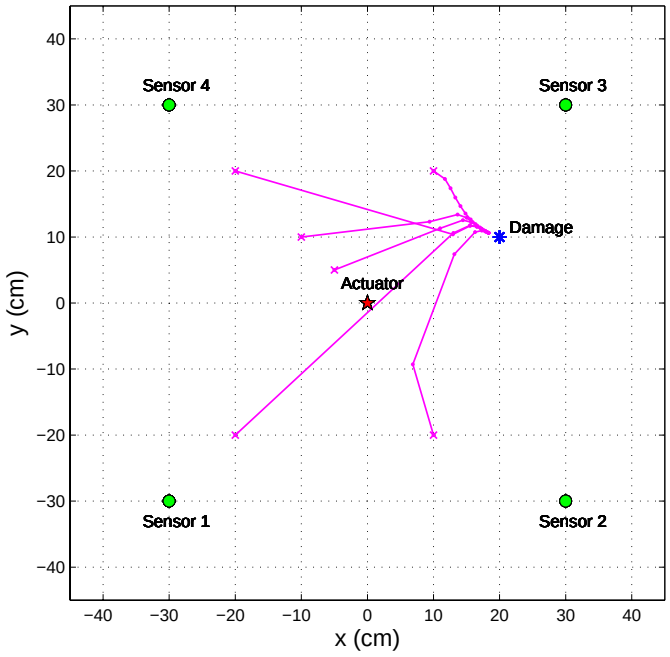

Figure 4.14 Experimental result of damage localization by least-squares method

5 Discussion and Conclusions

5.1 Conclusions

In this study, dispersion relations in composite laminates are investigated by both 3-D elasticity theory and a higher-order plate theory; and then a least-squares method is first introduced to SHM field for damage localization based on elastic waves in plates. Experiments studies are performed in this thesis, which consist of comparing the dispersion relations obtained by WT with the theoretical values and verifying the effectiveness of least-squares damage localization.

Specific contributions of this study to the field of research can be summarized as follows:

(a) Exact solutions of elastic waves in composite laminates with arbitrary propagation direction are obtained from 3-D theory elasticity. The dispersion relations of infinite symmetric and antisymmetric wave modes are numerically solved.

(b) A higher-order plate theory is extended to obtain approximate solutions of waves propagating along an arbitrary direction in composite laminates. The dispersion relations of three antisymmetric wave modes and five symmetric wave modes can be analytically solved.

(c) Not only the dispersion curves of phase velocity but also of group velocity are computed. From the compared results of the exaction solutions and approximation solutions, it may be seen that the higher-order plate theory gives good agreements with 3-D elasticity theory in the range of higher frequency. Especially for S_0 and A_0 modes, the two theories match very well.

(d) Gabor WT is directly performed on a dispersive wave to extract the time-frequency information. Consequently, the dispersion of not only group velocity but also phase velocity can be mathematically obtained.

(e) Experiments are performed by using a lead break as the simulated acoustic emission source on the surface of aluminum plate. The dispersion curves of both phase and group velocities of the lowest antisymmetric wave mode obtained from the experiments by using WT show good agreement with theoretical prediction values.

(f) A least-squares method is first applied to SHM field for iteratively searching damage location based on elastic wave energy measurements. The proposed method has a number of advantages over existing triangulation methods: first, the method is an active damage detection technique which is suitable for the applications of SHM; second the method uses the all time series data information collected by each sensor not only the time-of-flight or time of arrival; lastly the environmental noise can be taken into account.

(g) Simulated examples for damage detection based on a finite difference algorithm are demonstrated by using the least-squares method. Moreover, an active SHM system is set up to validate the feasibility of the least-squares damage localization method. From the simulated and experimental results, it is shown that the estimated damage location by least-squares method makes good agreement with the targeted location.

5.2 Future Studies

Although WT is an effective signal processing tool for nonstationary signals, WT can not achieve fine resolutions in both time and frequency domain simultaneously because of the limitation of Heisenberg-Gabor inequality (Chui, 1992). Additionally, interference terms (or crossing terms) existing in the WT induce some spurious components in time-frequency

domain, which have little physical meaning. Hilbert-Huang Transform (HHT) is an emerging time-frequency analysis tool for nonstationary signals (Huang *et al* 1998 and 1999). HHT has already been successfully introduced to system identification and time-frequency signal processing. It has been demonstrated that the HHT has a higher resolution in time-frequency domain because of its instantaneous frequency concept, and better computational efficiency than either STFT or even WT (Chen *et al*. 2002 and Peng *et al*. 2004). A valuable research of Chen *et al.* (2002) was successfully applied HHT to analyzing dispersion of seismic surface-waves; moreover the dispersion of both group and phase velocities were obtained from the spectrum of HHT, which made good agreements with the theoretical values. Chen's study also hints that HHT may be a better processing tool to analyze the dispersion relations of elastic waves in plates than WT.

Additionally, the additional reflected waves in original wave signal collected by each sensor need to be further investigated such that the direct reflected wave package from damage could be extracted automatically. For solving the non-linear least-squares equations, the gradient method, a classical optimization approach, is used in this study. Thus, other advanced optimization methods may be introduced in the future to reduce the computational cost. Furthermore, with the development of wireless sensor networks in SHM field, the proposed least-squares method can be fused with a wireless sensor networks to achieve an active automated SHM for real aerospace structures. The current study still needs to be extended to localize multiple damages in the future.

Finally, the further experiments on WT analysis of dispersive waves and the least-squares damage localization method need to be extended to composite laminates in the future.

6 References

[1] Ashton, J. E. and Whitney, J. M., *Theory of Laminated Plates*, Stamford, Connecticut, Technomic Publishing Co., 1970.

[2] Blitz, J. and Simpson, G., *Ultrasonic Methods of Non-Destructive Testing*, Chapman and Hall, London, 1996.

[3] Birt, E. A., "Damage Detection in Carbon-fibre Composite Using Ultrasonic Lamb Waves", *Insight*, Vol. 40, pp. 335-339, 1998.

[4] Boller, C. and Biemans, C., "Structural Health Monitoring in Aircraft: State-of-the-art, Perspectives and Benefits", *The First International Workshop on Structural Health Monitoring*, Stanford University, pp. 541-522, 1977.

[5] Butterworth-Hayes, P., "Europe Seeks 7E7 Work", *Aerospace America*, American Institute for Aeronautics and Astronautics, Nov. 2003, pp. 4-6, 2003.

[6] Cawley, P., "The Rapid Non-Destructive Inspection of Large Composite Structures", *Composites*, Vol. 25, pp. 351-357, 1994.

[7] Chang, F. K., "Structural Health Monitoring, a Summary Report on the first International Workshop on Structural Health Monitoring", *The 2nd International Workshop on Structural Health Monitoring*, Stanford University, pp. xix-xxix, 1999.

[8] Chen, C. H., Li C. P., and Teng, T. L., "Surface-wave Dispersion Measurements Using Hilbert-Huang Transform", *Terrestrial, Atmospheric and Oceanic Sciences (TAO)*, Vol. 13, No. 2, pp. 171-184, 2002.

[9] Chui, C. K., *An Introduction to Wavelets*, Academic Press, San Diego, CA, 1992.

[10] Doebling, S. W., Farrar, C. R., Prime, M. B., and *et al.*, "Damage Identification and Health Monitoring of Structural and Material System from Changes in Their Vibration Characteristics: A Literature Review", Los Alamos National Laboratory Report, LA-13070-MS, 1996.

[11] Dong, S. B., Pister, K., and Taylor, R. L., "On the Theory of Laminated Anisotropic Shells and Plates", *Journal of Aerospace Science*. Vol. 29, pp. 969-975, 1962.

[12] Farrar, C. R., Baker, W. E., Bell, T. M., and *et al*., "Dynamic Characterization and damage Detection in the I-40 Bridge over the Rio Grande", Los Alamos National Laboratory report LA-12767-MS, 1994.

[13] Fedorov, F. L., *Theory of Elastic Waves in Crystals*, Plenum, New York, 1968.

[14] Gaul, L. and Hurlebaus, S., "Identification of the Impact Location on a Plate Using Wavelets", *Mechanical Systems and Signal Processing*, Vol. 12, No. 6, pp. 783-795, 1997.

[15] Giurgiutiu, V., Zagrai, A. N., and Bao, J., "Piezoelectric Wafer Embedded Active Sensors for Aging Aircraft Structural Health Monitoring", *Structural Health Monitoring*, Vol. 1, No. 1, pp. 41-46, 2002.

[16] Gorman, M. R., "Plate Wave Acoustic Emission", *Journal of Acoustical Society of America*, Vol. 90, No. 1, pp. 358-364, 1991.

[17] Graff, K. F., *Wave Motion in Elastic Solids*. Dover publications, New York, 1991

[18] Guo, N. and Cawley, P., "Lamb Wave Reflection for the Quick Non-Destructive Evaluation of Large Composite Laminates", *Materials Evaluation*, Vol. 52, pp. 404-411, 1994.

[19] Haykin, S., *Array Signal Processing*, Prentice-Hall, Englewood-Cliffs, NJ, 1985.

[20] Hodges, C. H., Power, J., and Woodhouse, J., "The Use of the Spectrogram in Structure Acoustics and an Application to the Vibrations of Cylindrical Shells", *Journal of Sound and Vibration*, Vol. 101, No. 2, pp. 203-218, 1985.

[21] Housner, G. W., Bergman, L. A., Caughey, T. K., and *et al.*, "Structural Control Past, Present, and Future," *Journal of Engineering Mechanics*, Vol. 123, No. 9, pp. 897-971, 1997.

[22] Huang, N. E., Shen, A., Long, S. R., and *et al*., "The Empirical Mode Decomposition and Hilbert Spectrum for Nonlinear and Nonstationary Time Series Analysis". *Proceedings Royal Society of London Series*, A454, pp. 903-995, 1998.

[23] Huang, N. E., Shen, A., and Long, S. R., "A New View of Nonlinear Water Waves: The Hilbert Spectrum", *Annual Review of Fluid Mechanics*, Vol. 31, pp. 417-457, 1999.

[24] Hurlebaus, S., Niethmmer, M., Jacobs, L., and Valle, C., "Automated Methodology to Locate Notches with Lamb Waves", *Acoustics Research Letters Online*, Vol. 2, No. 4, pp. 97-102, 2001.

[25] Ihn, J. B. and Chang, F. K., "Detection and Monitoring of Hidden Fatigue Crack Growth Using a Built-in Piezoelectric Sensor/Actuator Network: I Diagnostics", *Smart Materials and Structures*, Vol. 13, No. 3, pp. 609-620, 2004.

[26] Jeong, H. and Jang, Y. S., "Wavelet Analysis of Plate Wave Propagation in Composite Laminates", *Composite Structures*, Vol. 49, No. 4, pp. 443-450, 2000.

[27] Jeong, H., "Analysis of Plate Wave Propagation in Anisotropic Laminates Using a Wavelet Transform", *NDT&E International*, Vol. 34, pp. 185-190, 2001.

[28] Jones, R. M. *Mechanics of Composite Materials*, Second Edition, Taylor & Francis, Philadelphia, 1999.

[29] Kane, T. R. and Mindlin, R.D., "High-frequency Extensional Vibrations of Plates", *Journal of Applied Mechanics*, Vol. 23, pp. 277-283, 1956.

[30] Kaplan, L. M., Le, Q., and Molnár, P., "Maximum Likelihood Methods for Bearings-only Target Localization", *IEEE International Conference on Acoustics, Speech, and Signal Processing (ICASSP '2001)*, Vol. 5, pp. 3001-3004, 2001.

[31] Kehlenbach, M. and Hanselka, H., "Automated Structural Integrity Monitoring based on Broadband Lamb Wave Excitation and Matched Filtering", *The 44th AIAA/ASME/ASCE/AHS Structures, Structural Dynamics, and Materials Conference*. April 7-10, Norfolk, Virginia, 2003.

[32] Kishimoto, K., Inoue, H., Hamada, M., and Shibuya, T., "Time Frequency Analysis of Dispersive Waves by Means of Wavelet Transform". *Journal of Applied Mechanics*, Vol. 62, pp. 841-46, 1995.

[33] Krautkramer, J. and Krautkramer, H., *Ultrasonic Testing of Materials*, Springer-Verlag, Berlin, 1990.

[34] Kulkarni, S. V. and Pagano, N. J., "Dynamic Characteristics of Composite Laminates", *Journal of Sound and Vibration*, Vol. 23, No. 1, pp. 127-143, 1972.

[35] Lamb, H., "On Waves in an Elastic Plate", *Proceedings Royal Society London*, series A, Vol. 93, pp. 114-128, 1916/1917.

[36] Lannotta, B., "Safe Launches for CEV", *Aerospace America*, pp. 40-44, June, 2004.

[37] Latif, R., Aassif, E. H., Maze, G., Moudden, A., and Faiz, B., "Determination of the Group and Phase Velocities from Time-frequency Representation of Wigner-Ville", *NDT&E International*, Vol. 32, No.7, pp. 415-422, 1999.

[38] Lemistre, M. and Balageas, D., "Structural Health Monitoring System Based on Diffracted Lamb Wave Analysis by Multiresolution Processing". *Smart Materials and Structures*, Vol. 10, No. 3, pp. 504-511, 2001.

[39] Lin, X., "Structural Health Monitoring Using Geophysical Migration Technique with Built-in Piezoelectric Sensor/Actuator Arrays", Ph.D. Dissertation, North Carolina State University, Raleigh, NC, 2000.

[40] Lin, X. and Yuan, F. G., "Diagnostic Lamb Waves in an Integrated Piezoelectric Sensor/Actuator Plate: Analytical and Experimental Studies", *Smart Materials and Structures*, Vol. 10, No. 5, pp. 907-913. 2001a.

[41] Lin, X. and Yuan, F. G., "Damage Detection of a Plate Using Migration Technique", *Journal of Intelligent Material Systems and Structures*, Vol. 12, No. 3, pp. 469-482, 2001b.

[42] Liu, G. R., Tani, J., Ohyoshi, T., and Watanabe, K., "Transient Waves in Anisotropic Laminated Plates, Part1: Theory, Part2: Application", *Journal of Vibration and Acoustics*, Vol. 113, pp. 230-239, 1991.

[43] Lo, K. H., Cristensen, R. M., and Wu, E. M., "A Higher-order Theory of Plate Deformation, Part 1 and 2", *Journal of Applied Mechanics*, Vol. 44, pp. 663-676, 1977.

[44] Lord Rayleigh, "On the Free Vibration of an Infinite Plate of Homogeneous Isotropic Elastic Matter", *Proceedings London Mathematical Society*, Vol. 20, No. 357, pp. 225-234, 1888/1889.

[45] Mal, A. K. and Lih, S., "Elastodynamic Response of a Unidirectional Composite Laminate to Concentrated Surface Loads Part I, Part II", *Journal of Applied Mechanics*, Vol. 59, pp. 878-892, 1992.

[46] Mallat, S., *A wavelet Tour of Signal Processing*, Academic Press, San Diego, CA, 1998.

[47] Mindlin, R. D., "Influence of Rotary Inertia and Shear on Flexural Motions of Isotropic Elastic Plates", *Journal of Applied Mechanics*, Vol. 18, pp. 31-38, 1960.

[48] Mindlin, R. D. and Medick, M. A., "Extensional Vibrations of Elastic Plates", *Journal of Applied Mechanics*, Vol. 26, pp. 561-569, 1959.

[49] Misiti, M., Oppenheim, G., and Poggi, J. M., *Wavelet Toolbox User's Guide*, Version 2, The Math Works, Inc., 2002. http://www.mathworks.com/access/helpdesk/help/pdf_doc/wavelet/wavelet_ug.pdf

[50] Nayfeh, A. H., "The General Problem of Elastic Wave Propagation in Multilayered Anisotropic Media", *Journal of Acoustic Society of America*, Vol. 89, No. 4, pp. 1521-1531, 1991.

[51] Nayfeh, A. H. and Chimenti, D. E., "Free Wave Propagation in Plates of General Anisotropic Media", *Journal of Applied Mechanics*, Vol. 56, pp. 881-886, 1989.

[52] Musgrave, M. J. P., *Crystal Acoustics Crystal acoustics: Introduction to the Study of Elastic Waves and Vibrations in Crystals*, Holden Day, San Francisco, CA. 1970.

[53] Newland, D. E., "Harmonic Wavelet Analysis", *Proceedings Royal Society of London Series*, Series A. Vol. 443, pp. 203-225, 1993.

[54] Newland, D. E., "Practical Signal Analysis: Do Wavelet Make Any Difference?". Keynote Paper, *Proceedings of 1997 ASME Design Engineering Technical Conferences, 16th Biennial Conf. on Mechanical Vibration and Noise*, Paper DETC97/VIB-4135 (CD ROM ISBN 0 7918 1243 X), Sacramento, CA, 1997.

[55] Newland, D. E., "Time-Frequency and Time-Scale Analysis by Harmonic Wavelets", In: Prochazka, A., Uhlir, J., Rayner, P. J. W., Kingsbury, N. G., editors. *Signal Analysis and Prediction*. Boston: Birkhauser; Chapter 1, 1998.

[56] Newland, D. E., “Ridge and Phase Identification in the Frequency Analysis of Transient Signals by Harmonic Wavelets”, *Journal of Vibration and Acoustics*, Vol. 121, pp. 149-155, 1999.

[57] Önsay, T. and Haddow, A. G., “Wavelet Transform Analysis of Transient wave propagation in a Dispersive Medium”, *Journal of Acoustical Society of America*, Vol. 95, No. 3, pp. 1441-1449, 1994.

[58] Orfanidis, S. J., *Introduction to Signal Processing*, Prentice Hall, Englewood Cliffs, NJ, 1996

[59] Peng, Z. K., Tse, P. W., and Chu, F. L., “A comparison Study of Improved Hilbert-Huang Transform and Wavelet Transform: Application to Fault Diagnosis for Rolling Bearing”, *Mechanical Systems and Signal Processing*, 2004, (In Press)

[60] Quek, S. T., Wang, Q., Zhang, L., and Ong, K. H., “Practical Issues in the Detection of Damage in Beams Using Wavelets”, *Smart Materials and Structures*, Vol. 10, pp. 1009-1017, 2001.

[61] Reddy, J. N., “A Simple Higher-order Theory for Laminated Composite Plates”, *Journal of Applied Mechanics*, Vol. 51, pp. 745-752, 1961.

[62] Reed, C. W., Hudson, R., and Yao, K., “Direct Joint Source Localization and Propagation Speed Estimation”, *IEEE International Conference on Acoustics, Speech, and Signal Processing (ICASSP '1999)*, Phoenix, AZ, pp. 1169-1172, 1999.

[63] Reissner, E. and Stavsky, Y., “Bending and Stretching of Certain Types of Heterogeneous Aeolotropic Elastic Plates”, *Journal of Applied Mechanics*, Vol. 28, pp. 402-408, 1961.

[64] Rose, J. L., *Ultrasonic Waves in Solid Media*, Cambridge, New York, Cambridge University Press, 1999.

[65] Rytter, A., “Vibration Based Inspection of Civil Engineering Structures”, PhD. Dissertation, Dept. of Building Technology and Structure Eng., Aalborg University, Denmark, 1993.

[66] Sachse, W. and Pao, Y. H., "On the Determination of Phase and Group Velocities of Dispersive Waves in Solids", *Journal of Applied Physics*, Vol. 49, No. 8, pp. 4320-4327, 1978.

[67] Sato, M., "Mathematical Foundation of Wavelets", *Journal of Acoustical Society of Japan*. Vol. 47, No. 6, pp. 405-423, 1991 (in Japanese).

[68] Shannon, C. E., "Communication in the presence of noise", *Proceedings of the Institute Radio Engineers*, Vol. 37, No. 1, pp. 10-21, 1949.

[69] Sheng, X. and Hu, Y-H., "Energy Based Acoustic Source Localization", *The 2nd International Workshop on Information Processing in Sensor Networks (IPSN '03)*, April 22-23, 2003, Palo Alto, CA. pp. 285-300, 2003

[70] Sohn, H., Park, G., Wait, J. R., Limback, N. P., and Farrar, C. R., "Wavelet-based Active Sensing for Delamination Detection in Composite Structures", *Smart Materials and Structures*, Vol. 13, No. 1, pp. 153-160, 2004.

[71] Strokes, G. G., *Smith's Prize Examination*, Cambridge, 1876. [Reprinted 1905 in *Mathematics and Physics Papers*, Vol. 5, pp. 362, Cambridge University Press]

[72] Sun, C. T. and Whitney, J. M., "On Theories for the Dynamic Response of Laminated Plates", *Proceedings AIAA/ASME/SAE 13th Structures, Structural Dynamics, and Materials Conference, AIAA paper* No. 72-398, 1972.

[73] Suzuki, H., Kinko, T., Hayashi, Y., Takemoto, M. and Ono, K., "Wavelet Transform of Acoustic Emission Signals", *Journal of Acoustic Emission*, Vol. 14, No. 2, pp. 69-82, 1996.

[74] Synge, J. L., "Elastic Waves in Anisotropic Media", *Journal of Mathematical Physics*, Vol. 25, pp. 323-334, 1957.

[75] Taff, L. G., "Target Localization from Bearing-only Observations", *IEEE Transaction on Aerospace and Electronic Systems*, Vol. 3, No. 1, pp. 2-10, 1997.

[76] Tan, K. S., Guo, N., Wong, B. S., and Tui, C. G., "Experimental Evaluation of Delaminations in Composite Plates by the Use of Lamb Waves", *Composite Science and Technology*, Vol. 53, No. 1, pp. 77-84, 1995.

[77] Tang, B., Henneke II, E. G., and Stiffler, R. C., “Low Frequency Flexural Wave Propagation in Laminated Composite Plates”, *Acoustic-Ultrasonic Theory and Application*, Ed by John, C. Duke, Jr. Plenum Press, New York, 1988.

[78] Thomas, G., “Overview of Nondestructive Evaluation Techniques” *Proceedings of SPIE on Nondestructive Evaluation of Aging Aircraft, Airports, Aerospace Hardware, and Materials*, Oakland, CA, Vol. 2455, pp. 5-9, 1995

[79] Tobias, A., “Acoustic-emission Source Location in Two Dimensions by an Array of Three Sensors”, *Non-Destructive Testing*, Vol. 9, No. 1, pp. 9-12, 1976

[80] Tsai, S. W. and Pagano, N. J., “Invariant Properties of Composite Materials”, *Composite Materials Workshop* (edited by Tsai, S. W., Halpin, J. C., and Pagano, N. J.), Stamford, Connecticut, Technomic Publishing Co., 1968.

[81] Vetterli, M. and Kovacevic, J., *Wavelets and Subband Coding*. Upper Saddle River, NJ, Prentice-Hall, pp. 311-312, 1995.

[82] Viktorov, I. A., *Rayleigh and Lamb Waves, Physical Theory and Applications*, Plenum Press, New York, 1967.

[83] Wang, C. S., Wu, F., and Chang, F. K., “Structural Health Monitoring for Fiber-Reinforced Composites to Steel-reinforced Concrete”, *Smart Materials and Structures*, Vol. 10, No. 3, pp. 548-522, 2001.

[84] Wang, L. and Yuan, F. G., "Imaging of Multiple Damages in a Composite Plate by Prestack Reverse-Time Migration Technique", *Proceedings of the 4th International Workshop on Structural Health Monitoring*, Stanford, CA. Sep 15-17, 2003.

[85] Washizu, K., *Variational Methods in Elasticity and Plasticity*, third edition, Pergamon Press, Oxford, 1982.

[86] Whitney, J. M. and Pagano, N. J., “Shear Deformation in Heterogeneous Anisotropic Plates”, *Journal of Applied Mechanics*, Vol. 37, pp. 1031-1036, 1970.

[87] Whitney, J. M. and Sun, C. T., “A Higher Order Theory for Extensional Motion of Laminated Composites”, *Journal of Sound and Vibration*, Vol. 30, No. 1, pp. 85-97, 1973.

[88] Wilcox, P., Lowe, M., and Cawley, P., "The Effect of Dispersion on Long-range Inspection Using Ultrasonic Guided Waves", *NDT&E International*, Vol. 34, pp. 1-9, 2001.

[89] Wu, T. T. and Chen, Y. C., "Dispersion of Laser Generated Surface Waves in an Epoxy-Bonded Layered Medium", *Ultrasonics*, Vol. 34, pp.793-799, 1996.

[90] Yang, S. and Yuan, F. G. Private Communication, 2004.

[91] Yao, K., Hudson, R. E., Reed, C. W., Chen, D., and Lorenzelli, F., "Blind Beam Forming on a Randomly Distributed Sensor Array System", *IEEE Journal Selected Areas in Communications*, Vol. 16, pp. 1555-1567, 1998.

[92] Yuan, F. G., *Lecture on Anisotropic Elasticity Application to Composite Fracture Mechanics*, North Carolina State University, NC, 1998.
www.mae.ncsu.edu/faculty/yuan/Aniso.pdf

[93] Yuan, F. G. and Hsieh, C. C., "Three-dimensional Wave Propagation in Composite Cylindrical Shells", *Composite Structures*, Vol.42, No. 2, pp. 153-167, 1998.

Appendix

A.1 Elastic Coefficients C_{ij} Calculated from C'_{ij} by Coordinate Transformations

Let (x, y, z) denote the global coordinate system and (x', y', z') be the principal material coordinate system. Fiber orientation ϑ may be considered as an angle of rotation from (x, y) axes to (x', y') axes about z-axis in the counter-clockwise direction, which is the positive angular direction, as shown in Figure A.1.

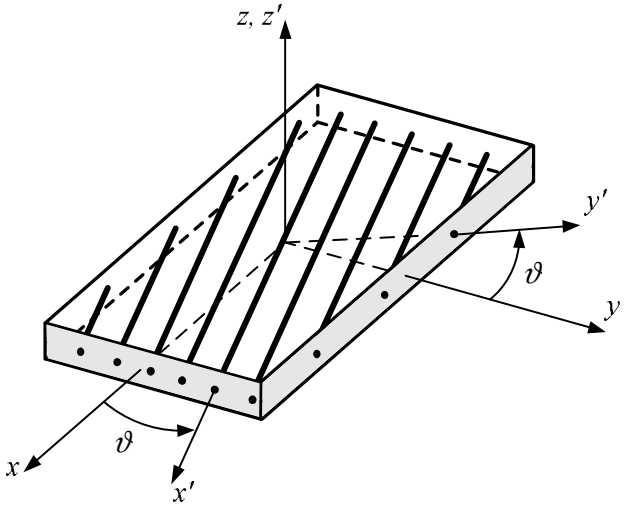

Figure A.1 An arbitrarily oriented lamina with global and principal material coordinate systems

The stress components are often written in contracted notation of $\boldsymbol{\sigma} = \{\sigma_{11},\ \sigma_{22},\ \sigma_{33},\ \sigma_{23},\ \sigma_{13},\ \sigma_{12}\}^T$ and $\boldsymbol{\sigma}' = \{\sigma'_{11},\ \sigma'_{22},\ \sigma'_{33},\ \sigma'_{23},\ \sigma'_{13},\ \sigma'_{12}\}^T$ in a column form. The transformation between $\boldsymbol{\sigma}$ and $\boldsymbol{\sigma}'$ is given by (Yuan, 1998)

$$\boldsymbol{\sigma}' = \mathbf{Q}(\vartheta)\boldsymbol{\sigma} \tag{A.1-1}$$

where

$$\mathbf{Q}(\vartheta)=\begin{bmatrix} \cos^2\vartheta & \sin^2\vartheta & 0 & 0 & 0 & 2\cos\vartheta\sin\vartheta \\ \sin^2\vartheta & \cos^2\vartheta & 0 & 0 & 0 & -2\cos\vartheta\sin\vartheta \\ 0 & 0 & 1 & 0 & 0 & 0 \\ 0 & 0 & 0 & \cos\vartheta & -\sin\vartheta & 0 \\ 0 & 0 & 0 & \sin\vartheta & \cos\vartheta & 0 \\ -\cos\vartheta\sin\vartheta & \cos\vartheta\sin\vartheta & 0 & 0 & 0 & \cos^2\vartheta-\sin^2\vartheta \end{bmatrix} \tag{A.1-2}$$

Note that the transformation matrix has the following property:

$$\mathbf{Q}^{-1}(\vartheta)=\mathbf{Q}(-\vartheta) \tag{A.1-3}$$

From the global coordinate system (x, y, z) to the principal material coordinate system (x', y', z'), the transformation relation is

$$C'_{ij}=\mathbf{Q}(\vartheta)C_{ij}\mathbf{Q}^T(\vartheta) \tag{A.1-4}$$

Since the aim is to obtain the stiffness constant C_{ij} in the global coordinate system from the known stiffness constant C'_{ij} derived from principal material coordinate system, with Eq. (A.1-3) the transformation relation from the principal material coordinate system (x', y', z') to the global coordinate system (x, y, z) can be expressed as

$$C_{ij}=\mathbf{Q}(-\vartheta)C'_{ij}\mathbf{Q}^T(-\vartheta) \tag{A.1-5}$$

where material elastic coefficients C'_{ij} of a lamina are obtained from the material properties E_i, ν_{ij}, and G_{ij} by using the formulas in Appendix A.2.

The elastic coefficients C'_{ij} in the stress-strain relations for the composite material with respect to the global coordinate system are given by:

$$\begin{Bmatrix}\sigma_x\\ \sigma_y\\ \sigma_z\\ \tau_{yz}\\ \tau_{xz}\\ \tau_{xy}\end{Bmatrix}=\begin{bmatrix}C_{11} & C_{12} & C_{13} & 0 & 0 & C_{16}\\ C_{12} & C_{22} & C_{23} & 0 & 0 & C_{26}\\ C_{13} & C_{23} & C_{33} & 0 & 0 & C_{36}\\ 0 & 0 & 0 & C_{44} & C_{45} & 0\\ 0 & 0 & 0 & C_{45} & C_{55} & 0\\ C_{16} & C_{26} & C_{36} & 0 & 0 & C_{66}\end{bmatrix}\begin{Bmatrix}\varepsilon_x\\ \varepsilon_y\\ \varepsilon_z\\ \gamma_{yz}\\ \gamma_{xz}\\ \gamma_{xy}\end{Bmatrix} \tag{A.1-6}$$

A.2 Elastic Coefficients C'_{ij} in the Principal Material Coordinate System

The stress-stain relations for an orthotropic material in the principal material coordinate system take the form

$$\begin{Bmatrix}\sigma_1\\ \sigma_2\\ \sigma_3\\ \tau_{23}\\ \tau_{13}\\ \tau_{12}\end{Bmatrix}=\begin{bmatrix}C'_{11} & C'_{12} & C'_{13} & 0 & 0 & 0\\ C'_{12} & C'_{22} & C'_{23} & 0 & 0 & 0\\ C'_{13} & C'_{23} & C'_{33} & 0 & 0 & 0\\ 0 & 0 & 0 & C'_{44} & 0 & 0\\ 0 & 0 & 0 & 0 & C'_{55} & 0\\ 0 & 0 & 0 & 0 & 0 & C'_{66}\end{bmatrix}\begin{Bmatrix}\varepsilon_1\\ \varepsilon_2\\ \varepsilon_3\\ \gamma_{23}\\ \gamma_{13}\\ \gamma_{12}\end{Bmatrix} \tag{A.2-1}$$

The elastic coefficients C'_{ij} in Eq. (A.2-1) are related to the engineering constants, E_i, ν_{ij}, and G_{ij} by (Jones, 1999)

$$C'_{11}=\frac{1-\nu_{23}\nu_{32}}{E_2E_3\Delta},\qquad C'_{12}=\frac{\nu_{21}+\nu_{31}\nu_{23}}{E_2E_3\Delta}=\frac{\nu_{12}+\nu_{32}\nu_{13}}{E_1E_3\Delta},$$

$$C'_{13}=\frac{\nu_{31}+\nu_{21}\nu_{32}}{E_2E_3\Delta}=\frac{\nu_{13}+\nu_{12}\nu_{23}}{E_1E_2\Delta},\qquad C'_{22}=\frac{1-\nu_{13}\nu_{31}}{E_1E_3\Delta},$$

$$C'_{23}=\frac{\nu_{32}+\nu_{12}\nu_{31}}{E_1E_3\Delta}=E_3\frac{\nu_{23}+\nu_{21}\nu_{13}}{E_1E_2\Delta},\qquad C'_{33}=\frac{1-\nu_{12}\nu_{21}}{E_1E_2\Delta},$$

$$C'_{44}=G_{23},\qquad C'_{55}=G_{13},\qquad C'_{66}=G_{12},$$

and $\Delta = \dfrac{1-\nu_{12}\nu_{21}-\nu_{23}\nu_{32}-\nu_{31}\nu_{13}-2\nu_{21}\nu_{32}\nu_{13}}{E_1E_2E_3}$

where the subscripts 1, 2, and 3 refer to the longitudinal, transverse, and through-thickness directions, respectively; E_1, E_2, E_3 are Young's moduli in 1, 2 and 3 directions, respectively; ν_{ij} is Poisson's ratio defined as ratio of transverse strain in the *j*th direction to the axial strain in the *i*th direction, when stressed in the *i*-direction, $-\varepsilon_j/\varepsilon_i$; G_{23}, G_{13}, G_{12} are the shear moduli in the 2-3, 1-3, and 1-2 planes respectively. In addition, the following reciprocal relation holds among the principal moduli E_i and Poisson's ratios ν_{ij}:

$$\frac{\nu_{ij}}{E_i} = \frac{\nu_{ji}}{E_j}, \qquad (i, j = 1, 2, 3) \tag{A.2-2}$$

A.3 Matlab Script Files: gabor.m and gabinfo.m

File Name: gabor.m

Save Location: "\MATLAB6p5\toolbox\wavelet\wavelet\" and current work directory

```
function [out1,out2] = gabor(varargin)
%GABOR Gabor complex wavelet.
%   [PSI,X] = GABOR(LB,UB,N) returns values of
%   the Gabor wavelet on a N points regular grid
%   on the interval [LB,UB].
%   Output arguments are the wavelet function PSI
%   computed on the grid X.
%
%   This wavelet has [-4 4] as effective support.
%
%   See also WAVEINFO GABINFO.

%   Lei Wang, 8-Aug-2002.     Last Revision: 23-Mar-2003.
%   Dept. Mechanical & Aerospace Engineering, NC State University.
%   Copyright 2003. Lei Wang <WangLeiBox@hotmail.com>
```

```
%   $Revision: 1.0 $  $Date: Mar.23,2003 10:10:20 $

% Check arguments.
if errargn(mfilename,nargin,[3 4],nargout,[0:2]), error('*'); end

% Compute values of the Gabor wavelet.
out2 = linspace(varargin{1:3});        % wavelet support.
w0 = 2*pi; r = pi*sqrt(2/log(2));
out1 = sqrt(w0/(r*sqrt(pi)))*exp(-(out2.^2)/2*(w0/r)^2).*exp(j*w0*out2);
```

File Name: gabinfo.m

Save Location: "\MATLAB6p5\toolbox\wavelet\wavelet\" and current work directory

```
function gabinfo
%GABINFO Information on Gabor Complex wavelet.
%
%   Gabor Complex Wavelet
%
%   Definition:
%   gab(x) = sqrt(w0/(r*sqrt(pi)))*exp(-x^2/2*(w0/r)^2) * exp(j*w0*x)
%   where: r = pi*sqrt(2/log(2))=5.336 In Matlab, log() indicates ln()
%          w0 = 2*pi
%
%   Family                  Gabor
%   Short name              gab
%
%   Orthogonal              no
%   Biorthogonal            no
%   Compact support         no
%   DWT                     no
%   CWT                     possible
%
%   Support width           infinite
%   Effective support       [-4 4]
%
%   Reference: Vetterli M. Kovacevic J,
%   Wavelets and Subband Coding.
%   Upper Saddle River, NJ: Prentice-Hall, 1995, pp. 311-312.

%   Lei Wang, 8-Aug-2002.     Last Revision: 23-Mar-2003.
%   Dept. Mechanical & Aerospace Engineering, NC State University.
%   Copyright 2003. Lei Wang <WangLeiBox@hotmail.com>
%   $Revision: 1.0 $  $Date: Mar.23,2003 10:09:56 $
```

A.4 Bandwidth of a Signal

There are several ways in which bandwidth can be defined, but two common approaches are often used to evaluate the bandwidth of a signal. One is 3-dB bandwidth which is widely used in signal processing; the other is based on the standard deviation that is usually used in mathematics since it can give the bandwidth from the analytical spectrum expression of the signal.

A.4.1 3-dB bandwidth

3-dB bandwidth may be the simplest definition and it is suitable for the signal without the need of analytical spectrum expression. If $\hat{s}_{\max}$ is the maximum amplitude of the frequency spectrum of a signal $\hat{s}(\omega)$, and considering the power is proportional to the square of amplitude, the amplitude at which the power of the signal is half that of the peak is given by (Orfanidis, 1996)

$$\hat{s}^2_{half-power} = \hat{s}^2_{\max} / 2 \tag{A.4-1}$$

where $\hat{s}^2_{\max}$ is the maximum power of the signal and $\hat{s}^2_{half-power}$ is half of the maximum power. In dB, this condition reads

$$20\log(\frac{\hat{s}_{half-power}}{\hat{s}_{\max}}) = 10\log(1/2) = -3\,\text{dB} \tag{A.4-2}$$

Therefore, the amplitude associated with the half-power points of a signal is 3dB below the maximum value. On a linear scale of amplitude, the amplitude at a half-power point is given by

$$\hat{s}_{half-power} = \frac{\sqrt{2}}{2}\hat{s}_{\max} \approx 0.707\hat{s}_{\max} \tag{A.4-3}$$

Therefore 3-dB bandwidth $\Delta\hat{s}$ is the frequency bandwidth between the half-power points of the spectrum.

Consider the Gabor function Eq. (3.2-2) and the relation Eq. (A.4-3), the following equation can be obtained

$$\exp[-\frac{(\gamma/\omega_0)^2}{2}(\omega-\omega_0)^2]=\frac{\sqrt{2}}{2} \tag{A.4-4}$$

Solving Eq. (A.4-4), the frequency coordinates of two half-power points are

$$\omega_{half-power}=\omega_0\pm\frac{\omega_0}{\gamma}\sqrt{\ln\sqrt{2}} \tag{A.4-5}$$

Thus the 3-dB bandwidth of the Gabor function is

$$\Delta\hat{\psi}_g(\omega)=2\frac{\omega_0}{\gamma}\sqrt{\ln\sqrt{2}} \tag{A.4-6}$$

Especially, if $\gamma=\pi\sqrt{2/\ln 2}$ and $\omega_0=2\pi$, then $\Delta\hat{\psi}_g(\omega)=1.3863$.

Figure A.2 shows the parameters associated with 3-dB bandwidth of Gabor function.

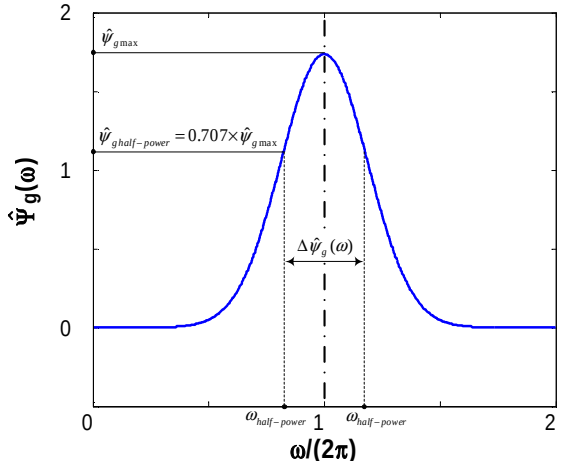

Figure A.2 Illustration of 3-dB bandwidth of Gabor function $\Delta\hat{\psi}_g(\omega)=1.3863$

A.4.2 Standard deviation bandwidth

If the analytical spectrum expression of signal $s(t)$ is known, say $\hat{s}(\omega)$, its frequency bandwidth $\Delta\hat{s}$ can be also derived from the standard deviation of $\hat{s}(\omega)$ (Mallat, 1998).

$$\sigma_{\hat{s}}^2 = \frac{1}{2\pi\|s(t)\|^2}\int_{-\infty}^{+\infty}(\omega-\omega_c)^2\left|\hat{s}(\omega)\right|^2 d\omega \tag{A.4-7}$$

where $\hat{s}(\omega)$ is the Fourier transform of the signal, ω_c is the central frequency of the function $\hat{s}(\omega)$. Then bandwidth is defined as

$$\Delta\hat{s} = \sigma_{\hat{s}} \tag{A.4-8}$$

For the Gabor function, since $\|\psi_g(t)\| = 1$, $\left|\hat{\psi}_g(\omega)\right| = \hat{\psi}_g(\omega)$, and its central frequency equals to ω_0, Eq. (A.4-7) can be rewritten as

$$\begin{aligned}\sigma_{\hat{\psi}_g(\omega)}^2 &= \frac{1}{2\pi}\int_{-\infty}^{+\infty}(\omega-\omega_0)^2\frac{2\pi}{\sqrt{\pi}}\frac{\gamma}{\omega_0}\exp[-(\frac{\gamma}{\omega_0})^2(\omega-\omega_0)^2]d\omega \\ &= \frac{1}{\sqrt{\pi}}\frac{\gamma}{\omega_0}\int_{-\infty}^{+\infty}(\omega-\omega_0)^2\exp[-(\frac{\gamma}{\omega_0})^2(\omega-\omega_0)^2]d\omega\end{aligned} \tag{A.4-9}$$

Considering the following known integral

$$\int_{-\infty}^{+\infty}x^2e^{-(px)^2}dx = \frac{1}{2}\frac{\mathrm{sgn}(p)}{p^2}\sqrt{p\pi} \tag{A.4-10}$$

where p is a real constant. Then, Eq. (A.4-9) can be simplified as

$$\sigma_{\hat{\psi}_g(\omega)}^2 = \frac{1}{2}\sqrt{\gamma\omega_0} = \frac{\sqrt{\omega_0\pi}}{\sqrt[4]{8\ln 2}} \tag{A.4-11}$$

Thus the corresponding bandwidth of Gabor function is

$$\Delta\hat{\psi}_g(\omega) = \sigma_{\hat{\psi}_g(\omega)} = \frac{\sqrt[4]{\omega_0\pi}}{\sqrt[8]{8\ln 2}} \tag{A.4-12}$$

Especially, if $\omega_0 = 2\pi$, then $\Delta\hat{\psi}_g(\omega) = 1.7015$.

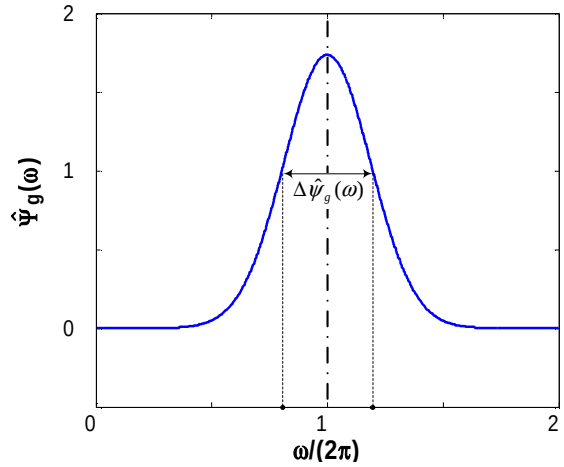

Figure A.3 Illustration of standard deviation bandwidth of Gabor function $\Delta\hat{\psi}_g(\omega) = 1.7015$

A.5 Derivation of Eq. (3.4-10) from Eq. (3.4-9)

Eq. (3.4-9) can be rearranged as

$$\mathrm{WT}_w(a,b) = \frac{\sqrt{a}}{2\pi}\int_{-\infty}^{+\infty}\hat{F}(\omega)\hat{\psi}_g(a\omega)\exp[i(\omega b - kx)]d\omega \qquad \text{(A.5-1)}$$

where $\hat{\psi}_g(a\omega)$ is a real-valued Gaussian function given by

$$\hat{\psi}_g(a\omega) = \frac{\sqrt{2\pi}}{\sqrt[4]{\pi}}\sqrt{\frac{\gamma}{\omega_0}}\exp[-\frac{(\gamma/\omega_0)^2}{2}(a\omega-\omega_0)^2]$$

Central frequency and bandwidth of $\hat{\psi}_g(a\omega)$ are given by $\omega_c = \omega_0/a$ and $\Delta\hat{\psi}_g(a\omega) = \Delta\hat{\psi}_g(\omega)/a$, where ω_0 and $\Delta\hat{\psi}_g(\omega)$ are the central frequency and standard deviation bandwidth of the Gabor function $\hat{\psi}_g(\omega)$ defined in Appendix A.4.2, respectively. Thus $\hat{\psi}_g(a\omega)$ may be considered as a band-pass filter and its central frequency is at ω_c.

In the following, a function is defined as

$$\varphi(\omega) = i(\omega b - kx) \qquad \text{(A.5-2)}$$

Functions $\varphi(\omega)$ and $\hat{F}(\omega)$ in Eq. (A.5-1) can be expanded at the central frequency $\omega = \omega_c$ of $\hat{\psi}_g(a\omega)$ by using a first-order Taylor expansion in the vicinity of $\omega_c = \omega_0 / a$.

$$\begin{aligned}\varphi(\omega) &\approx \varphi(\omega_c) + \varphi'(\omega_c)(\omega - \omega_c) \\ &= i\omega_c b - ikx + i(b - k'x)(\omega - \omega_c) \\ &= ix(k'\omega_c - k) + i(b - k'x)\omega \end{aligned} \tag{A.5-3}$$

where $k'(\omega_c) = dk(\omega_c)/d\omega$.

Similarly,

$$\hat{F}(\omega) \approx \hat{F}(\omega_c) + \hat{F}'(\omega_c)(\omega - \omega_c) = \hat{F}(\omega_c) - \omega_c \hat{F}'(\omega_c) + \hat{F}'(\omega_c)\omega \tag{A.5-4}$$

where $\hat{F}'(\omega_c) = d\hat{F}'(\omega_c)/d\omega$

Letting $c_1 = ix(k'\omega_c - k)$ and $c_2 = \hat{F}(\omega_c) - \omega_c \hat{F}'(\omega_c)$, Eq. (A.5-1) becomes

$$\mathrm{WT}_w(a,b) = \frac{\sqrt{a}}{2\pi} \int_{-\infty}^{+\infty} [c_2 + \hat{F}'(\omega_c)\omega] \hat{\psi}_g(a\omega) \exp[c_1 + i(b - k'x)\omega] d\omega \tag{A.5-5}$$

The integration above can be conveniently evaluated as a sum of the two terms, I_1 and I_2 by splitting the term in the first square bracket in the integrand into two parts. In addition, since both c_1 and c_2 are not functions of ω, they can be placed outside of the integration. Starting from the first term I_1,

$$\begin{aligned} I_1 &= \frac{\sqrt{a}}{2\pi} \int_{-\infty}^{+\infty} c_2 \hat{\psi}_g(a\omega) \exp[c_1 + i(b - k'x)\omega] d\omega \\ &= \frac{c_2\sqrt{a}}{2\pi} \exp(c_1) \int_{-\infty}^{+\infty} \hat{\psi}_g(a\omega) \exp[i(b - k'x)\omega] d\omega \end{aligned}$$

$$= \frac{c_2\sqrt{a}}{2\pi}\exp(c_1)\int_{-\infty}^{+\infty}\hat{\psi}_g(a\omega)\exp(ia\omega\frac{b-k'x}{a})\frac{d(a\omega)}{a} \tag{A.5-6}$$

Using the inverse Fourier transform $\int_{-\infty}^{+\infty}\hat{\psi}_g(\xi)\exp(it\xi)d\xi = \psi_g(t)$, the equation above can be simplified as

$$I_1 = \frac{c_2}{2\sqrt{a}\pi}\psi_g(\frac{b-k'x}{a})\exp(c_1) \tag{A.5-7}$$

Plugging c_1 and c_2 into the equation above leads to

$$I_1 = \frac{\hat{F}(\omega_c)-\omega_c\hat{F}'(\omega_c)}{2\sqrt{a}\pi}\psi_g(\frac{b-k'x}{a})\exp[ix(k'\omega_c - k)] \tag{A.5-8}$$

Following a similar approach, the second term of the integration, I_2, is

$$I_2 = \frac{\sqrt{a}}{2\pi}\exp(c_1)\hat{F}'(\omega_c)\int_{-\infty}^{+\infty}\omega\hat{\psi}_g(a\omega)\exp[i(b-k'x)\omega]d\omega$$

$$= \frac{\hat{F}'(\omega_c)\sqrt{a}}{2a^2\pi i}\exp(c_1)\int_{-\infty}^{+\infty}i(a\omega)\hat{\psi}_g(a\omega)\exp[ia\omega\frac{b-k'x}{a}]d(a\omega) \tag{A.5-9}$$

Knowing the inverse Fourier transform relationship $\int_{-\infty}^{+\infty}i\xi\hat{\psi}_g(\xi)\exp(it\xi)d\xi = \psi_g'(t)$, we have

$$I_2 = \frac{\hat{F}'(\omega_c)\sqrt{a}}{2a^2\pi}\psi_g'(\frac{b-k'x}{a})\exp[\,i(k'\omega_c x - kx - \pi/2)] \tag{A.5-10}$$

In summery, the first-order Taylor series expansion of the Eq. (A.5-1) leads to the resulting form of Eq. (3.4-10) given by

$$\begin{aligned}\mathrm{WT}_w(a,b) = {} & \frac{\hat{F}(\omega_c)-\omega_c\hat{F}'(\omega_c)}{2\sqrt{a}\pi}\exp[(i(k'x\omega_c - kx)]\psi_g(\frac{b-k'x}{a}) \\ & + \frac{\sqrt{a}\hat{F}'(\omega_c)}{2a^2\pi}\exp[i(k'x\omega_c - kx - \pi/2)]\psi_g'(\frac{b-k'x}{a})\end{aligned} \tag{A.5-11}$$

A.6 Source Localization using Triangulation Method

In this Appendix, a triangulation method for passive source localization is introduced from time differences of arrival (TDOA's) between pairs of sensors and sensor locations. In isotropic plates, closed-form solutions can be given when the number of TDOA measurements is equal to the number of unknowns (r and θ). However, for anisotropic plates where the group velocity is dependent on the wave propagation direction, an iterative algorithm needs to be developed to identify the source location.

A.6.1 Isotropic plates

To uniquely locate the impact source in a plate, measurements from three sensors must be used. Tobias (1976) formulated the problem by identifying the source location as three intersecting circles, each centered at a sensor, with their radii determined by the time of propagation of the wave emitted from the source to the respective sensor. Without loss of generality, sensor S_0 is taken at the origin of the coordinate. Two other sensors S_1 and S_2 are located at (x_1, y_1) and (x_2, y_2) respectively. By solving the three resulting equations simultaneously, closed-form solutions for the source location can be expressed by the radius r, measured from a sensor located at a reference origin, and the angle θ measured counter-clockwise from the x-axis. Figure A.4 shows a source location relative to the three sensors.

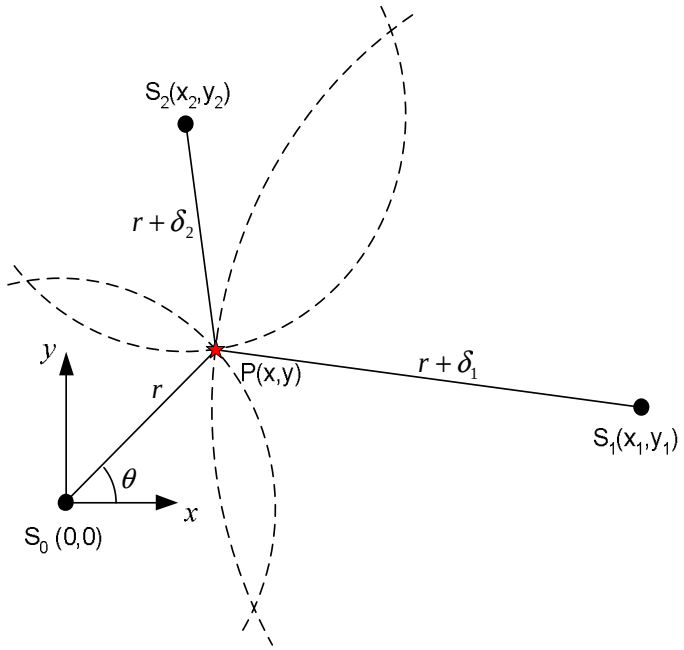

Figure A.4 Source localization by triangulation method for an isotropic plate

The impact source at P(x, y) is located at the point of intersection of the circles about S_0, S_1, and S_2 as centers with radii r, $r+\delta_1$, and $r+\delta_2$ respectively.

The equations of the three circles are written respectively as:

$$x^2 + y^2 = r^2 \tag{A.6-1a}$$

$$(x - x_1)^2 + (y - y_1)^2 = (r + \delta_1)^2 \tag{A.6-1b}$$

$$(x - x_2)^2 + (y - y_2)^2 = (r + \delta_2)^2 \tag{A.6-1c}$$

Substituting the first equation into the last two equations leads to

$$2xx_1 + 2yy_1 + 2r\delta_1 = (x_1^2 + y_1^2 - \delta_1^2) \tag{A.6-2a}$$

$$2xx_2 + 2yy_2 + 2r\delta_2 = (x_1^2 + y_2^2 - \delta_2^2) \tag{A.6-2b}$$

Changing the variables x and y in the polar coordinates in the above equation gives

$$2r(x_1 \cos\theta + y_1 \sin\theta + \delta_1) = A_1 \tag{A.6-3a}$$

$$2r(x_2\cos\theta + y_2\sin\theta + \delta_2) = A_2 \tag{A.6-3b}$$

where $A_1 = x_1^2 + y_1^2 - \delta_1^2$ and $A_2 = x_2^2 + y_2^2 - \delta_2^2$. Note that if the source location does not coincide with the reference sensor location, A_1 and A_2 are not equal to zero. Then from Eq. (A.6-3) $x_1\cos\theta + y_1\sin\theta + \delta_1 \neq 0$ and $x_2\cos\theta + y_2\sin\theta + \delta_2 \neq 0$.

δ_1 and δ_2 contained in Eq. (A.6-3) and A_1 and A_2 can be calculated from

$$\delta_1 = \Delta t_1 c_g \text{ and } \delta_2 = \Delta t_2 c_g \tag{A.6-4}$$

where c_g is the group velocity and Δt_1 and Δt_2 are the time differences of arrival (TDOA's) at sensor pairs S_0, S_1 and S_0, S_2 respectively.

For $x_1\cos\theta + y_1\sin\theta + \delta_1 \neq 0$ and $x_2\cos\theta + y_2\sin\theta + \delta_2 \neq 0$, the radius r can be determined by

$$r = \frac{A_1}{2(x_1\cos\theta + y_1\sin\theta + \delta_1)} = \frac{A_2}{2(x_2\cos\theta + y_2\sin\theta + \delta_2)} \tag{A.6-5}$$

Using Eq. (A.6-5) the following identify can be deduced:

$$(A_1x_2 - A_2x_1)\cos\theta + (A_1y_2 - A_2y_1)\sin\theta = A_2\delta_1 - A_1\delta_2 \tag{A.6-6}$$

Dividing the term $B = [(A_1x_2 - A_2x_1)^2 + (A_1y_2 - A_2y_1)^2]^{1/2}$ on both sides of Eq. (A.6-6) and defining

$$K = \frac{A_2\delta_1 - A_1\delta_2}{B} \tag{A.6-7}$$

the angle θ can be solved by the following equation

$$\cos(\theta - \phi) = K \tag{A.6-8}$$

where $\tan\phi = \dfrac{A_1y_2 - A_2y_1}{A_1x_2 - A_2x_1}$.

Since the numerator and denominator of $\tan\phi$, parameters B and K can be determined from the known positions of the two sensors S_1 and S_2, the time differences of arrival Δt_1 and Δt_2, and group velocity c_g, the angle can be determined first by

$$\theta = \phi + \cos^{-1} K \tag{A.6-9}$$

Using Eq. (A.6-5) with Eq. (A.6-9) the radius r can be then determined. Then the single damage can be localized by knowing the two unknowns r and θ.

A.6.2 Summary of the triangulation method (Tobias, 1976)

- The method is not an active detection technique but a passive sensing method, unsuitable for structural health monitoring;
- Three sensors can be placed in arbitrary triangle;
- The method is only suitable for isotropic plates due to the assumption of constant group velocity c_g;
- The method can localize the source outside of the triangular area;
- Two unknowns (r,θ) are the source location in polar coordinates. Knowing (r,θ), the source location in the Cartesian coordinates can be simply obtained by $x = r\cos\theta$ and $y = r\sin\theta$;
- The following parameters are given for locating the impact source:
    - Geometry parameters: the Cartesian coordinates of three sensors $S_0\,(0,0)$, $S_1\,(x_1, y_1)$, and $S_2\,(x_2, y_2)$;
    - Measured parameters: Δt_1 and Δt_2 are the time differences of arrival (TDOA's) at the sensor pairs S_0, S_1 and S_0, S_2 respectively;
    - Constant group velocity: c_g;

In majority of the cases, the solution for the source location (r,θ) is unique. However, in few exceptional cases, there exist two physical solutions for (r,θ). Such solutions are so-called ambiguous solutions (Tobias, 1976). In order to resolve the ambiguous solutions it is necessary to use a fourth sensor S_3, located at the point (x_3, y_3).

A general procedure of locating the impact source can be taken by the following steps:

1. Calculate ϕ first by knowing Δt_1 and Δt_2 and sensor locations;
2. Compute the unknown θ by Eq. (A.6-9). Note that since θ has two solutions over the range $(-\pi,\pi)$ where two solutions of θ are obtained;
3. Use the two values of θ to calculate the unknown radius r with Eq. (A.6-5). Neglect the inadmissible angle θ if the corresponding $r<0$. Then obtain the unique solution for the source location (r,θ);
4. Transfer (r,θ) to Cartesian coordinate system $x=r\cos\theta$ and $y=r\sin\theta$.

A.6.3 Anisotropic plates

Since the group velocity of wave propagating in an anisotropic plate is not constant but depends on the propagation direction, the proposed method in the above section is not valid for anisotropic plates. For a planar source location, three sensors must be used. Analysis of arrival times at different sensors enables the emission source to be located by means of a triangulation method. A pair of differences in the arrival time from an array of three sensors defines two hyperbolae at which point of intersection the emission source is located. For isotropic materials, a closed form solution has been derived (Tobias, 1976). In anisotropic materials, the source location determination becomes more complicated since the group velocity is function of direction of propagation in the plate.

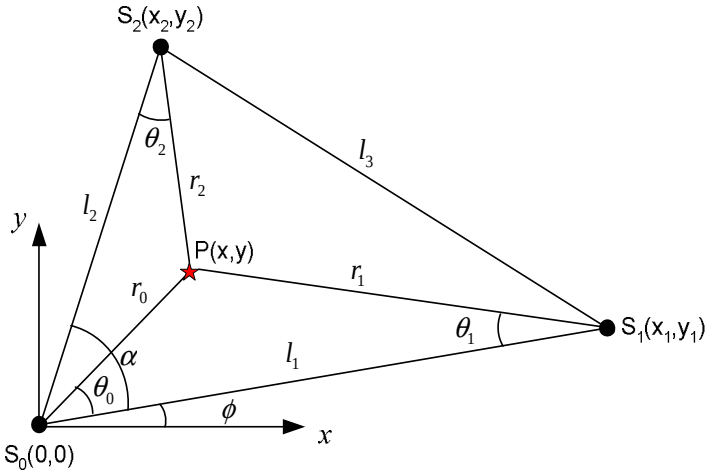

Figure A.5 Source localization analysis for an anisotropic plate

Figure A.5 shows three sensors S_0, S_1, and S_2 and the location of a source $P(x, y)$ relative to the sensors. Three wave propagating directions from the impact source are as follows: PS_0 (direction: $\theta_0 + \pi + \phi$), PS_1 (direction: $2\pi - \theta_1 + \phi$), and PS_2 (direction: $\theta_2 + \alpha + \phi$). Since the group velocity of wave is function of both propagation direction and frequency f, three group velocities may be expressed as:

$$c_{g0} = c_g(\theta_0 + \pi + \phi, f) \tag{A.6-10a}$$

$$c_{g1} = c_g(2\pi - \theta_1 + \phi, f) \tag{A.6-10b}$$

$$c_{g2} = c_g(\theta_2 + \alpha + \phi, f) \tag{A.6-10c}$$

Sensors S_0 and S_1 are considered first. The time difference of arrival (TDOA) at the sensor pair S_0, S_1 is

$$\Delta t_1 = t_1 - t_0 = \frac{r_1}{c_{g1}} - \frac{r_0}{c_{g0}} \tag{A.6-11}$$

From geometric considerations, the unknown distances r_1 and r_0 can be written in terms of the unknown angles and the known distance between S_1 and S_0.

From sine law, we have the following relation in the triangle PS_0S_1

$$\frac{\sin\theta_0}{r_1} = \frac{\sin\theta_1}{r_0} = \frac{\sin(\theta_0+\theta_1)}{l_1} \tag{A.6-12}$$

Then the distances r_0 and r_1 can be expressed as

$$\begin{cases} r_0 = \dfrac{l_1 \sin\theta_1}{\sin(\theta_0+\theta_1)} \\ r_1 = \dfrac{l_1 \sin\theta_0}{\sin(\theta_0+\theta_1)} \end{cases} \tag{A.6-13}$$

Plugging Eq. (A.6-13) back into Eq. (A.6-11) gives

$$\frac{l_1 \sin\theta_0}{c_{g1}\sin(\theta_0+\theta_1)} - \frac{l_1 \sin\theta_1}{c_{g0}\sin(\theta_0+\theta_1)} = \Delta t_1 \tag{A.6-14}$$

Because the analytical expression of c_g is not available for anisotropic plates and only the numerical values of c_g with different wave propagating directions can be obtained, it is unlikely to obtain the analytical solution to Eq. (A.6-14). Thus a numerical method is employed to get the solution.

In order to solve Eq. (A.6-14) numerically, we can rearrange the equation and define the following cost function J_1 to avoid possible denominator to vanish and to make the computation more stable.

$$J_1 = \left| l_1 c_{g0} \sin\theta_0 - l_1 c_{g1} \sin\theta_1 - \Delta t_1 \, c_{g0} c_{g1} \sin(\theta_0+\theta_1) \right| \tag{A.6-15}$$

For a fixed value θ_0, θ_1 is iterated through to calculate the values of cost function J_1 until J_1 approaches zero and usually less than a specified terminal error. At this end, the

solution θ_1 from Eq. (A.6-15) is obtained for the fixed θ_0. Next a sufficiently small step size change θ_0 is made and the same iteration above to search another θ_1 is performed. After searching the suitable values of θ_0 and θ_1, the source possible location of $P(x, y)$ may be expressed as

$$\begin{cases} x = r_0 \cos(\theta_0 + \phi) = \dfrac{l_1 \sin\theta_1}{\sin(\theta_0 + \theta_1)} \cos(\theta_0 + \phi) \\ y = r_0 \sin(\theta_0 + \phi) = \dfrac{l_1 \sin\theta_1}{\sin(\theta_0 + \theta_1)} \sin(\theta_0 + \phi) \end{cases} \tag{A.6-16}$$

This produces locus of possible location points. Physically, all the points on the loci satisfy the arrival time difference Δt_1 at the sensor pair S_0, S_1.

In a similar manner, from sine law, we have the following relation in the triangle PS_0S_2

$$\frac{\sin(\alpha - \theta_0)}{r_2} = \frac{\sin\theta_2}{r_0} = \frac{\sin(\alpha - \theta_0 + \theta_2)}{l_2} \tag{A.6-17}$$

The distances r_0 and r_2 can then be written as

$$\begin{cases} r_0 = \dfrac{l_2 \sin\theta_2}{\sin(\alpha - \theta_0 + \theta_2)} \\ r_2 = \dfrac{l_2 \sin(\alpha - \theta_0)}{\sin(\alpha - \theta_0 + \theta_2)} \end{cases} \tag{A.6-18}$$

The time difference of arrival Δt_2 at the sensor pair S_0, S_2.

$$\Delta t_2 = t_2 - t_0 = \frac{r_2}{c_{g2}} - \frac{r_0}{c_{g0}} \tag{A.6-19}$$

Plugging Eq. (A.6-18) into Eq. (A.6-19) yields

$$\frac{l_2 \sin(\alpha - \theta_0)}{c_{g2} \sin(\alpha - \theta_0 + \theta_2)} - \frac{l_2 \sin\theta_2}{c_{g0} \sin(\alpha - \theta_0 + \theta_2)} = \delta_2 \tag{A.6-20}$$

Similarly, define the cost function J_2 as

$$J_2 = \left| l_2 c_{g0} \sin(\alpha - \theta_0) - l_2 c_{g2} \sin\theta_2 - \Delta t_2 c_{g0} c_{g2} \sin(\alpha - \theta_0 + \theta_2) \right| \qquad \text{(A.6-21)}$$

Use the iterative procedures to search the solution θ_0 and θ_2 which make the cost function J_2 approaches zero. After searching the suitable values of θ_0 and θ_2, the possible source location of $P(x, y)$ may be obtained as

$$\begin{cases} x = r_0 \cos(\theta_0 + \phi) = \dfrac{l_2 \sin\theta_2}{\sin(\alpha - \theta_0 + \theta_2)} \cos(\theta_0 + \phi) \\ y = r_0 \sin(\theta_0 + \phi) = \dfrac{l_2 \sin\theta_2}{\sin(\alpha - \theta_0 + \theta_2)} \sin(\theta_0 + \phi) \end{cases} \qquad \text{(A.6-22)}$$

The produces locus of possible location points, which satisfy the TDOA equals to Δt_2. The intersection of the two loci is the source location (Jeong and Jang, 2000).

A.6.4 Summary of the triangulation method (Jeong and Jang, 2000)

- The method is not an active detection technique but a passive sensing method, unsuitable for structural health monitoring;
- Three sensors can be arranged in arbitrary triangle;
- The method can locate the source either in an isotropic or in an anisotropic plate;
- The valid detection area includes within and beyond the enclosed triangular area;
- The closed-form solution of source location is not available because the closed-form expression of group velocity are inaccessible for anisotropic plates;
- The method can only obtain the numerical solution and a graphic technique is used to search the intersection of the two loci, the finial resulting location;
- Using the vector computation technique instead of do-loop in Matlab®, the computation speed is acceptable. For example, it takes less than 20 seconds to get the

source location in IM6/3501-6 composite plate by using a computer with 1.5GHz and 256MB RAM.

A.6.5 Numerical Simulation

This section demonstrates numerical simulation results of single source localization in both aluminum and composite plates based on Jeong and Jang's (2000) triangulation method by using two TDOA values. Three sensors are located at (0, 0)m, (10, 2)m, and (2, 10)m in a plate. Table 2.1 and Table 3.1 list the material properties of IM7/5250-4 composite plate and Al 6061 aluminum plate, respectively. After knowing the distance from source to sensor and calculating the group velocity, the time-of-flight of wave propagating from the source to the sensor can be theoretically computed; then the TDOA of sensor S_1 and S_2, and TODA of sensor S_1 and S_3 are obtained. Finally, these two TDOA values are fed into the algorithm of Section A.6.3 to numerically search the source location.

In the following figures, the green circles are the location of three sensors, and the red "x" indicates the location of target source. In addition, the blue locus denotes the possible source location which satisfies the TODA of sensor S_1 and S_2. Similarly, the cyan locus is the possible source location for the TODA of sensor S_1 and S_3. The evaluated source location is located at the cross point of the two loci in each figure.

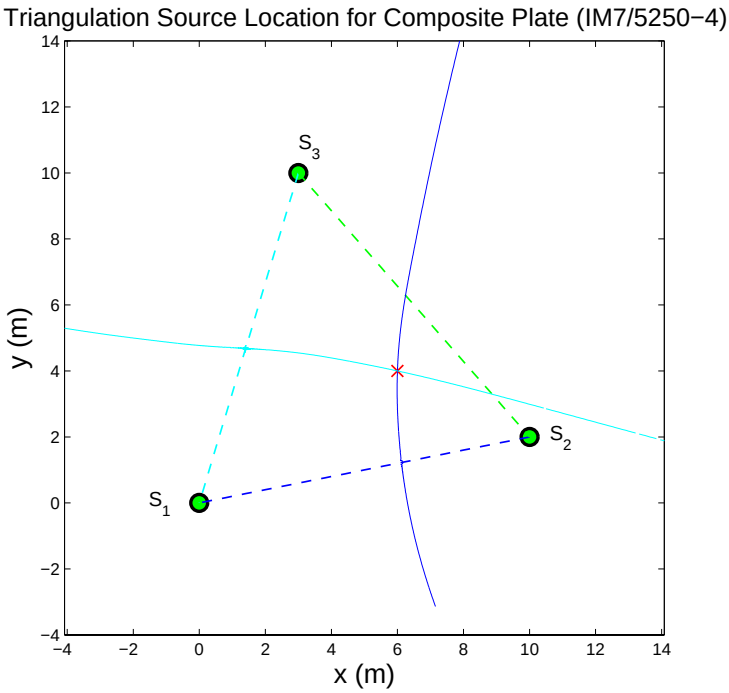

Figure A.6 Numerical simulation of source location in anisotropic plate with source at (6, 4) m denoted by “x”

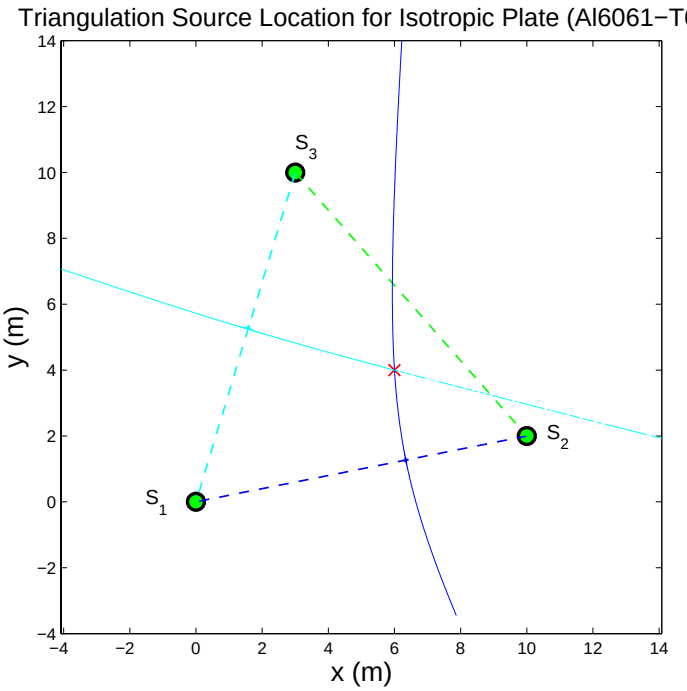

Figure A.7 Numerical simulation of source location in isotropic plate with source at (6, 4) m denoted by “x”

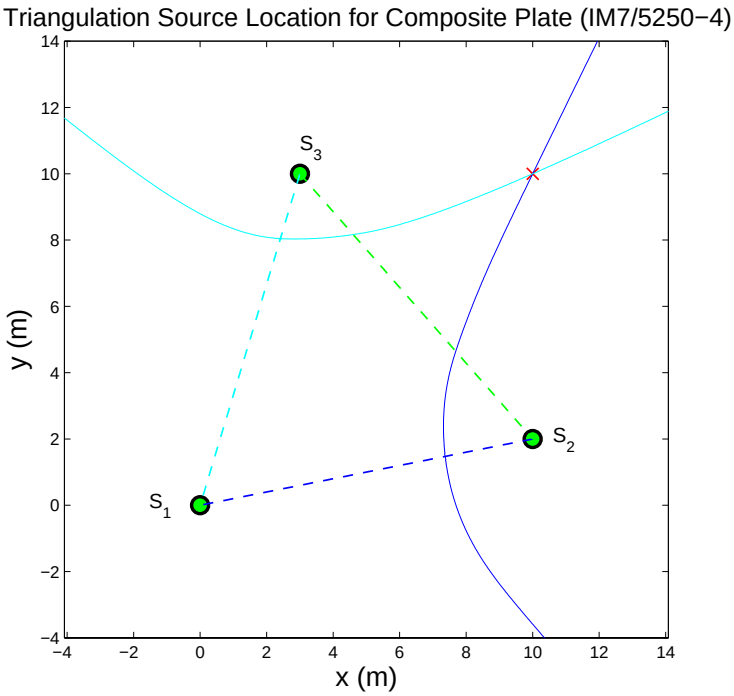

Figure A.8 Numerical simulation of source location in anisotropic plate with source at (10, 10) m denoted by “x”

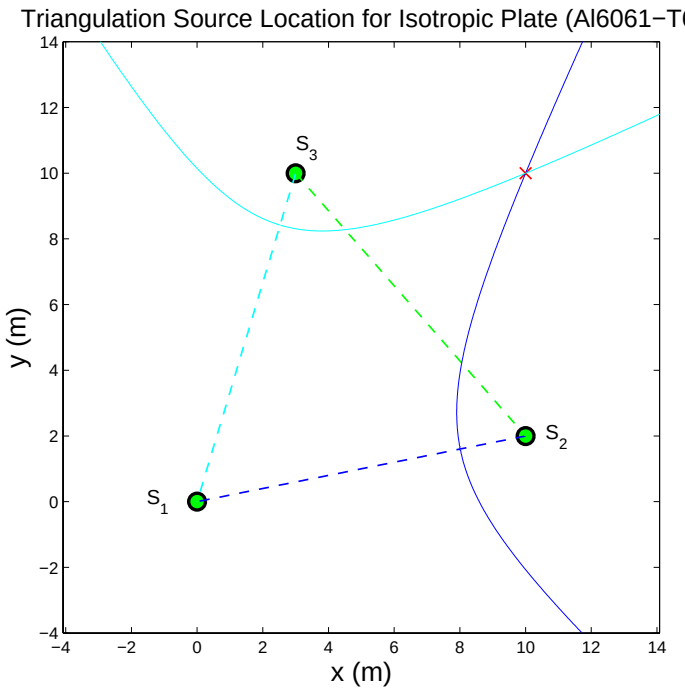

Figure A.9 Numerical simulation of source location in isotropic plate with source at (10, 10) m denoted by “x”